Actuation and Charge Transport Modeling of Ionic Liquid-Ionic Polymer Transducers

by

Jacob D. Davidson

Thesis submitted to the Faculty of the
Virginia Polytechnic Institute and State University
in partial fulfillment of the requirements for the degree of

Master of Science
in
Mechanical Engineering

Nakhiah C. Goulbourne, Chair
Donald J. Leo
Romesh C. Batra

January 28, 2010
Blacksburg, Virginia

Keywords: Ionic polymer transducer, ionic polymer-metal composite, Nafion, ionic liquid, ionic polymer, electroactive polymer

Actuation and Charge Transport Modeling of Ionic Liquid-Ionic Polymer Transducers

Jacob D. Davidson

(ABSTRACT)

Ionic polymer transducers (IPTs) are soft sensors and actuators which operate through a coupling of micro-scale chemical, electrical, and mechanical mechanisms. The use of ionic liquid as solvent for an IPT has been shown to dramatically increase transducer lifetime in free-air use, while also allowing for higher applied voltages without electrolysis. This work aims to further the understanding of the dominant mechanisms of IPT actuation and how these are affected when an ionic liquid is used as solvent. A micromechanical model of IPT actuation is developed following a previous approach given by Nemat-Nasser, and the dominant relationships in actuation are demonstrated through an analysis of electrostatic cluster interactions. The elastic modulus of Nafion as a function of ionic liquid uptake is measured using uniaxial tension tests and modeled in a micromechanical framework, showing an excellent fit to the data. Charge transport is modeled by considering both the cation and anion of the ionic liquid as mobile charge carriers, a phenomenon which is unique to ionic liquid IPTs as compared to their water-based counterparts. Numerical simulations are performed using the finite element method, and a modified theory of ion transport is discussed which can be extended to accurately describe electrochemical migration of ionic liquid ions at higher applied voltages. The results presented here demonstrate the dominant mechanisms of IPT actuation and identify those unique to ionic liquid IPTs, giving directions for future research and transducer development.

Acknowledgments

Firstly, I'd like to thank my advisor Dr. Goulbourne for giving me the opportunity to continue my education as a graduate student working on a cross-disciplinary research project in the area of smart materials. Her advice and encouragement has always pushed me to do my best. Coming from a non-engineering undergraduate, I definitely had a transition in graduate school and I'm grateful for all the help I got along the way. I'd also like to thank Dr. Leo and Dr. Batra for being on my committee and for all that I've learned from their classes and research that's helped me write this thesis.

Thanks goes out to all my colleagues at CIMSS for all the fun times as well as helpful discussions. It's been an interesting journey and I couldn't have done it without you guys. Special thanks goes out to Steve Anton, Kahlil Detrich, and Devon Murphy - without you all I'd still be stuck in a pile of dirt about 15 feet from my bike after that big jump on brush mountain. I feel lucky to have been around such a great group of people to learn from while starting the momentous quest of graduate school - one that I'll still be at for at least a few more years. I'd also like to thank Dr. Inman for creating a great work environment at CIMSS and always providing the lab with a good sense of humor.

Finally, I'd like to thank my parents for the ridiculous personalized license plate they purchased me for my truck. After reading this, I hope they at least have a vague idea of what "Nafion" is. Otherwise, please see Refs. [1-90]. I'm also grateful for the love and support provided by my family throughout the years.

Contents

List of Figures

viii

ix

List of Tables

Chapter 1

Introduction

Ionic polymer transducers (IPTs) are an emerging class of smart materials with applications as soft sensors and actuators. These transducers consist of an ion-exchange membrane placed in a certain cation form (typically Li^+ or Na^+), solvated with a polar solvent, and electroded on both sides. When a DC voltage (1-5 V) is applied to the faces of an IPT in a cantilever configuration, the transducer will bend towards the anode as shown in Figure 1.1. Conversely, a voltage will be generated by an IPT when a mechanical deformation is imposed. These transduction properties are the result of ion and solvent transport through the thickness of the membrane.

IPT performance is affected by cation form, the nature of the solvent, the ionomer membrane, and the electrode composition. Water provides a fast actuation response, but water-based transducers are not stable for free-air use due to water evaporation and drying out of the IPT.
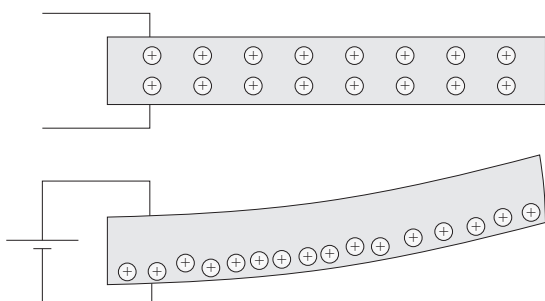
Figure 1.1: An IPT will bend towards the anode when a voltage is applied due to cation and solvent movement.

Ionic liquids have been shown to dramatically increase a transducer's lifetime in free-air use [1]. The negligible vapor pressure of an ionic liquid inhibits evaporation. Studies have shown that a water-based transducer will stop working after around 3 000 cycles, while similar ionic liquid-based transducers displayed only a 30% decrease in strain response after 250 000 cycles, when actuating with a 2 Hz sine wave with a peak of 1.5 V [1]. Another difficulty with using water is the small electrochemical stability window, since electrolysis will begin to occur at approximately 1.2 V. Since the dominant mechanism of actuation is charge transport by migration, electrochemical oxidation/reduction reactions at the electrodes are not desired. Ionic liquids have larger electrochemical stability windows: 1-ethyl-3-methylimidazolium trifluoromethanesulfonate (EMI-Tf) ionic liquid, which is commonly used in IPTs, is stable up to 4.1 V [2]. The application of higher voltages results in increased ion and solvent transport and a greater actuation response.

The term "ionic liquid" is used to describe salts that are in liquid form near room temperature. In a typical electrolyte solution, the solvent overcomes the forces holding together the salt molecules so that the ionic bond is broken and the ions become dissociated and free to move separately in the solution. In an ionic liquid, heat energy at or near room temperature is enough to overcome the cohesive forces between the salt molecules, so the substance exists as a liquid. Ionic liquids typically contain an organic cation and an inorganic/polyatomic anion and have several unique and attractive properties: negligible vapor pressure, a wide electrochemical window, a large temperature range between the melting and boiling points, and high ionic conductivity. Although the conductivity may be high compared to that of water or dilute electrolyte solutions, the conductivity of an ionic liquid is still about four orders of magnitude lower than that of a liquid metal [3]. This means that conduction still occurs through ion transport, just like in an electrolyte solution. However, the large sizes of the ionic liquid ions will change the structure of the electric double layer, as is discussed in Chapter 3.

In order to create targeted, high performance electroactive devices and improve the performance of current transducers, a model of the fundamental mechanisms of IPT actuation is needed so that material properties and transducer characteristics can be optimized. Current IPT modeling attempts can be placed into several different categories, including equivalent circuit models [4, 5, 6], semi-empirical models [7, 8], and physics-based models [9, 10, 11, 12, 13]. In this work, a physics-based approach is taken, using the modeling framework outlined by Nemat-Nasser [12, 13] as a starting point. In an IPT system, the

introduction of an ionic liquid poses several questions: Are the fundamental transduction mechanisms the same as those of water-based transducers? How is charge transport affected? Experimental investigations using spectroscopy as well as examining the actuation response have pointed out a few differences. For example, infrared spectroscopy results show a lower frequency of the symmetric sulfonate-oxygen stretching peak for ionic liquid-swollen versus water-swollen Nafion membranes when the membrane is swollen above the critical uptake [14]. Additionally, it is known that ionic liquid-based IPTs typically do not display back relaxation [1, 15], while Nafion-based IPTs with water as solvent exhibit an extensive back relaxation effect [9, 12, 15].

The overall goal of this research is to develop a model for the transduction mechanisms in ionic liquid IPTs. With an understanding of the underlying mechanisms in these transducers and the differences compared to when other polar solvents are used, optimal material properties can be predicted and applied to the development of future devices. In this work, the focus is on developing a model which can identify and account for the effects that are unique to ionic liquid IPTs, and which also can be used to describe new actuator systems. First, the micromechanics modeling framework is outlined in Chapter 2, and the governing equations for charge transport are given in Chapter 3. Next, actuation mechanisms are analyzed by considering effective cluster pressures during actuation (Chapter 4) and the resulting deformation of the IPT (Chapter 5). The mechanical properties of Nafion membranes swollen with ionic liquid are measured experimentally and modeled in Chapters 6 and 7. The actuation model is applied to an ionic liquid IPT in Chapter 8, and results for numerical simulations of charge transfer are presented in Chapter 9. Finally, the results are discussed and directions for future work are suggested in Chapters 10 and 11.

Chapter 2

Modeling Framework

2.1 Actuation Mechanisms

When a voltage is applied to the faces of an IPT, the mobile ions in the polymer will move to screen the applied field. For water-based IPTs, the neutralizing cation species (typically Li^+ or Na^+) is the only mobile ion in the polymer. When ionic liquids are used there will be multiple mobile ionic species - this is modeled in Chapter 3. The movement of ions causes the formation of thin layers near each electrode that have an excess or a depletion of charge. These layers, referred to as boundary layers, are where all the 'action' occurs during actuation. Electrostatic interactions between the ions cause pressures to develop in the boundary layers, and the resulting pressure gradient causes the movement of solvent molecules. The boundary layers will either expand or contract as the solvent molecules move to neutralize the pressure gradient, causing an elastic deformation of the polymer backbone material. Equilibrium will consist of a balance between electrostatic interactions, migration and diffusion potentials, and the resulting elastic stress from boundary layer expansion or contraction. It is found that the cathode boundary layer undergoes a larger expansion than the anode boundary layer, and thus an IPT in a cantilever configuration will bend towards the anode as shown in Figure 1.1.
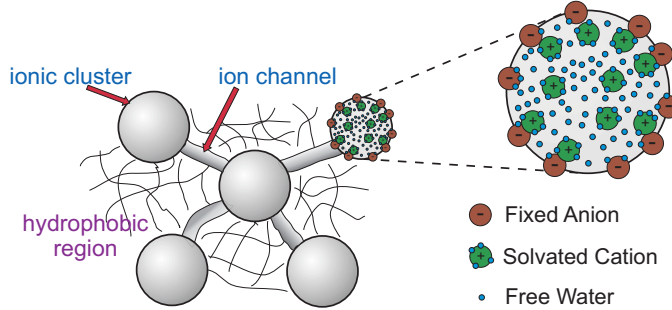
Figure 2.1: The assumed microstructure of Nafion, showing clusters interconnected by channels through which ions move.

2.2 Microstructure and Micromechanics

The unique chemical structure and morphology of the base ionomer membrane, e.g. Nafion, enables all the processes leading to actuation to occur, so a brief overview of ionomer characteristics and physical properties will be presented to facilitate model development. For a general introduction to ionomer chemistry and physical properties, see [16]. Here, the focus is on Nafion, which has been extensively studied for its unique properties and wide range of applications [17, 18]. Most work with IPTs has used Nafion, although recent work has demonstrated the successful use of other ionomers [19, 20, 21].

In a Nafion membrane, it is thermodynamically favorable to form ionic clusters, consisting of the functional sulfonate end-groups, in order to minimize the potential energy of the system [22]. Different theories have been proposed to describe cluster composition in Nafion and other ionomers, including the core-shell model [23], modified hard-sphere model [24, 25], multiplet-cluster model [26], cluster-network model [27, 28], and, most recently, the parallel cylindrical channel model [29, 30, 31]. In the following, the cluster-network model is used to describe the microstructure of Nafion. It is assumed that the clusters grow in size when solvent is absorbed by the polymer and at a certain threshold of solvent uptake become interconnected by channels through which ions move. At and above this level of solvent uptake the ionomer becomes a good conductor of ions [27, 28, 32]. Previous research has shown that the ionic conductivity of the membrane and the performance of the IPT actuator markedly increase above this critical uptake [14, 15, 33, 34].

Figure 2.1 shows the assumed microstructure of the system, showing water as the solvent. The Teflon backbone of Nafion is hydrophobic, and therefore the solvent will exist almost
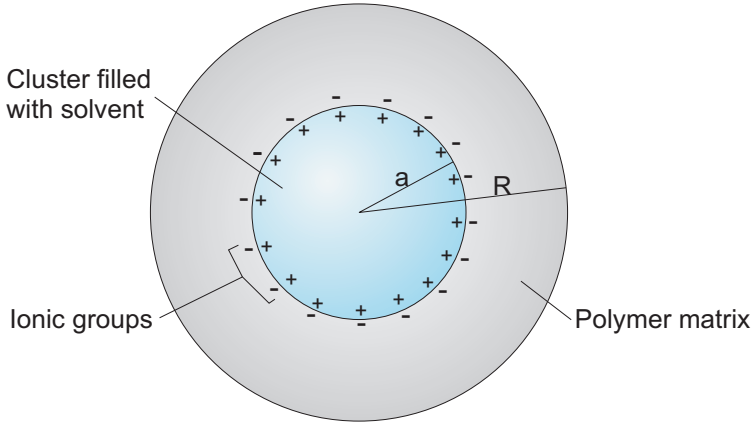
Figure 2.2: The representative volume element for the system, consisting of a spherical cluster of radius a embedded in a polymer matrix of radius R.

exclusively in the ionic clusters and channels. To further simplify the system it is assumed that the amount of ions and solvent in the connecting channels is negligible compared to that existing in the clusters. Therefore a representative volume element (RVE) can be defined to represent a typical cluster as shown in Figure 2.2. The polymer matrix surrounding the cluster is approximated as a homogeneous continuum, and it is assumed that all clusters have the same initial size (before a voltage is applied). The length scale of the RVE is on the order of nanometers, since a representative cluster in an IPT actuator has radius ~ 1.6 nm [12]. Additionally, a dilute distribution of clusters is assumed, i.e. the expansion/contraction of one cluster will not affect the behavior of a neighboring cluster.

Of course, these idealizations are not a direct picture of the system. A Gaussian distribution of cluster sizes is expected and the interactions between polymer chains outside of and between clusters will consist of coupled interactions including van der Waals forces, electrostatic repulsion/attraction, and conformational reorganization. The use of these assumptions allows for analytical progress to be made in forming a model of the system, and a comparison can be made with experimental results to validate the model.

2.3   Electrode Structure

IPTs were first constructed with platinum and gold electrodes [35, 36]. To create these electrodes, the Nafion polymer is soaked in a platinum salt solution and then a reducing agent

is used to deposit the platinum on the surface of the membrane [37]. The platinum is seen to penetrate into the polymer and form an electrode structure several microns thick (Figure 2.3(a)). Gold is electroplated onto the surface of the platinized membrane to improve surface conductivity, which greatly improves the performance of the device [38]. These fabrication methods place practical limits on the use of potential solvents, however, because the Pt reduction and Au electroplating processes are typically done in aqueous solutions.

Subsequent research has shown that the actuation performance of an IPT is directly related to its capacitance [39], and a new fabrication technique was developed to create optimized transducers [40]. The Direct Assembly Process (DAP) in Ref. [40] also allows for ionic liquids to be easily incorporated as solvent since electroding processes are not performed in aqueous solutions. The basic process to make an ionic liquid IPT using DAP is to start with a Nafion membrane, exchange the cation, swell with an ionic liquid, spray on electrode materials, and then press on gold foil to improve the surface conductivity. Figure 2.3(b) shows a cross section of a water-based DAP IPT with ruthenium oxide (RuO_2) and Pt composite electrodes, and Figure 2.3(c) shows a cross section of an ionic liquid DAP transducer made with RuO_2. As can be seen, the electrode is far from a flat metal surface - the interpenetrating distribution of metal particles increases the effective surface area of the electrode region, which greatly increases the overall capacitance of the transducer.
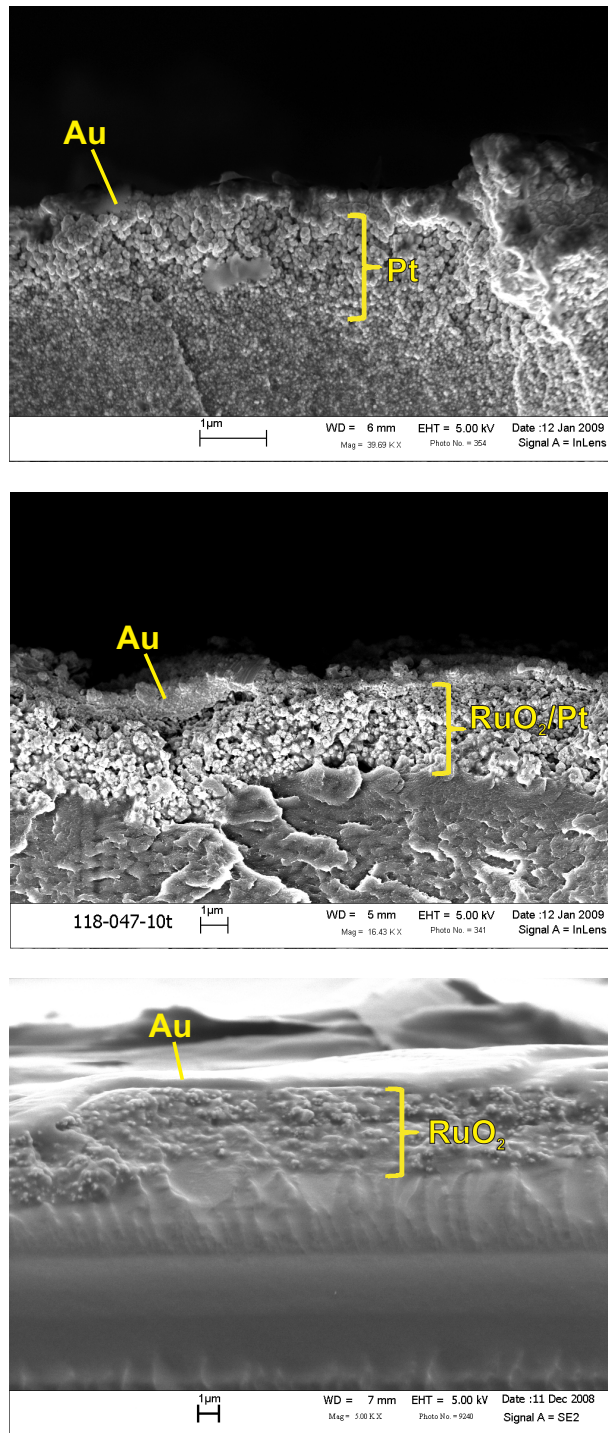
Figure 2.3: SEM images of the cross section of IPTs made with different electrode materials. (a) A water-based IPT with Pt/Au electrodes. (b) A water-based IPT with RuO_2/Pt/Au electrodes. (c) An ionic liquid IPT with RuO_2/gold foil electrodes and EMI-Tf ionic liquid as solvent.

Chapter 3

Charge Transport Modeling

When a voltage is applied across the faces of an IPT, ion movement causes the formation of boundary layers near each electrode. From previous experimental and theoretical studies [10, 12, 39, 41, 42, 43] it is known that the actuation of an IPT is a direct function of the charge transported when a voltage is applied. Akle et al. [39] demonstrated that IPT actuation performance is directly related to capacitance, and thus a direct function of the charge transferred. In Ref. [43], Shahinpoor and Kim model the deformation of an IPT as a result of solvent flux from changes in osmotic pressure, which varies linearly with the volumetric charge density in the polymer. Porfiri [42] uses a similar relationship for electromechanical coupling, saying that the stress in the polymer (and thus the bending moment generated during actuation) is linearly related to the volumetric charge density. Leo et al. [41] model the stress developed in the polymer during actuation as a sum of linear and quadratic terms of the spatially varying volumetric charge density. This same relation for electromechanical coupling is also used by Wallmersperger et al. in Ref. [10]. Nemat-Nasser [12] states that transported charge causes electrostatic and osmotic pressures to develop in the polymer, which in turn cause solvent flux, boundary layer expansion, and actuation. This approach is taken in the model presented in the following chapters.

The charge transport characteristics of an IPT are obviously an important point to study in order to model and understand the actuation response. For ionic liquid IPTs, the fundamental question is: How does the introduction of an ionic liquid affect the charge transport properties? In a water-based IPT, the counter-cation (typically Li^+ or Na^+) is the only mobile ionic species and functions as the sole charge carrier in the device. When an ionic liquid

is present, the cation and anion of the ionic liquid will also function as mobile charge carriers, which creates a unique distinction in charge transport characteristics for ionic liquid IPTs versus their water-based counterparts. In the following, a model is presented which describes the movement of multiple mobile ionic species in ionic liquid IPTs. First, an overview of Nernst-Planck/Poisson (NPP) theory is given and the governing equations considering a single mobile ionic species are established. Next, a modified theory is presented which accounts for the finite size of the ions of the ionic liquid. The governing equations for multiple mobile ionic species in an ionic liquid IPT are established, and the numerical framework for solving the simpler case of classic NPP theory is given.

3.1 Nernst-Planck/Poisson Theory Applied to an IPT

The electrochemical potential of a species i in a given phase is

$$\mu_i = \mu_i^0 + z_i F \phi + RT \ln a_i \tag{3.1}$$

where a_i is the activity and z_i is the charge of the species, ϕ is the electric potential, R is the universal gas constant, F is Faraday's constant, T is temperature in kelvin, and μ_i^0 is the standard chemical potential. The activity is the product of the activity coefficient and the concentration, i.e. $a_i = \gamma_i c_i / c_{std}$, where the dimensionless coefficient γ_i represents the deviation from ideal solution behavior. Using molar concentration, $c_{std} = 1$ M [44]. For ions in an electrolyte solution, $\gamma_i = 1$ corresponds to an infinitely dilute solution. Assuming that γ_i is constant over the concentration ranges being studied, the electrochemical potential is now expressed as

$$\mu_i = \mu_i^{0'} + z_i F \phi + RT \ln c_i \tag{3.2}$$

where

$$\mu_i^{0'} = \mu_i^0 + RT \ln \gamma_i \tag{3.3}$$

is taken to be constant. By using Eq. 3.2 for the electrochemical potential, explicitly dealing with the activity coefficient γ_i is avoided. Note that Eqs. 3.1, 3.2, and 3.3 appear to contain dimensional errors, since c_i has units of concentration and γ_i is unitless. This is because the standard state is defined using a hypothetical 1 M solution [44] and thus the term $-RT \ln c_{std} = 0$ is omitted from Eq. 3.2 with no loss of information.
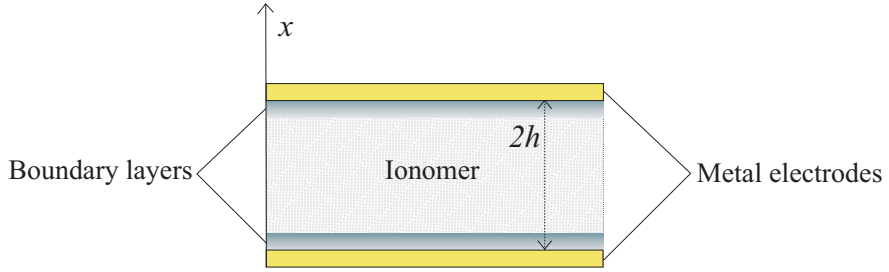
Figure 3.1: A diagram of the system for modeling ion transport, showing the through-thickness x direction.

The concentration of the fixed anionic groups is calculated to be

$$c_0 = \frac{\rho_b}{EW(1+w)} \tag{3.4}$$

where $\rho_b \approx 2.0$ g/cm^3 is the dry density of Nafion, EW is the equivalent weight of the ionomer in g/mol, and the solvent uptake w is the ratio of the volume of the solvent to the volume of the dry polymer:

$$w = \frac{V_{solvent}}{V_{polymer}} \tag{3.5}$$

The electrochemical potential of the mobile cations, given by Eq. 3.2, is inserted into Fick's law of diffusion

$$J_i = -\frac{D_i c_i}{RT} \frac{\partial \mu_i}{\partial x} \tag{3.6}$$

where D_i is the diffusion coefficient of species i, to obtain the 1-dimensional Nernst-Planck equation for the ith species:

$$J_i = -D_i \left(\frac{\partial c_i}{\partial x} + \frac{z_i c_i F}{RT} \frac{\partial \phi}{\partial x} \right) \tag{3.7}$$

where J_i is ion flux. Symmetry along the length and width of the IPT has been presumed to reduce the problem to only the through-thickness direction x as shown in Figure 3.1. Recent results using nuclear magnetic resonance spectroscopy (NMR) have shown that Nafion displays a certain degree of diffusion anisotropy, which results from a preferential channel alignment along one of the normal axes created by the manufacturing process [45]. Because of the geometry of an IPT, only the through-thickness direction needs to be considered to model actuation, and therefore diffusion anisotropy does not need to be taken into account. In deriving Eq. 3.7 it has also been assumed that $\gamma_i = const$. For the large concentration

gradients that develop when a voltage is applied to an IPT, this assumption is not expected to hold. An alternative theory which implements an effective correction to γ_i for the large ionic liquid ions is discussed in Section 3.3.

The transient behavior of the mobile cations is determined by combining Eq. 3.7 with the expression for the conservation of mass:

$$\frac{\partial c_i}{\partial t} + \frac{\partial J_i}{\partial x} = 0 \tag{3.8}$$

The resulting equation using Eqs. 3.7 and 3.8 is solved along with the Poisson equation [46],

$$\frac{\partial^2 \phi}{\partial x^2} = -\frac{F}{\bar{\epsilon}} \sum_i z_i c_i \tag{3.9}$$

where $\bar{\epsilon}$ is the effective average permittivity of the IPT, to obtain the transient charge transfer response. To proceed, it is useful to first non-dimensionalize (* variables) using the following definitions:

$$\phi^* = \phi \frac{F}{RT} \qquad c^* = \frac{c}{c_0} \qquad x^* = \frac{x}{\lambda} \qquad t^* = \frac{t}{\tau} = \frac{tD_+}{\lambda^2} \tag{3.10}$$

The Debye length, λ, and the Debye time, τ, are defined as

$$\lambda = \left(\frac{\bar{\epsilon}RT}{c_0 F^2}\right)^{1/2} \qquad \tau = \frac{\lambda^2}{D_+} \tag{3.11}$$

where the diffusion coefficient of the counter-cation, D_+ is used to define τ.

The average permittivity of the IPT, $\bar{\epsilon}$, is defined using an approximate bulk capacitance measurement to incorporate some effects of the interpenetrating electrodes. This effectively changes the length scale of the problem by increasing the Debye length and therefore the size of the boundary layers relative to the total thickness of the polymer, $2h$. With this approximation, predictions for the amount of charge transferred when a voltage is applied become on the order of experimental results. The electrode structure can alternatively be represented by specifying the microscopic surface area of the electrode and using a value for the permittivity corresponding to an averaging of ionic liquid, water, and Nafion (which would give $\bar{\epsilon} < 10\epsilon_0$) [42]. This definition may give more direct information about the electrodes, but leads to numerical instabilities from the small relative size of the boundary layers,

λ/h. The definition of $\bar{\epsilon}$ using an approximate capacitance measurement has been shown to yield a good comparison with experimental results [10, 12], and this approach is taken here. Although this approach does not give any specific information on the characteristics of the interpenetrating electrodes, it simplifies the numerical analysis such that dominant charge transfer characteristics can more easily be identified.

3.2   Governing Equations for a Single Mobile Ionic Species

When an ionic liquid is not used (e.g. water-based IPTs), there is only a single mobile ionic species: The counter-cation, which is typically Li^+ or Na^+. In this case, the non-dimensional form of the governing equations become (dropping the * for ease of notation):

$$J_+ = -D_+ \left(\frac{\partial c_+}{\partial x} + c_+ \frac{\partial \phi}{\partial x} \right) \tag{3.12}$$

$$\frac{\partial c_+}{\partial t} + \frac{\partial J_+}{\partial x} = 0 \tag{3.13}$$

$$\frac{\partial^2 \phi}{\partial x^2} = -c_+ + 1 \tag{3.14}$$

The initial and boundary conditions are

$$c_+(x,0) = 1$$

$$J_+(\pm h^*, t) = 0$$

$$\phi(\pm h^*, t) = \mp \frac{V_0^*}{2} \tag{3.15}$$

where $h^* = h/\lambda$ is the non-dimensionalized thickness parameter ($2h$ is the thickness of the polymer layer - see Figure 3.1) and V_0^* is the non-dimensionalized applied voltage. The concentration of the fixed anionic groups, c_0, is taken as constant, although it will change slightly with the varying solvent uptake in the boundary layers during actuation according to Eq. 3.4. Considering a single mobile ionic species, there are only two coupled equations with two unknowns, $c_+(x,t)$ and $\phi(x,t)$, to solve for. Eqs. 3.12-3.14 can also be used in an approximate treatment of charge transport in an ionic liquid IPT since the counter-cation will still be the dominant charge carrier. This simplified approach is used to model actuation in Chapters 4 and 5.

3.3 Modified NPP Theory for Ionic Liquid IPTs

Previous research regarding ionic liquid IPT actuation has not considered the dynamics of charge transport concerning the ions of the ionic liquid. In an ionic liquid IPT, there are three mobile ions: the neutralizing cation and both the anion and cation of the ionic liquid. Recent results have shown that not all of the ions of the ionic liquid will exist as "free" ions, able to selectively move under the applied electric field [47]. Some ionic liquid ions stay associated as dipole and quadrupole pairs and will not move as ions when a voltage is applied. This was taken into account by performing parameter variations to analyze the effect of free ionic liquid ion content on the response of the system in Chapter 9.

Before applying Eqs. 3.7, 3.8 and 3.9 to describe an ionic liquid IPT, it is important to look at the assumptions involved. The Poisson equation is an expression of the electrostatic mean field across the membrane. The local field on the atomic scale is quite complex; molecular dynamics simulations are needed to quantify local interactions when multiple particles are involved. For an IPT, we are looking at length scales larger than the atomic scale, so Eq. 3.9 is expected to hold. Eq. 3.7 needs to be carefully examined, however. Recall that the electrochemical potential was expressed as

$$\mu_i = \mu_i^{0'} + z_i F \phi + RT \ln c_i \qquad (3.16)$$

where

$$\mu_i^{0'} = \mu_i^0 + RT \ln \gamma_i \qquad (3.17)$$

was taken to be constant. This is inserted into Fick's law of diffusion to obtain Eq. 3.7. Setting $\gamma_i = const$ is equivalent to saying that the free energy of the system will follow the same constitutive relationship regardless of concentration. This is a good assumption for many applications where the size of the ions is small compared to the characteristic length scale for the problem. However, at higher applied voltages, or when the size of the ion increases, this assumption is not valid. When a significant potential difference is applied, the second term in Eq. 3.7 will initially be large, and a large number of ions will move under migration. The diffusion term in Eq. 3.7 will stay the same. Since the Debye length is independent of applied voltage, the Nernst-Planck equation says that the extra ions moving into the boundary layer will continue to pack more closely together. Eventually, local short-range interactions between the ions will become important. These consist of

local electrostatic interactions, van der Waals forces, and steric effects. The latter two are often included in molecular simulations using the Lennard-Jones potential. The physical interpretation of steric effects at an atomic scale can be thought of as a strong repulsion due to the overlap of electron orbitals.

A strong steric repulsion between molecules is equivalent to saying that the free energy of the system increases dramatically when the molecules become very closely packed. This will tend to limit the maximum concentration level that is reached according to the sizes of the molecules. This sort of interaction is reflected mathematically by a change in the activity of the ionic species - the activity will increase rapidly when concentration reaches a certain point and steric effects become important. At low applied potentials or when the sizes of the ions are small this effect is negligible and is typically not included in a model of the electric double layer. However, when a large potential is applied, or the ions are large such as in an ionic liquid, this is an important effect to include. In an ionic liquid, the ions form a lattice-like structure which also has "holes" that fluctuate due to Brownian motion [3]. Because of the holes, the maximum concentration, say, the cations can reach will be greater than twice its initial concentration (assuming both ions have equal size).

Recent work has been done to model these effects in ionic liquids and concentrated electrolyte solutions [48, 49, 50]. Kornyshev [48] proposes a change in the electrochemical potential of the ionic liquid ions of the form

$$
\begin{aligned}
\mu_+ &= \mu_+^0 + F\phi + 2A_+ c_+ + Bc_- + RT \ln \frac{c_+}{c_{max} - c_+ - c_-} \\
\mu_- &= \mu_-^0 - F\phi + 2A_- c_- + Bc_+ + RT \ln \frac{c_-}{c_{max} - c_+ - c_-}
\end{aligned}
\tag{3.18}
$$

where $A_\pm$, B, and c_{max} are empirical factors representing interactions between like-charged and oppositely-charged ions, and the maximum possible concentration, respectively. Comparing Eq. 3.18 with the typical expression for chemical potential, it is seen that the activity coefficients of the cations and anions can be effectively defined to be $\gamma_+ = \gamma_- = c_{std}(c_{max} - c_+ - c_-)^{-1}$. As $(c_+ + c_-) \to c_{max}$, $\gamma_\pm \to \infty$, and therefore the so-called "lattice saturation" effect is represented. Inserting Eq. 3.18 into Fick's law of diffusion (Eq. 3.6), the

flux of the ionic liquid ions is

$$J_+ = -D_+ \left(\frac{c_+ F}{RT} \frac{\partial \phi}{\partial x} + \frac{\partial c_+}{\partial x} + 2A_+ c_+ \frac{\partial c_+}{\partial x} + B c_+ \frac{\partial c_-}{\partial x} + \frac{c_+ \left(\frac{\partial c_+}{\partial x} + \frac{\partial c_-}{\partial x} \right)}{c_{max} - c_+ - c_-} \right)$$

$$J_- = -D_- \left(\frac{-c_- F}{RT} \frac{\partial \phi}{\partial x} + \frac{\partial c_-}{\partial x} + 2A_- c_- \frac{\partial c_-}{\partial x} + B c_- \frac{\partial c_+}{\partial x} + \frac{c_- \left(\frac{\partial c_+}{\partial x} + \frac{\partial c_-}{\partial x} \right)}{c_{max} - c_+ - c_-} \right) \qquad (3.19)$$

The first two terms are the same as those in Eq. 3.7, and the next three terms represent specific ionic interactions and steric effects.

3.4   Governing Equations and FEM Framework for Ionic Liquid IPTs

Eq. 3.19 is highly nonlinear due to the last term, where the concentration appears in the denominator, and the inclusion of this term significantly complicates the numerical analysis. In this work, the classic NPP theory will be used at low applied potentials to gain insight into charge transport mechanisms when there are multiple mobile ionic species. In modeling an IPT system, allowing an ionic liquid ion to reach a concentration higher than its neat solution maximum is correct in the model to a certain extent, since the boundary layers will actually expand and make room for more ions to fit in. This justifies the use of the classic NPP theory at low applied potentials; however, the range of applicability of Eq. 3.7 is clearly limited for ionic liquids and a modification such as that described by Eq. 3.19 needs to be included to model ion transport in ionic liquid IPTs at actuator operating voltages. Nonetheless, a test case considering a low applied voltage using NPP theory gives insight into the movement of multiple mobile ionic species and the resulting charge transport characteristics which are unique to ionic liquid IPTs. This approach is taken here.

Using classic NPP theory, i.e. not considering steric effects and specific ionic interactions,

the governing equations for 3 mobile ionic species are expressed in non-dimensional form as

$$J_i = -D_i \left(\frac{\partial c_i}{\partial x} + z_i c_i \frac{\partial \phi}{\partial x} \right) \tag{3.20}$$

$$\frac{\partial c_i}{\partial t} + \frac{\partial J_i}{\partial x} = 0 \tag{3.21}$$

$$\frac{\partial^2 \phi}{\partial x^2} = - \left(z_1 c_1 + z_2 c_2 + z_3 c_3 - 1 \right) \tag{3.22}$$

where the diffusion coefficients D_i are normalized with respect to the diffusion coefficient of the counter-cation. Modeling the electrodes as blocking electrodes, the initial and boundary conditions are

$$c_i(x, 0) = c_i^0 \tag{3.23}$$

$$J_i(\pm h^*, t) = 0 \tag{3.24}$$

$$\phi(\pm h^*, t) = \mp \frac{V_0^*}{2} \tag{3.25}$$

The finite element method is used to solve Eqs. 3.20-3.22, and is implemented following Lim [51]. However, in this analysis there are three mobile ionic species and one fixed negatively charged species, in comparison to two mobile species in Ref. [51]. First, the weak form of Eqs. 3.20-3.22 is derived by multiplying each equation by a test function, ψ, and integrating over the domain. Next, the Galerkin method is used to define the approximation to the solution for each variable and for the test function:

$$c_j \approx N_A c_A^j \qquad \phi \approx N_A \phi_A \qquad \psi \approx N_A e_A \tag{3.26}$$

where N_A are the Hermite shape functions, e_A are arbitrary constants, and summation convention is used over indices in CAPS. It should be noted that since a weak form of Eqs. 3.20-3.22 only involves 1st order derivatives of c_j and ϕ, linear (Lagrange) basis functions are sufficient in obtaining a solution using the finite element method. Both Hermite and Lagrange basis functions were used in generating solutions, and it was seen that the solutions using Hermite basis functions were significantly smoother than those using Lagrange basis functions. Since the additional computational time needed to use the higher order basis functions is not a significant problem for this 1-dimensional solution, Hermite basis functions were used in the solutions shown later in Section 9.2. In this formulation, both the variable and its first derivative appear as unknowns. Now, using Eq. 3.26, the system of equations is

written as

$$\Phi_A = \left[N_A \frac{dN_B}{dx} \phi_B \right]_{-h^*}^{h^*} - \int_{-h^*}^{h^*} \frac{dN_A}{dx} \frac{dN_B}{dx} \phi_B dx + \int_{-h^*}^{h^*} N_A \left[N_B \sum_{j=1}^{3} z_j c_B^j - 1 \right] dx = 0$$

$$\Theta_A^i = \int_{-h^*}^{h^*} N_A N_B \frac{dc_B^i}{dt} dx + [N_A J_i]_{-h^*}^{h^*} + \int_{-h^*}^{h^*} D_i \frac{dN_A}{dx} \left(\frac{dN_B}{dx} c_B^i + z_i N_B c_B^i \frac{dN_K}{dx} \phi_K \right) dx = 0$$

$$(3.27)$$

where $h^* = h/\lambda$ is the non-dimensionalized thickness parameter ($2h$ is the thickness of the polymer layer - see Figure 3.1), and again summation convention is only used over indices in CAPS. Since Hermite shape functions are used, there are 4 equations for each element for Φ_A and Θ_A^i, and $i = 1...3$ for the 3 mobile ionic species. There is thus a total of 8 degrees of freedom at each node, which translates to a total of 16 degrees of freedom per element. The element equations and nodal variables are assembled as

$$\mathbf{G}^e = \left\{ \Phi_1, \Phi_2, \Theta_1^1, \Theta_2^1, \Theta_1^2, \Theta_2^2, \Theta_1^3, \Theta_2^3, \Phi_3, \Phi_4, \Theta_3^1, \Theta_4^1, \Theta_3^2, \Theta_4^2, \Theta_3^3, \Theta_4^3 \right\} \qquad (3.28)$$

$$\mathbf{q}^e = \left\{ \phi_1, \phi_2, c_1^1, c_2^1, c_1^2, c_2^2, c_1^3, c_2^3, \phi_3, \phi_4, c_3^1, c_4^1, c_3^2, c_4^2, c_3^3, c_4^3 \right\} \qquad (3.29)$$

The global system of equations is assembled to be $\mathbf{G}$, with global variables $\mathbf{q}$, and the system of equations is now written in matrix form:

$$\mathbf{G}(\mathbf{q}) = \mathbf{M}\dot{\mathbf{q}} + \mathbf{r}(\mathbf{q}) - \mathbf{f} = 0 \qquad (3.30)$$

The contents of $\mathbf{M}$, $\mathbf{r}(\mathbf{q})$, and $\mathbf{f}$ are given in Appendix A. Since the governing equations are nonlinear, Newton-Raphson iteration is performed at each time step to obtain the values for the nodal variables $\mathbf{q}$. Using the backward difference method, the algorithm involves expanding Eq. 3.30 in a Taylor series about the current approximation for the solution, $\tilde{\mathbf{q}}$, keeping first order terms, and re-arranging to get

$$\left[\mathbf{M} + \Delta t \left(\frac{\partial \mathbf{r}}{\partial \mathbf{q}} \right)_{\mathbf{q} = \tilde{\mathbf{q}}} \right] \mathbf{\Gamma}(\tilde{\mathbf{q}}) = -\mathbf{G}(\tilde{\mathbf{q}}) \qquad (3.31)$$

where $\mathbf{\Gamma}$ is the correction to the current approximation for the solution. This equation is solved and the solution for time $t + 1$ is updated to be $\mathbf{q}_{t+1} = \tilde{\mathbf{q}} + \mathbf{\Gamma}(\tilde{\mathbf{q}})$. If the residual, $\sum_j |\mathbf{G}_j(\mathbf{q}_{t+1})|$, is within acceptable limits, the solution for $\mathbf{q}_{t+1}$ is kept and the program moves to the next time step. If the residual is not acceptable, $\tilde{\mathbf{q}}$ is set equal to $\mathbf{q}_{t+1}$ and

Figure 3.2: An example of a refined mesh, defined with 100 elements and a refinement factor of $g = 1.1$.

the process is repeated until the residual is acceptably small. The convergence criteria used in the numerical solution was $\sum_{j=1}^{m} |\mathbf{G}_j| < 10^{-6}$, where the total number of equations is $m = 8(ne + 1)$. A method to calculate the tangent matrix $\frac{\partial \mathbf{r}}{\partial \mathbf{q}}$ is outlined in Appendix A.

Since the boundary layers are small compared to the thickness of the membrane, a refined mesh is used which places smaller elements near the electrodes. This is done by using a refinement factor, g, and generating elements with increasing/decreasing sizes proportioned by g^n, where n refers to the nth element with respect to either boundary. A refined mesh is needed at both boundary layers since the concentration in both layers will change appreciably when a voltage is applied, so therefore element sizes are defined to increase from $-h < x < 0$ and decrease from $0 < x < h$. This procedure is defined in Ref. [10]. An example mesh with 100 elements and a refinement factor of $g = 1.1$ is shown in Figure 3.2.

Chapter 4

Cluster Pressures During Actuation

4.1 Solvent Transport

Due to the small sizes of the clusters and channels in Nafion (on the order of nanometers [18]), either the pore-flow model or the solution-diffusion model can be used to describe solvent transport in the membrane in response to a gradient in chemical potential. Some of the differences in applicability of the two models are summarized in Ref. [52]. The pore-flow model, with solvent flow primarily from a pressure gradient, is best suited to describe flow through membranes with large pores, i.e. pores which can be thought of as permanently existing in the material. The solution-diffusion model, with solvent flow primarily from a concentration gradient, is best suited to describe flow though membranes with small pores, where the pores are effectively represented by statistical fluctuations instead of existing permanently. The transition from the applicability of the solution-diffusion model to the pore-flow model occurs for pore sizes around 0.5 to 1.0 nm [52]. The effective pore sizes of Nafion are just above this range [53], and so either model can be applied with reasonable results. However, especially in describing treated membranes with improved transport characteristics, the pore-flow model is found to explain experimental data more accurately with relatively simple modeling considerations [53], and it is most commonly used to model solvent transport in Nafion. Additionally, since the assumed mechanism of actuation is solvent transport due a pressure gradient, the pore-flow model is readily applied to the actuation of an IPT. A relationship between the diffusion coefficient and the hydraulic permeability of the solvent in Nafion can be derived if it is assumed that the activity coefficient of the sol-

vent is constant and the mechanism for solvent movement is the same whether the chemical potential gradient is from a pressure difference or concentration difference [54]. Here, these assumptions are not evaluated and the hydraulic permeability is used to describe solvent flux in the membrane.

Using the pore-flow model, Darcy's law is used to relate solvent flux to the pressure gradient in the membrane:

$$v_s = -K_s \frac{\partial P_c(x,t)}{\partial x} \tag{4.1}$$

where v_s is solvent velocity, K_s is the hydraulic permeability of the solvent, and P_c is the total internal cluster pressure which consists of osmotic and electrostatic components. The hydraulic permeability is characteristic of both the solvent and the membrane, since it depends on the pore sizes and pore connectivity in the membrane as well as the dynamic viscosity of the solvent. Electrostatic interactions are dominant in determining the overall actuation response, so the electrostatic component of cluster pressure will be the largest.

4.2   Osmotic Pressure

To calculate osmotic pressure, consider an isothermal process and first note that the Gibbs free energy must be at a minimum in order to have equilibrium:

$$dG = VdP + \mu_s dn_s + \mu_+ dn_+ + \mu_- dn_- = 0 \tag{4.2}$$

where G is the Gibbs free energy, V is volume, P is pressure, n_i is the number of particles of species i, and the subscripts s, $+$, and $-$ refer to solvent, cations, and anions respectively. Consider a system where the total number of ions is constant, and a semi-permeable membrane separates the electrolyte solution from pure solvent. In this case, the pressure P that must be applied to restrict the flow of solvent molecules across the interface is the osmotic pressure, and Eq. 4.2 yields

$$\Pi = -\frac{RT}{V_s} \ln a_s \tag{4.3}$$

where Π is osmotic pressure and V_s is the partial molar volume of the solvent. The activity of the solvent in the clusters varies with the mole fraction of solvent:

$$a_s = \gamma_s \frac{n}{n+1} \tag{4.4}$$

where $n = c_s/c_+$ is the number of solvent molecules per cation in the cluster. The concentration of solvent molecules with respect to solvent uptake is calculated as

$$c_s = \frac{1}{V_s} \frac{w}{w+1} \tag{4.5}$$

where w is the solvent uptake defined in Eq. 3.5. Since the anions are fixed, they do not contribute to the activity of the solvent in this representation. Assuming $\gamma_s = 1$, the osmotic pressure is expressed as

$$\Pi = \frac{RT}{V_s} \ln \frac{n+1}{n} \tag{4.6}$$

For a dilute solution, expanding Eq. 4.6 in a Taylor series and keeping 1$^{\text{st}}$ order terms yields the analogy of the Morse equation for the system:

$$\Pi_{dilute} = RTc_+ \tag{4.7}$$

In Ref. [12], this equation was used to calculate osmotic pressure. However, since the cluster system does not actually resemble a dilute solution, here Eq. 4.6 is used in the actuation model.

4.3 Electrostatic Pressure

Recall that the anions are assumed to be distributed on the surface of the clusters - see Figures 2.1 and 2.2. The anion surface charge density of a cluster is calculated to be [12]

$$q = \frac{\rho_b F}{3EW} \frac{a}{w} \tag{4.8}$$

where a is the cluster radius as shown in Figure 2.2. Eq. 4.8 assumes that the number of ionic groups per cluster stays constant as the cluster expands or contracts. The normalized ion charge density in the polymer is defined to be

$$Q = \frac{c_+ - c_0}{c_0} \tag{4.9}$$

To quantify electrostatic interactions, the effective local permittivity of the cluster must also be determined. When water is used as the solvent it will first fill up the hydration shells of

the ions as it enters the clusters. Once these hydration shells are full, free water will exist in the cluster. Of course, an exact representation would require statistical mechanics, but this simplified description is a good qualitative representation of the actual behavior. When a water molecule is locally oriented by a strong electric field, such as that in the hydration shell of an ion, it will no longer be polarized by externally applied fields and its permittivity will decrease. Therefore, the cluster can be considered as a two-phase mixture of bound and free water when calculating the local permittivity. When an ionic liquid is used as solvent, the ionic liquid will not associate with the ions as water does. However, water still exists in the membrane from an equilibrium with the relative humidity of the environment - this point is discussed further in Sections 6.2.1 and 7.1. Additional water is also absorbed by the ionic liquid: Li et al. [55] found that on the order of 1 water molecule per ionic liquid molecule is absorbed by EMI-Tf ionic liquid in a Nafion membrane at room temperature and ambient atmospheric humidity (40-60% relative humidity). The cluster can be considered a two-phase mixture of ionic liquid and water. Assuming spherical inclusions of water embedded in a matrix of ionic liquid, the effective permittivity is given by the Maxwell-Garnett mixing formula,

$$\epsilon = \epsilon_1 \left(\frac{2\epsilon_1 + \epsilon_2 - 2f(\epsilon_1 - \epsilon_2)}{2\epsilon_1 + \epsilon_2 + f(\epsilon_1 - \epsilon_2)} \right) \tag{4.10}$$

where ϵ_1 and ϵ_2 are the permittivity of the ionic liquid and water, respectively, and f is the volume fraction of water. Since only a small amount of water exists, it is assumed that it all exists in the hydration shells of the counter-cations when evaluating Eq. 4.10. For a Li^+ ion, the water in its hydration shell is calculated to have a permittivity of $\sim 7.5\epsilon_0$, where ϵ_0 is the permittivity of free space [56]. Thus, in the model $\epsilon_2 = 7.5\epsilon_0$ and $\epsilon_1 = 15.1\epsilon_0$ when EMI-Tf ionic liquid is used [57]. When water is used as the solvent, the system is modeled considering spherical inclusions of free water embedded in a matrix of bound water, so ϵ_1 and ϵ_2 correspond to bound and free water, respectively. For more details on the derivation of Eq. 4.10, see either of Refs. [58, 59, 60][1].

In the absence of an applied voltage the cation-anion pairs in a single cluster can be considered to form dipoles. These dipoles on the surface of the cluster are assumed to point radially outward. To determine the effective pressure from this configuration, the system is approximately represented as two spheres separated by a distance α and each containing a total charge of $4\pi a^2 q$. Let the sphere at $r = a$ be positively charged, corresponding to the cations, and the sphere at $r = a + \alpha$ be negatively charged, corresponding to the anions. If

---

[1]Note that Eq. (B5) of Ref. [60] contains a typographical error. Eq. 4.10 is the correct expression.

there is zero net charge, the system is analogous to a spherical capacitor and there will only be an electric field for $a < r < a + \alpha$. The energy of the distribution is given by [46]

$$W = 2\pi\epsilon \int_0^\infty r^2 E^2 dr \qquad (4.11)$$

where the electric field vector, $\mathbf{E}$, only has a radial component, and $E = |\mathbf{E}|$. Considering a continuous charge distribution, the integral in Eq. 4.11 exists over all space. The force acting on the surface of the cluster is the change in configuration energy with respect to a change in the cluster radius:

$$\mathbf{F} = -\frac{dW}{da} \qquad (4.12)$$

The force only has a radial component, so from now on it will be simply written as F instead of $\mathbf{F}$. The effective pressure that will tend to either expand or contract the cluster is now expressed as the force divided by the surface area, resulting in

$$P_{sc} = \frac{q^2}{2\epsilon}\left[1 - \frac{a^2}{(a+\alpha)^2}\right] \qquad (4.13)$$

This pressure arises because the potential energy of the cluster will decrease as the radius of the cluster increases. Therefore, there is an effective pressure that tends to expand the cluster as the system attempts to reach a state of minimum potential energy. The distance between charge distributions, α, can be taken as an effective dipole length, or more generally as a representation of electrostatic interactions in the absence of an applied voltage. Note that the assumption of radial dipoles is key in deriving Eq. 4.13. Numerical simulations show that the distribution of dipoles on the surface of a sphere which minimizes free energy actually leads to dipoles with zero radial component [61]. However, steric effects from the alignment of polymer side chains to form the cluster will give the dipoles a radial component. Assuming completely radial dipoles is analogous to assuming that steric effects from polymer chain alignment play a large role in cluster formation, such that the dipoles will align with a significant radial component. At sufficient solvent uptakes, the clusters will be large and contain enough ionic groups such that this assumption is justified. The effective pressure when the dipoles are not completely radial can only be calculated numerically, since the dipole moment distribution will not be uniform.

Using an estimated cluster radius of $a = 1.6$ nm [12] and considering discrete charges, Eq. 4.8 yields ~ 38 anions on the surface of a typical cluster. Since the number of ions in the system

(a) 50 ion pairs   (b) 500 ion pairs
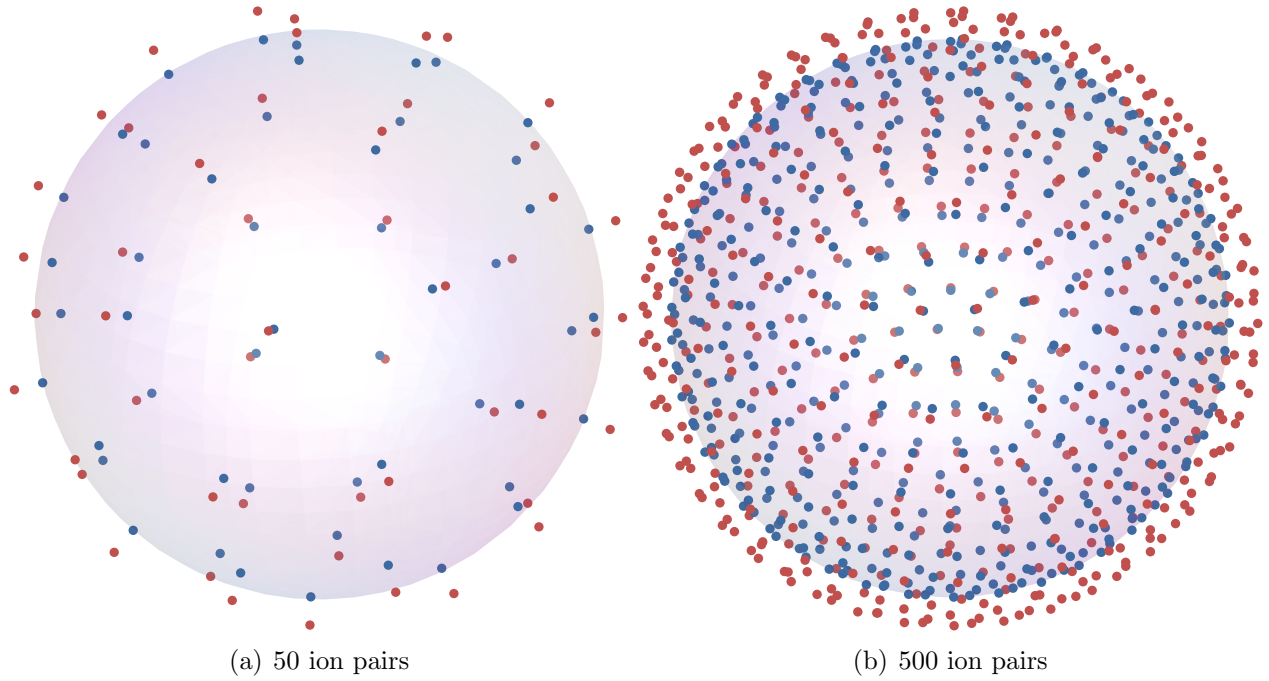
Figure 4.1: Quasi-uniform distributions of ions (shown as point charges) forming radial dipoles on the surface of a sphere, showing 50 and 500 ion pairs. The ratio of the radius to the ion-pair charge separation length is $\beta = 10$.

is small, there is question as to whether the analytical expression in Eq. 4.13 obtained by assuming a continuous charge distribution is accurate in describing electrostatic interactions in a cluster. To test this, numerical simulations were performed considering radial dipoles distributed on the surface of a sphere. First, note that a uniform distribution of points on a sphere only exists for a number of points which corresponds to the number of vertices or faces of the regular polyhedra. However, any number of points can be quasi-uniformly distributed on the surface of a sphere using an algorithm given by Saff and Kujilaars [62]. Quasi-uniform means that the distribution may not give the absolute minimum in potential energy, but it will be very close. Following the derivation of Eq. 4.13, this was used to place a given number of cations on the surface of a sphere. The anions were placed radially outward at a distance of α from the cations, shown in Figure 4.1. To proceed, the analysis is simplified by defining the non-dimensional parameter $\beta = a/\alpha$. Because the system is linear, superposition can be used and the energy and the total force from Eqs. 4.11 and 4.12 can be non-dimensionalized and re-written only in terms of β. Considering the continuous charge distribution described

above, this leads to the non-dimensionalized energy

$$W^* = W \left(\frac{Q_0^2}{4\pi\epsilon a} \right)^{-1} = \frac{1}{2(\beta + 1)} \tag{4.14}$$

where $Q_0 = 4\pi a^2 q$ is absolute value of the total anion charge on the surface of a cluster. The total non-dimensionalized force, which is distributed uniformly on the surface of the cluster due to symmetry, is expressed as

$$F^* = F \left(\frac{Q_0^2}{4\pi\epsilon \alpha^2} \right)^{-1} = \frac{2\beta^2 + 1}{2 \left(\beta^2 + \beta \right)^2} \tag{4.15}$$

These definitions are made for convenience for comparing with the numerical results. For the discrete system, the total configuration energy is calculated with

$$W_n^* = \sum_{i=1}^{n} \sum_{j=i+1}^{n} \frac{e_i^* e_j^*}{r_{ij}^*} \tag{4.16}$$

where n is the total number of ions, $e_i^* = e^i/Q$ is the normalized charge of the ith ion, and $r_{ij}^* = r_{ij}/a$ is the normalized distance between ions i and j. Values of the energy were calculated varying β for different numbers of ions in order to compare the discrete calculations to the continuum approach.

To calculate the total force numerically by applying Eq. 4.12, care needs to be taken in using Eq. 4.16, since this equation was multiplied by the cluster radius a in the non-dimensionalization. Considering this and re-writing the derivative in Eq. 4.12 in terms of β and then using the chain rule leads to

$$F_n^* = \frac{W_n^*}{\beta^2} - \frac{1}{\beta} \frac{dW_n^*}{d\beta} \tag{4.17}$$

The second term can be evaluated numerically using the finite element method, leading to

$$F_n^* = \frac{W_n^*}{\beta^2} - \left(M^\beta \right)^{-1} K^\beta W_n^* \tag{4.18}$$

The finite element matrices are defined as

$$M_{AB}^{\beta} = \int_{\beta_1}^{\beta_n} L_A L_B d\beta \tag{4.19}$$

$$K_{AB}^{\beta} = \int_{\beta_1}^{\beta_n} L_A \frac{dL_B}{d\beta} \beta^{-1} d\beta \tag{4.20}$$

where L_A are the Lagrange interpolation functions and the interpolation is done over the parameter space $\beta_1 \leq \beta \leq \beta_n$.

The comparison between the continuous and the discrete calculations for energy and force is shown in Figure 4.2. From this it is seen that the results of force and energy for the discrete system are less than that of the continuous system, converging as the number of ions becomes very large. So, using Eq. 4.13 in the model will tend to overpredict the electrostatic component of cluster pressure, in comparison with the cluster system that the equation is intended to describe. A more direct comparison is shown in Figure 4.3, where F_n/F is plotted as a function of β for $n = 38$ and $n = 5000$. This plot shows that the discrete results do not just differ by a constant - the relationship of F_n with β is also slightly different, especially when n is small. Since a generalized expression for cluster pressure as a function of net cluster charge is needed for modeling actuation (these expressions are derived below), the analytical expression based on the continuum assumption is used in the model. This approximation should be kept in mind when examining the model results. However, also note that a spherical cluster with perfectly radial dipoles is a modeling abstraction, not an exact representation of the cluster system. This means that both the discrete and continuum calculations discussed above are both approximations to the cluster system, and that the best relationship for F vs. β would have to be obtained using molecular dynamics or Monte Carlo simulations considering polymer backbone deformation, cluster size, shape, and ion alignment, and the interaction with solvent that causes the cluster to expand. The use of Eq. 4.13 (and the generalized expression, Eq. 4.22) in the model can be evaluated by comparing basic model predictions with experimental results. Since it is found that the use of these equations leads to reasonable model predictions, it can be assumed that these equations are a good approximation to electrostatic cluster pressure and that they capture the essential mechanisms of actuation.

At higher levels of solvent uptake the cations will become dissociated from the fixed anion sites on the cluster surface. FTIR studies of solvated Nafion systems have confirmed this
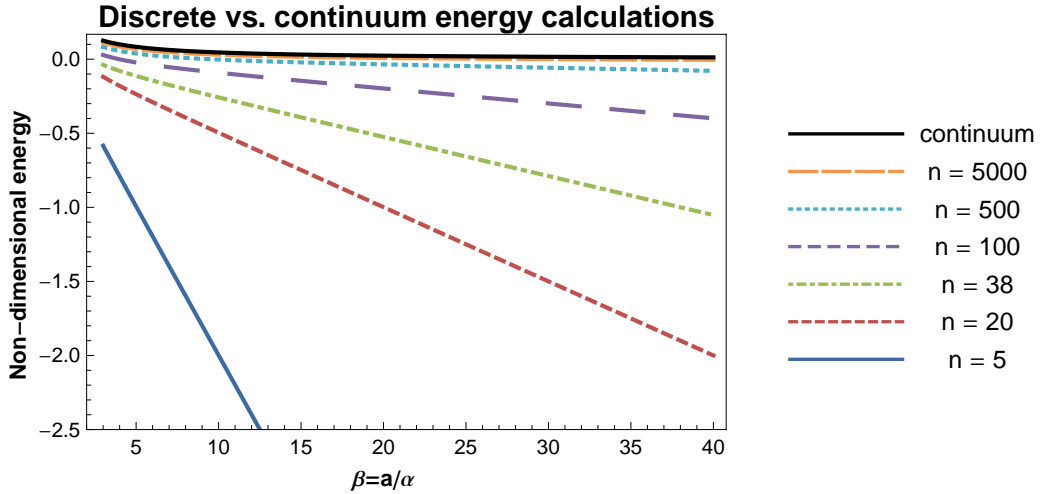
(a) Comparison of continuum (Eq. 4.11) and discrete (Eq. 4.16) energy calculations, varying the number of ions for the discrete calculation.
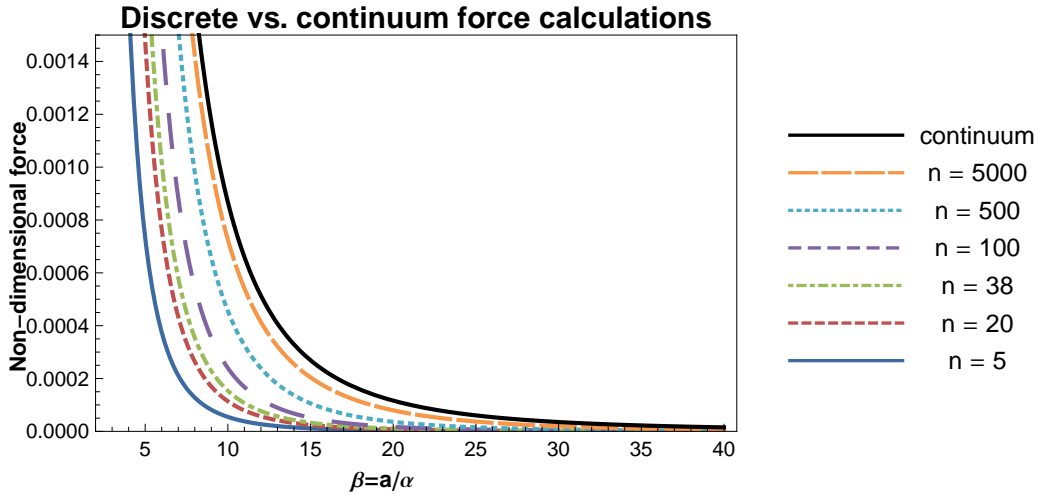
(b) Comparison of continuum (Eq. 4.12) and discrete (Eq. 4.17) calculations for net cluster electrostatic force, varying the number of ions for the discrete calculation.

Figure 4.2: Comparison of calculations for energy 4.2(a) and force 4.2(b) using continuum and discrete approaches, varying the number of ions. The calculations are plotted as a function of the non-dimensional parameter $\beta = a/\alpha$. The results converge as n becomes large.

Discrete divided by continuum force calculations
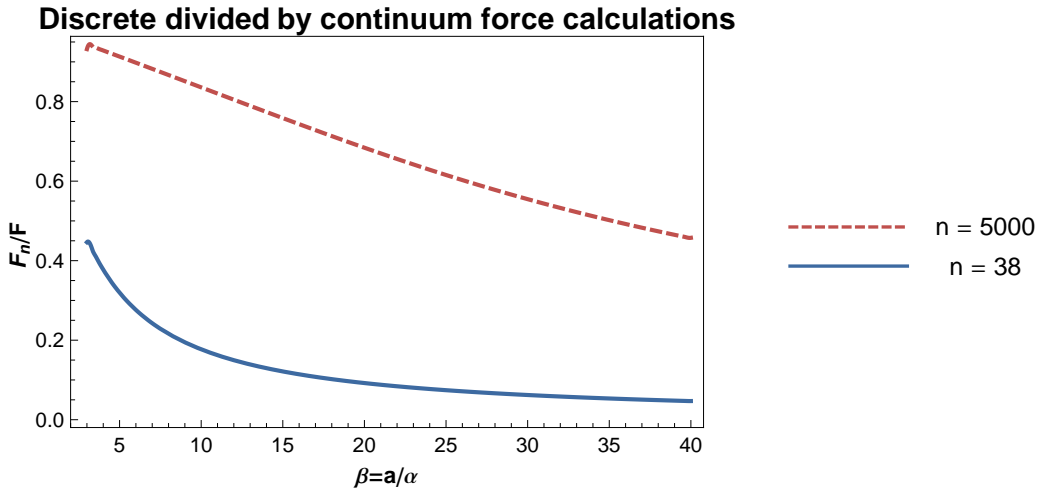
Figure 4.3: Net cluster electrostatic force calculated using 38 and 5000 ions divided by that calculated using a continuum approach, plotted as a function of the non-dimensional parameter $\beta = a/\alpha$.

behavior for several different cationic species [15, 63, 64]. Now, α is better described as a mean separation between cations and anions, or effective dipole length, since the dissociated ions do not form true dipoles. As more cations are dissociated from the fixed anion sites α will increase, reaching a maximum when all cations are dissociated at high levels of solvent uptake (i.e. solvent uptakes above the critical uptake). To visualize these ionic interactions, consider an anion and a cation as shown in Figure 4.4(a). The two ions will align with their charge centers as close as possible in order to maximize the favorable Coulombic interaction between oppositely charged particles. Approximating the ions as spheres with the charge located at the center, this configuration would lead to a dipole length of the sum of each ion's radius. However, the sulfonate group on the side chains of Nafion is highly polarizable due to differences in electronegativities of the atoms, and the negative charge will be located mostly on the oxygen atoms since oxygen is more electronegative than sulfur. This means that the dipole moment length arising from an associated anion-cation pair will be less than the sum of the two radii, as shown in Figure 4.4(b). Because of the polarizability of the sulfonate group, the ionic bond is easily broken when a solvent is introduced, and the cation becomes dissociated. When there is complete dissociation water molecules will exist between the anion and the cation, shielding the electrostatic interactions between the ions. The separation between the ionic charges, or the effective dipole length, will now increase since the charge centers of the ions are further displaced, as shown in Figure 4.4(c). For an ionomer with a different functional group but in the same cation form, the magnitude and direction of the

(a) Effective dipole length approximating the ions as spheres with charge located at the center.

(b) Effective dipole length considering the polarizability of the anion.

(c) Effective dipole length when the cation is dissociated.
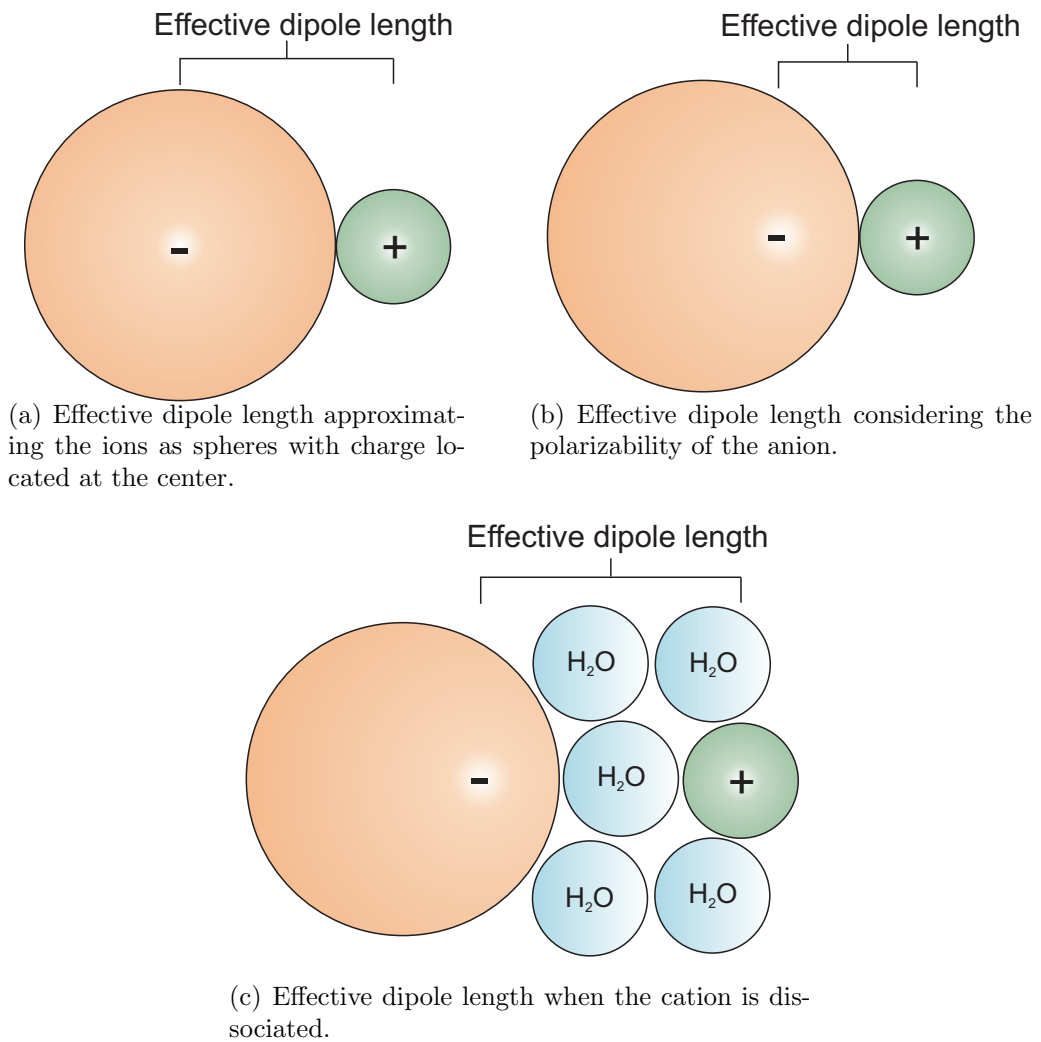
Figure 4.4: The effective dipole length for different representations of the anion-cation interaction in an ionic cluster of an ionomer.

effective dipole arising from ionic interactions will depend on the polarizability and size of the anion as well as steric constraints. The latter refers to the direction of alignment of the polymer side chains on the cluster surface. The effective dipole length α can be estimated using the simple considerations mentioned above, but detailed calculations which include all the different interactions would be required to quantify this value and compare for different systems.

During actuation, charge transport causes clusters to have a non-zero net charge. Specifically, clusters in the cathode boundary layer will have a net positive charge, and clusters in the anode boundary layer will have a net negative charge. To calculate the electrostatic pressure, a distribution of cations must either be calculated or assumed. Since these ionic interactions play a large role in determining the actuation response, an accurate representation is important. It is expected that the cations will tend to place themselves as close to the fixed anion sites as possible to maximize this favorable interaction. To test this hypothesis, a Monte Carlo simulation was performed to determine the equilibrium distribution of cations in a representative cluster. From the considerations mentioned above in the comparison of the discrete and continuum pressure calculations, 38 anions are placed on the surface of sphere with radius $a = 1.6$nm [12] using the quasi-uniform distribution algorithm given by Saff and Kujilaars [62]. The cations were initially given random positions inside the sphere and were allowed to move in order to minimize potential energy. 152 cations were placed inside the sphere, which corresponds to a cluster in the cathode boundary layer with $Q = 3$ (i.e. the net cluster charge is 3 times the total anion charge, see Eq. 4.9). The ions were assigned distances of closest approach corresponding to the ionic radii: 0.15 Å for Li$^+$ and an estimate of 1 Å for SO$_3^-$. Eq. 4.16 was used to calculate the total potential energy of the system. To proceed, the potential energy of the system is first calculated and the value is stored. Next, a random movement is given to a single cation and the potential energy of the system is calculated again. If the new potential energy is lower, the move is kept; if not, the cation is moved back to its original position. This process is applied to each cation, and repeated until the potential reaches a stable value.

A Mathematica program was written to perform the simulation. The results confirm what was expected, that the cations will move towards the surface of the cluster when allowed to reach equilibrium. This occurs because the cations will tend to maximize the favorable interactions with the oppositely-charged anions and minimize the interactions with other like-charged cations. Figure 4.5 shows the change in cation volumetric charge density and

(a) Initial cation charge density distribution (b) Equilibrium cation charge density distribution
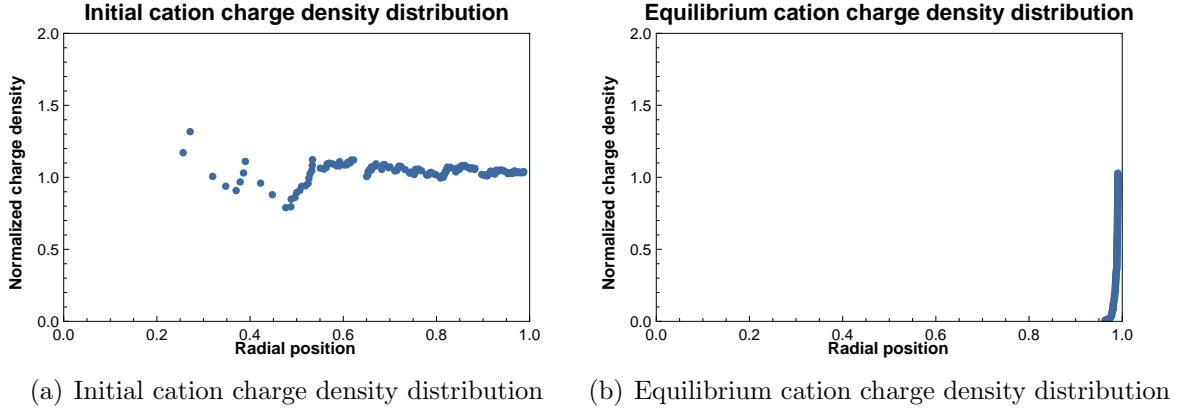
Figure 4.5: Monte Carlo simulation results showing charge density for a cluster with 38 fixed anions and 152 mobile cations. (a) Initial cation charge density after the cations are given random positions inside the sphere. (b) Equilibrium charge density distribution

Figure 4.6 shows the change in cation distribution from initial to final states (the fixed anions are not represented). The volumetric charge density in Figure 4.5 is plotted with respect to the radial distance from the center. For a cation located at radius r_k, the equivalent uniform volumetric charge density at r_k is calculated as the total number of cations with position $r \leq r_k$ divided by $\frac{4}{3}\pi r_k^3$.

When the cations are at their initial random positions, Figure 4.5(a) shows that this leads to a nearly constant variation in charge density with respect to radial position. Of course, since the initial positions are assigned at random, Figure 4.5(a) will look different for each run. However, when many runs are averaged, the average charge density will be constant with respect to the radial position. This is expected because the cations are initially assigned random positions in $\mathbb{R}^3$ (i.e. 3-dimensional space), and therefore the number of cations enclosed by a volume with radius r will vary directly with r^3. An animation of the Monte Carlo simulation is in Appendix D.5.

To calculate the pressure represented by the cation distribution in Figure 4.6(a), recall that there are also fixed anions distributed on the surface of the cluster. Due to the sizes of the cations and anions and their hydration shells they will not completely reach the surface of the cluster. Steric effects from polymer chain alignment on the surface of the cluster will also cause cation-anion dipole pairs to line up with a significant radial component. Let α be the average approach distance of the cations to the anions, with the anions placed at $r = a + \alpha$, as was done in deriving Eq. 4.13. It can now be said that the cations will have a constant

(a) Initial cation distribution   (b) Equilibrium cation distribution
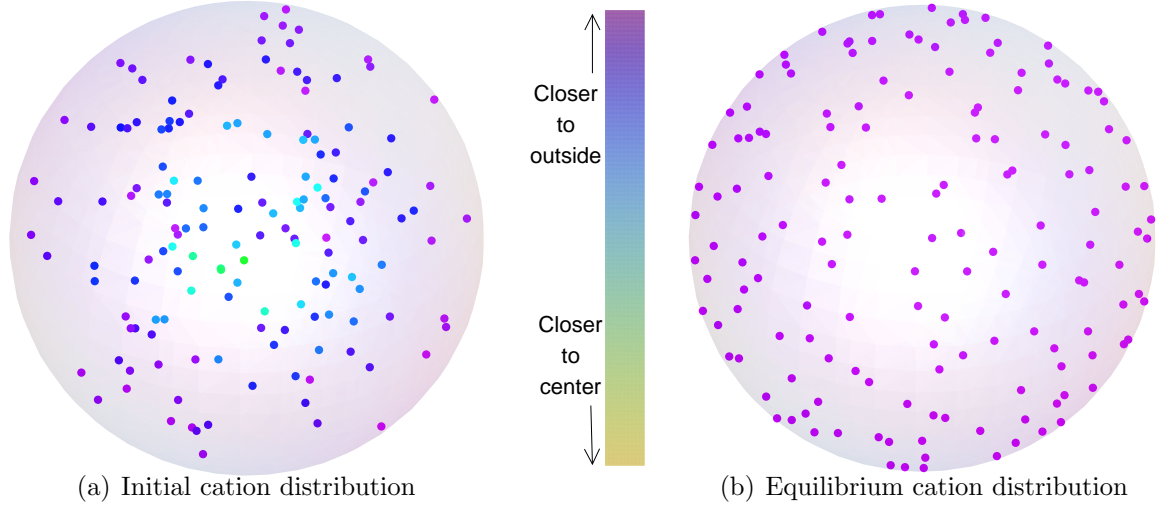
Figure 4.6: Initial (a) and final (b) cation distributions from the Monte Carlo simulation. Results show movement toward the outside of the cluster at equilibrium. The fixed anions on the surface of the sphere are not shown.

volumetric charge density for $0 < r < a$. To represent this mathematically, first define the absolute value of the total anion charge on the surface of a cluster as Q_0. Now, there are three regions with different expressions for the electric field: Region 1 from $0 < r < a$ where the enclosed charge at position r is $Q_0(Q+1)r^3/a^3$, region 2 from $a < r < a + \alpha$ where the enclosed charge is $Q_0(Q+1)$, and region 3 from $a + \alpha < r < \infty$ where the enclosed charge is $Q_0 Q$. With the electric field for these three regions, the pressure is calculated as force divided by surface area using Eqs. 4.11 and 4.12. The equation is also simplified using $Q_0 = 4\pi a^2 q$, yielding

$$P_{vol} = \frac{q^2}{2\epsilon} \left(Q^2 \frac{a^2}{(a+\alpha)^2} + (Q+1)^2 \left[\frac{6}{5} - \frac{a^2}{(a+\alpha)^2} \right] \right) \tag{4.21}$$

This pressure encompasses all of the electrostatic interactions when a volume charge density of cations is assumed.

From the simulation results shown in Figures 4.5(b) and 4.6(b), the cation-anion system at equilibrium can be considered as two surface charge distributions with a separation distance α. A derivation similar to that of Eq. 4.21 yields the associated pressure:

$$P_e = \frac{q^2}{2\epsilon} \left(Q^2 \frac{a^2}{(a+\alpha)^2} + (Q+1)^2 \left[1 - \frac{a^2}{(a+\alpha)^2} \right] \right) \tag{4.22}$$

In the limit as $\alpha \to 0$, Eqs. 4.21 and 4.22 both reduce to $q^2Q^2/2\epsilon$. Both equations also give the same pressure, $q^2/2\epsilon$, for the anode boundary layer where $Q = -1$. A more detailed derivation of Eqs. 4.21 and 4.22 is given in appendix B.

The change from a volume charge density of cations (Eq. 4.21) to an effective surface charge density (Eq. 4.22) can be mathematically described as follows. Consider cations moving into the cathode boundary layer. As the cations enter a cluster they will not be in an equilibrium configuration and the cluster can be considered to resemble Figure 4.6(a) with corresponding electrostatic pressure P_{vol}. As ions stop entering the cluster, the system will reach equilibrium as shown in Figure 4.6(b), and the resulting distribution will have corresponding electrostatic pressure P_e. The transition between these two states may thus be related to the rate at which ions are being added to the cluster. Assuming an exponential variation with respect to ion flux, this yields

$$P_{ion}(\dot{Q}) = (P_e - P_{vol}) \, e^{b\dot{Q}} + P_{vol} \tag{4.23}$$

where b is an empirical factor. This equation satisfies the conditions that $P_{ion} = P_e$ when $\dot{Q} = 0$ and $P_{ion} = P_{vol}$ when $\dot{Q} = \infty$. However, since ion flux will never reach ∞, a better expression can be obtained by requiring that $P_{ion}(B) = f_p P_{ion}(\infty)$ when $\dot{Q} = B$. Here, B is an empirical parameter and f_p is simply given a value less than one, e.g. $f_p = 0.95$. Applying this condition and simplifying leads to

$$P_{ion}(\dot{Q}) = (P_e - P_{vol}) \left(\frac{(1 - f_p) \, P_{vol}}{P_{vol} - P_e} \right)^{\left| \dot{Q}/B \right|} + P_{vol} \tag{4.24}$$

where the absolute value is added because both positive and negative ion fluxes would be expected to affect the local cation distribution in a similar manner.

The change between volume and surface charge densities described by Eq. 4.24 can be thought of as a physical description of a local micro-scale cluster phenomenon during actuation. However, this change is expected to happen very quickly, at a time scale much faster than the time scale of solvent transport and actuation. The complexity of Eq. 4.24 also prevents it from being of any use in forming a reasonable analytical model of electrostatic cluster pressures during IPT actuation. Therefore, Eq. 4.22 is used in the actuation model to represent electrostatic interactions. Finally, the total cluster pressure is expressed as the sum of osmotic and electrostatic components:

$$P_c = \Pi + P_e \tag{4.25}$$

In comparison with the cluster pressures used by Nemat-Nasser in Ref. [12], a few key differences in the current results should be noted. Here, the electrostatic cluster pressure is shown to vary with Q^2, while the cation-dipole pressure term used to describe electrostatic interactions in [12] varies with Q. This is an important distinction in terms of modeling the electromechanical coupling of IPTs and accurately representing the underlying actuation mechanisms. The use of an electrostatic pressure term that varies linearly with Q suggests that electromechanical coupling in IPTs is approximated well by assuming a linear relationship with charge transferred. Experimental results have shown that this is not the case; in Ref. [41] Leo et al. demonstrate that the dominant behavior at low actuation frequencies has a larger contribution from a nonlinear coupling term than from a linear one. The same nonlinear model of electromechanical coupling in Ref. [41] is also used by Wallmersperger [10], showing a good fit to a wide range of experimental data. The electrostatic cluster pressures derived in this chapter are consistent with these results, since the Q^2 dependence of cluster pressure suggests an electromechanical coupling mechanism to leading order that varies with Q^2.

Chapter 5

Actuation from Boundary Layer Expansion

5.1 Beam Bending Analysis and Linearization

When ions and solvent move into or out of the boundary layers, there will be expansion or contraction according to the corresponding volume changes of the ions and solvent in a cluster. Here, we follow Nemat-Nasser's approach [12] and consider the volumetric strains in a cluster to be eigenstrains, i.e. the strains would develop whether the cluster was embedded in a polymer matrix or not. Due to an equilibrium of forces, stress in the polymer matrix always balances the internal cluster pressure at the cluster boundary. Additionally, the matrix material is assumed to not impede the expansion/contraction of a cluster.

Since the volume of the mobile cations (Li^+ or Na^+) is small compared to the volume of the solvent molecules (either water or ionic liquid), it is assumed that volumetric expansion of a cluster is caused only by local changes in solvent uptake. Using true strain, the local volumetric strain e_v is related to the solvent uptake by

$$e_v = \ln\left(1 + w\right) \tag{5.1}$$

The assumption that volumetric strains are caused only by changes in solvent uptake will be relaxed in Section 5.3, when the finite volumes of the mobile cations are also considered as a source of volumetric expansion.
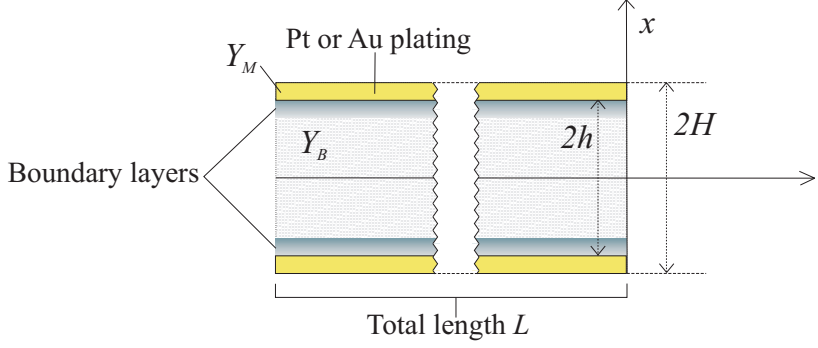
Figure 5.1: A representative cross-section of the IPT showing the metal layers and boundary layers.

The Euler-Bernoulli beam theory is used to derive an expression for the tip displacement rate based on the bending moment generated by boundary layer expansion. For a derivation, see Appendix C. The result is

$$\frac{\dot{u}}{L} = \frac{L}{4H^3\left(3Y_{IPT} - 2Y_B\right)} \int_{-h}^{h} xY_B(x,t)\frac{\dot{w}(x,t)}{1+w(x,t)}dx \tag{5.2}$$

where u is tip displacement and $\dot{u}$ is tip velocity, L is the length and Y_{IPT} is the modulus of the IPT, Y_B is the modulus of the bare polymer, and $2H$ and $2h$ are the thicknesses of the IPT and the bare polymer, respectively - see Figure 5.1 for a diagram of the system. In order to evaluate this expression, the solvent uptakes in the boundary layers need to be determined. First, note that the relevant continuity equation for solvent transport is

$$\frac{\partial e_v}{\partial t} + \frac{\partial v_s}{\partial x} = 0 \tag{5.3}$$

Solvent uptake can now be related to the pressure gradient in the membrane by combining Eqs. 4.1, 5.1, and 5.3:

$$\frac{\dot{w}\left(x,t\right)}{1+w\left(x,t\right)} = K_s\frac{\partial^2 P_c\left(x,t\right)}{\partial x^2} \tag{5.4}$$

Considering no solvent to move outside of the polymer region, the initial and boundary conditions are $w(x,0) = \bar{w}$ and $v_s(\pm h, t) = 0$.

This is a highly nonlinear problem due to the nature of the cluster pressures P_c, given in Eq. 4.25 as a combination of Eqs. 4.6 and 4.22, and a complete solution requires numerical methods. However, Nemat-Nasser [12] has shown that an approximate solution can be

obtained by assuming uniform solvent uptakes and pressures in the boundary layers. This approach is followed here.

Since solvent uptake will only vary in the boundary layers, the integral in Eq. 5.2 can be approximated with

$$\int_{-h}^{h} x Y_B(x,t) \frac{\dot{w}(x,t)}{1+w(x,t)} dx \approx h \left[\frac{Y_B(w_C) L_C \dot{w}_C(t)}{1+w_C(t)} - \frac{Y_B(w_A) L_A \dot{w}_A(t)}{1+w_A(t)} \right] \tag{5.5}$$

where w_C and w_A represent the solvent uptakes in the uniform linearized cathode and anode boundary layers. L_C and L_A are the effective lengths of the boundary layers which are determined from the equilibrium solutions of the Nernst-Planck/Poisson equations (see Nemat-Nasser [12] for more details), and second order terms in L_C and L_A have been ignored since $L_C/h \ll 1$ and $L_A/h \ll 1$. The modulus in the boundary layers is evaluated at the current value of solvent uptake. Eq. 5.4 is linearized by assuming uniform pressures in the boundary layers, leading to

$$\frac{\dot{w}_C(t)}{1+w_C(t)} \approx K_s \frac{P_{CBL}(t) - P_R}{L_C^2}$$
$$\frac{\dot{w}_A(t)}{1+w_A(t)} \approx K_s \frac{P_{ABL}(t) - P_R}{L_A^2} \tag{5.6}$$

where P_{ABL} and P_{CBL} are the pressures in the uniform linearized anode and cathode boundary layers and P_R is a reference pressure in the middle layer of the polymer, where charge density and solvent uptake do not change appreciably when a voltage is applied. Now, the tip displacement rate can be expressed in linearized form as

$$\frac{\dot{u}}{L} = \frac{L K_s Y_{BL} h}{4H^3 (3Y_{IPT} - 2Y_B)} \left[\frac{P_{CBL}(t) - P_R}{L_C^2} - \frac{P_{ABL}(t) - P_R}{L_A^2} \right] \tag{5.7}$$

The results of ion and solvent movement are accounted for in the boundary layer pressure terms P_{ABL} and P_{CBL}. Writing the equation in this form shows the explicit dependence on the effective pressures in the boundary layers. Also, a time derivative no longer appears on the RHS, which simplifies the process for solving numerically.

To evaluate Eq. 5.7, first solve for the time-dependent boundary layer solvent uptakes using Eq. 5.6, then use these values to express the boundary layer pressures with respect to time. An expression for the time dependent charge distribution in the membrane is still needed in

order to calculate the boundary layer pressures at a given time. In this linearized model, we assume uniform charge densities in both the anode and cathode boundary layers and express an approximate solution to the Nernst-Planck/Poisson equations for a single mobile ionic species (Eqs. 3.12, 3.13, and 3.14) as [12]

$$Q(x,t) \approx \Omega(x)g(t) \tag{5.8}$$

where the equilibrium charge distribution is approximated to be

$$\Omega \approx \left\{ \begin{array}{ll} L_A/L_C & h - L_C < x < h \\ 0 & -h + L_A < x < h - L_C \\ -1 & -h < x < -h + L_A \end{array} \right\} \tag{5.9}$$

and the temporal solution is

$$g(t) = 1 - e^{-t/\tau_C} \tag{5.10}$$

The charging time scale is defined as

$$\tau_C = \frac{\lambda h}{D_+} \tag{5.11}$$

where λ is the Debye length, defined in Eq. 3.11, and 2h is the thickness of the polymer as shown in Figure 5.1. This is quite a large simplification of the governing equations, but it captures the most essential mechanisms of charge transport during actuation when a single mobile species is considered - see Chapter 9 for complete numerical solutions of the NPP equations for different cases and a discussion of the results. Now, these expressions can be used to calculate the tip displacement of an IPT when a voltage is applied.

5.2   Free Air Actuation

An implicit assumption in the model to this point is actuation in a solvent bath, i.e. there is always solvent available to move into the boundary layers and into the inactive middle layer, such that the uptake in the middle layer stays constant. When actuated in air, the uptake in the middle layer of the polymer will decrease, since solvent in this layer will move into the cathode boundary layer (CBL). This will cause the local modulus and the effective pressure in the middle layer, P_R, to increase. If P_R increases, solvent uptake in the boundary layers

will decrease as is seen in Eq. 5.6. If the effective modulus of the middle layer increases with a decrease in solvent uptake, the displacement of the IPT will decrease.

To enforce conservation of mass of the solvent for free air actuation, it is imposed that the average solvent uptake through the thickness of the polymer is constant, i.e.

$$\bar{w} = \frac{1}{2h} \int_{-h}^{h} w(x) \, dx = const. \tag{5.12}$$

If Eq. 5.4 is solved numerically, imposing a zero-flux boundary condition will mean that Eq. 5.12 is always satisfied. To analyze this effect analytically, Eq. 5.12 can be expressed in a linearized form according to the linearized model presented by Nemat-Nasser [12]:

$$\bar{w} = \frac{1}{2h} \left(L_A w_A + L_M w_M + L_C w_C \right) \tag{5.13}$$

where L_M and w_M represent the length and solvent uptake of the middle layer of the polymer. The lengths of the anode and cathode boundary layers are determined from the equilibrium solution of the NPP equations [12], and w_A and w_C are determined using Eq. 5.6. Representative calculations for solvent uptake in the boundary layers of a Nafion-based IPT with EMI-Tf ionic liquid as solvent are shown in Figures 8.1(a) and 8.1(b). Solvent uptake in the CBL will increase to several times its initial value, and this causes the solvent uptake in the middle layer to decrease according to Eq. 5.13.

To incorporate this change into the actuation model, solutions are obtained for the solvent uptakes in both the anode and cathode boundary layers using a variable middle layer pressure, P_R. The length of the middle layer is calculated by subtracting the lengths of the boundary layers from the thickness of the polymer, $L_M = 2h - L_A - L_C$. The pressure and modulus of the middle layer are then evaluated at a solvent uptake of w_M, which depends on the solvent uptakes and relative lengths of the boundary layers.

5.3 Cation Dependent Volumetric Eigenstrains

The assumption in writing Eq. 5.1 was that the volumetric eigenstrains which develop in the boundary layers during actuation are only due to changes in solvent uptake. However, the cations that move into or out of the boundary layers have a finite volume and will also

contribute to the volumetric eigenstrains in the boundary layers. In Eq. 5.1, the ratio of final to initial volume is calculated as $V_{final}/V_{initial} = \left(V_{polymer} + V_{solvent}\right)/V_{polymer} = 1 + w$ using the definition of solvent uptake in Eq. 3.5. The volume of the cations is thus included by making the modification $V_{final} = V_{solvent} + V_{polymer} + V_{cations}$, where $V_{cations}$ is calculated as the difference in number of cations from the initial equilibrium state times the effective volume of a single cation, V_{1c}. In the model framework, this is calculated as

$$
\begin{aligned}
V_{cations} &= N_A V_{1c} \left(c_+ - c_0\right) \left(V_{polymer} + V_{solvent}\right) \\
&= \frac{N_A V_{1c} \rho_b Q}{EW(1 + w)} \left(V_{polymer} + V_{solvent}\right)
\end{aligned}
\tag{5.14}
$$

where N_A is Avogadro's number and the definitions of Q and c_0 in Eqs. 4.9 and 3.4 are used. Now, plugging in and simplifying leads to the new expression for volumetric strain:

$$
e_v = \ln\left(1 + w + \chi Q\right) \qquad \chi = \frac{N_A V_{1c} \rho_b}{EW}
\tag{5.15}
$$

where χ is a non-dimensional factor which depends on the volume of the counter-cation. When there is more than one mobile charge carrier, the volumetric eigenstrains due to ion movement won't simply depend on charge density as shown in Eq. 5.15 - the concentrations of each ion will need to be considered.

Eq. 5.15 is now used to calculate the bending moment rate due to changes in volumetric expansion:

$$
\dot{M}_{BL} = \frac{1}{3} \int_{-h}^{h} Y_B(x,t) x \left(\frac{\dot{w}(x,t) + \chi \dot{Q}(x,t)}{1 + w(x,t) + \chi Q(x,t)}\right) dx
\tag{5.16}
$$

By linearizing and using Eqs. 5.8, 5.9, and 5.10 for charge density, the resulting expression for tip velocity is

$$
\frac{\dot{u}}{L} = \frac{h L L_A Y_{BL}}{4H^3 \left(3Y_{IPT} - 2Y_B\right)} \left[\frac{K_s L_A^{-1} L_C^{-1} \left(1 + w_C\right)\left(P_{CBL} - P_R\right) + \chi \dot{g}(t)}{1 + w_C + \chi \frac{L_A}{L_C} g(t)} \right.
$$
$$
\left. - \frac{K_s L_A^{-2} \left(1 + w_A\right)\left(P_{ABL} - P_R\right) - \chi \dot{g}(t)}{1 + w_A - \chi g(t)}\right]
\tag{5.17}
$$

When $\chi = 0$, Eq. 5.17 simplifies to the previous expression for tip velocity, Eq. 5.7. Table 5.1 shows values of χ for different ions. For a small cation such as Li$^+$ or Na$^+$, χ is small and the

Ion form	χ
Li^+	0.0020
Na^+	0.0049
K^+	0.012
Rb^+	0.016
Cs^+	0.021
TBA^+	0.49
EMI^+	0.12
Tf^-	0.095

Table 5.1: Values of the ion-size parameter χ for IPTs in different ion forms.

volume of the cation does not make a significant contribution to tip displacement predictions. However, the use of large ions like as TBA^+, EMI^+, or Tf^- leads to a significant change in model predictions. A value of χ for Tf^- is calculated simply for comparison purposes; an anion-exchange membrane would need to be used in order to actually have an anion as the main mobile charge carrier.

Chapter 6

Modulus of Nafion With Respect to Ionic Liquid Uptake

6.1 Mechanical Properties of Nafion

For polymers (without functional ionic groups), the modulus depends on the molecular weight, chain interactions, and the degree of crosslinking. For viscoelastic materials, certain interactions also have an associated rate dependence. Physical models have been formulated to describe the mechanical properties of many polymer systems - see Refs. [65, 66, 67] for an introduction. In an ionomer, the electrostatic interactions cause micro-phase separation and the formation of ionic clusters, which has a definite effect on the mechanical properties of the material. The presence of ionic groups also complicates the prediction and interpretation of the mechanical behavior of an ionomer, since typical polymer models are no longer directly applicable. Here, a brief overview of previous studies on the mechanical properties of Nafion is presented, focusing on those which deal specifically with the effects of solvent content.

Nafion and other ionomers have been shown to have two different glass transition temperatures due to ionic clustering and micro-phase separation. The polymer matrix phase and the cluster phase each has a transition associated with it, and the water content will affect the temperature at which the transitions occur [18, 68]. The dynamic mechanical response is also dependent on the size of the counterion because of the different electrostatic interactions [18, 69, 70].

To model IPT actuation, the tensile modulus as a function of solvent content is of interest. Empirical relations have been reported for the modulus of Nafion as a function of water content and equivalent weight [71, 72]. Other studies have measured the modulus of Nafion in different cation forms, showing that the modulus decreases with solvent content and increases with the size of the counterion [73, 74]. In Ref. [73] mechanical tests were also performed using non-aqueous solvents, but conclusions could not be made in regards to how the nature of the solvent affects the mechanical properties. Several models have been proposed to describe the relationship between modulus and solvent uptake for Nafion [12, 75, 76, 77], and a more complete relationship between modulus and water content has been measured by using a humidity chamber [12, 77, 78, 79]. The primary goal of this study is to look at the relationship of modulus/solvent content when an ionic liquid is used, and to investigate whether the ionic liquid changes the behavior as compared to a water-based system.

6.2 Experimental

6.2.1 Preparation

There are many factors which impact the performance of Nafion, including the manufacturing technique (casting vs. extrusion), time history of thermal exposure, handling considerations, and the method of solvent absorption. The latter is known as Schroeder's paradox, which refers to the difference in absorption for a polymer when using a liquid solvent versus its saturated vapor. However, recent work has suggested that the paradox can be eliminated by careful consideration of the thermal history of Nafion and strict temperature control during experiments [80]. For the experiments performed here, care was taken to give all the samples the same pre-treatment in order to minimize extraneous effects. Samples of Nafion 117 were obtained from Ion-Power.com and were cut into 5x20 mm sizes. Next, the samples were boiled in 1M H_2SO_4 for 30 minutes for purification and proton exchange, and then were soaked in de-ionized water for 2 hours. A 0.5 M solution of LiOH was prepared and the samples were placed in this solution with stirring for 8 hours at room temperature. The samples were then rinsed with de-ionized water, placed between pieces of filter paper, and placed in a vacuum of $\sim$ 30 torr (at room temperature) for 16 hours. Previous work has demonstrated that drying Nafion in a vacuum at room temperature until equilibrium is reached will lead to a water content of $n^w = 1$, where n^w refers the number of water molecules

per sulfonate group [81, 82]. Therefore, it was assumed that the measured "dry" state had $n^w = 1$, and this was taken into account in the data reduction. The membranes were taken out of the vacuum oven and immediately weighed to obtain a dry mass. Next, the samples were distributed to jars and allowed to sit for 2 days to equilibrate with room humidity. After this time it was found that the water content was no longer changing, so equilibrium was assumed. The samples were weighed to take an equilibrium mass, and this was used to obtain an estimate of the water content. Now, the various samples were soaked in 1-ethyl-3- methylimidazolium trifluoromethanesulfonate (EMI-Tf) ionic liquid (EMD Chemicals) at room temperature for various times in order to obtain different ionic liquid uptakes. Note that higher ionic liquid uptakes can be obtained with heating, but this was not done in order to keep the thermal histories of each sample equivalent. The samples were weighed in order to quantify the ionic liquid content, and were also weighed again immediately before testing (1-3 days). The difference in mass for these two measurements divided by the dry mass of each sample was calculated to be 0.00433 ± 0.0126, which confirms that the samples were indeed in equilibrium with room conditions. It should be noted that water also exists in the neat ionic liquid, and its presence will generally decrease the viscosity, increase the conductivity, and decrease the electrochemical window of the ionic liquid [83]. Recently, experimental results using in situ proton NMR have shown that on the order of 1 water molecule per ionic liquid cation-anion pair will exist in Nafion swollen with ionic liquid in addition to the equilibrium water content of the membrane [55]. This was also accounted for in the results.

6.2.2 Experimental Procedure

Uniaxial tension tests were performed on a setup consisting of a linear stage (Newmark Systems NLS4) with a 1 kg load cell (Transducer Techniques GS0-1K). The setup is shown in Figure 6.1. Samples were placed in the clamps and centered, leaving a gauge length of 10 mm. Since a standard die was not used in cutting the samples and the samples were also now swollen with ionic liquid, the width of each sample was measured with an electronic caliper before testing. A very slow strain rate, 2.5×10^{-4} s^{-1}, was used in testing in order to ensure a quasi-static response. The samples were stretched past the yield point, although only the initial linear regime was used to calculate the results and is of interest for IPT actuation. Data was recorded using a National Instruments data acquisition system (DAQ) with an interface through LabView.
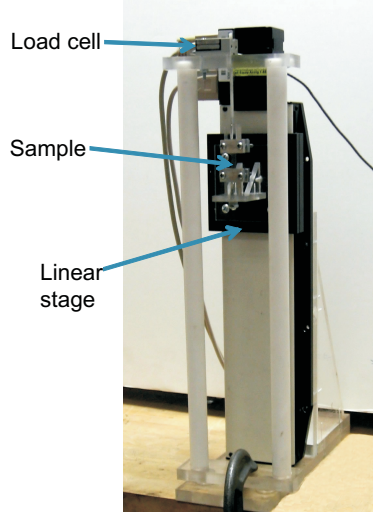
Figure 6.1: The uniaxial tension-test setup used for testing

6.3   Modeling of Modulus vs. Uptake

In this section, a micromechanical model developed by Nemat-Nasser [12] is described to model the relationship of modulus vs solvent uptake. The model in Ref. [12] is modified to include results from Chapter 4 where appropriate.

To begin, the microstructure is taken to be described by the Gierke and Hsu cluster-network model [27] and a representative volume element (RVE) is chosen which consists of a spherical cluster embedded in a spherical matrix of polymer backbone material - see Figure 2.2 and Section 2.2 for more detail. The polymer backbone material is modeled as a continuum, and the stress due to cluster expansion and polymer matrix deformation is determined using a neo-Hookean model:

$$\sigma_I = \frac{1}{3} Y \lambda_I^2 - p_0 \tag{6.1}$$

where Y is the effective Young's modulus of the polymer backbone material, λ_I is the principal stretch in the Ith direction, and p_0 is a hydrostatic pressure. Using incompressibility and rewriting in spherical coordinates yields the radial and hoop stresses [12]

$$\sigma_r = \frac{1}{3} Y \lambda_\theta^{-4} - p_0 \tag{6.2}$$

$$\sigma_\theta = \frac{1}{3} Y \lambda_\theta^2 - p_0 \tag{6.3}$$

where $\lambda_\theta = r/r_0$ is the hoop stretch for a material point initially at radius r_0 which moves to radial position r. These stresses are a function of the initial radial position r_0, which corresponds to a state where the membrane is completely dry. The initial porosity of the membrane is calculated as the ratio of the initial dry cluster volume to polymer backbone volume [12], $n_0 = (a_0/R_0)^3$. Assuming all solvent is contained in the clusters and that the number of ionic groups per cluster stays constant with swelling, the solvent uptake can be expressed using the RVE geometry as

$$w = \frac{a^3}{R_0^3 - a_0^3} \tag{6.4}$$

where a corresponds to the radius of the cluster at a solvent uptake of w.

The internal cluster pressure consists of osmotic and electrostatic components, as discussed in Chapter 4. For clarity, the relevant equations will be restated here. These cluster pressure expressions are different from those used in Ref. [12], where the approximation for a dilute solution is used for osmotic pressure (Eq. 4.7), and an approximate dipole-dipole interaction pressure is used to represent electrostatic interactions. Here, the osmotic pressure is calculated using

$$\Pi = \frac{RT}{V_s} \ln \frac{n+1}{n} \tag{6.5}$$

where $n = n^w + n^{IL}$ is the moles of solvent per mole cation and V_s is the partial molar volume of the solvent. Note that in the absence of an applied voltage, the concentration of cations is constant in the membrane and equal to the concentration of anions, so n can be taken as either moles solvent per mole cation or anion. Since there are both water and ionic liquid molecules in the system, n is a sum of both types of molecules and V_s is an average based on the amounts of each. Defining $\bar{w}^w$ as the average equilibrium water content in the membrane before the addition of ionic liquid, for $w \leq \bar{w}^w$, $n^{IL} = 0$ and $V_s = V_w$. When $w > \bar{w}^w$, assuming that ionic liquid and water molecules are added in a 1:1 fashion leads to the expressions

$$n^{IL} = \frac{\beta EW}{\rho_B} (w - \bar{w}^w)$$
$$n^w = \bar{n}^w + n^{IL} = \frac{EW}{\rho_B} \left(\frac{\bar{w}^w}{V_w} + \beta (w - \bar{w}^w) \right) \tag{6.6}$$

where $\beta = (V_{IL} + V_w)^{-1}$ and $\bar{n}^w$ refers to the average equilibrium number of moles water

per moles cation before ionic liquid is added. The partial molar volume of the mixture of water/ionic liquid molecules when $w > \bar{w}^w$ is expressed as

$$\frac{1}{V_s} = 2\beta \left(1 - \frac{\bar{w}^w}{w}\right) + \frac{\bar{w}^w}{V_w w} \tag{6.7}$$

The electrostatic component of cluster pressure is described solely by a spherical capacitor interaction pressure since no potential is applied to the membrane. From Section 4.3, this is expressed as

$$P_{sc} = \frac{q^2}{2\epsilon} \left[1 - \frac{a^2}{(a + \alpha)^2}\right] \tag{6.8}$$

At low solvent uptakes, the counter-cations will not all be dissociated from the fixed anionic sites, and therefore the effective dipole length α will vary with uptake. Since Eq. 6.8 is an approximate expression, α can be taken to be a representation of electrostatic interactions in the absence of an applied voltage rather than an actual physical length between an anion and a cation. Thus, the effective dipole length can be assumed to vary with solvent uptake and local permittivity as [12]

$$\alpha = \left(\frac{\epsilon}{\epsilon_1}\right)(\bar{\alpha}_1 w + \bar{\alpha}_2) \tag{6.9}$$

where ϵ is the effective local permittivity in the cluster, $\epsilon_1 = 15.1\epsilon_0$ is the permittivity of EMI-Tf ionic liquid [57], and the parameters $\bar{\alpha}_1$ and $\bar{\alpha}_2$ are fit to the experimental data. Since the cluster contains both ionic liquid and water molecules, ϵ is calculated to reflect this. Modeling the system as spherical inclusions of water in a matrix of ionic liquid, the Maxwell-Garnett mixing formula [58, 59, 60] is used to calculate the local permittivity:

$$\epsilon = \epsilon_1 \left(\frac{2\epsilon_1 + \epsilon_2 - 2f(\epsilon_1 - \epsilon_2)}{2\epsilon_1 + \epsilon_2 + f(\epsilon_1 - \epsilon_2)}\right) \tag{6.10}$$

where f is the volume fraction of water and $\epsilon_2 = 7.5\epsilon_0$, assuming that all the water in the system is in the hydration shells of the Li^+ ions [56].

Now, the boundary conditions are applied. The radial component of elastic stress must balance the internal cluster pressure at the cluster boundary:

$$\sigma_r(a_0) = -(\Pi + P_{sc}) \tag{6.11}$$

Additionally, equilibrium conditions require that the volume average of the stress tensor

must vanish when no external load is applied [12]. This is a homogenization step which leads to the expression

$$\frac{1}{V_{polymer}} \int \frac{1}{3} \left(\sigma_r + 2\sigma_\theta\right) dV_{polymer} = w \left(\Pi + P_{sc}\right) \tag{6.12}$$

where $V_{polymer} = 4\pi/3 \left(R_0^3 - a_0^3\right)$ is the volume of the polymer matrix material using the RVE geometry. Performing the integration in Eq. 6.12 and combining the results with Eqs. 6.2, 6.4, and 6.12 yields an expression for the modulus of the polymer with respect to solvent uptake:

$$Y(w) = \frac{\Pi + P_{sc}}{3} \frac{(1 + w)}{w_0 I_n - (w_0 I_n)^{4/3}}$$

$$I_n = \frac{1 + 2An_0}{n_0 \left(1 + An_0\right)^{1/3}} - \frac{1 + 2A}{\left(1 + A\right)^{1/3}} \qquad A = \frac{w}{w_0} - 1 \tag{6.13}$$

where n_0 is the initial porosity and w_0 is defined using Eq. 6.4 to be

$$w_0 = \frac{a_0^3}{R_0^3 - a_0^3} = \frac{n_0}{1 - n_0} \tag{6.14}$$

Chapter 7

Results - Modulus of Nafion With Respect to Ionic Liquid Uptake

7.1 Data Reduction and Test Results

A Mathematica program was written to process the test data and calculate the Young's modulus of the samples. First, the ionic liquid uptakes, w^{IL}, and the water uptakes, w^w, were calculated using the masses of the samples at the various measurement times. The total water uptake includes the measured uptake from room humidity equilibrium plus the assumed "dry" uptake of $n^w = 1$, plus the contribution from assuming one water molecule per EMI-Tf molecule. The uptake is defined the same way as in Eq. 3.5:

$$w_i^s = \frac{V_i^s}{V_{polymer}} \tag{7.1}$$

where the superscript s refers to water or ionic liquid, and i refers to the ith sample. Subtracting the ionic liquid water content, the average membrane water content was calculated to be $\bar{w}^w = 0.155 \pm 0.0196$.

Since swelling with a solvent will change the dimensions of the membrane, it was assumed that the thickness with respect to uptake is given by

$$t_i = t_0 \left(1 + w_i^{IL} + w_i^w\right)^{1/3} \tag{7.2}$$
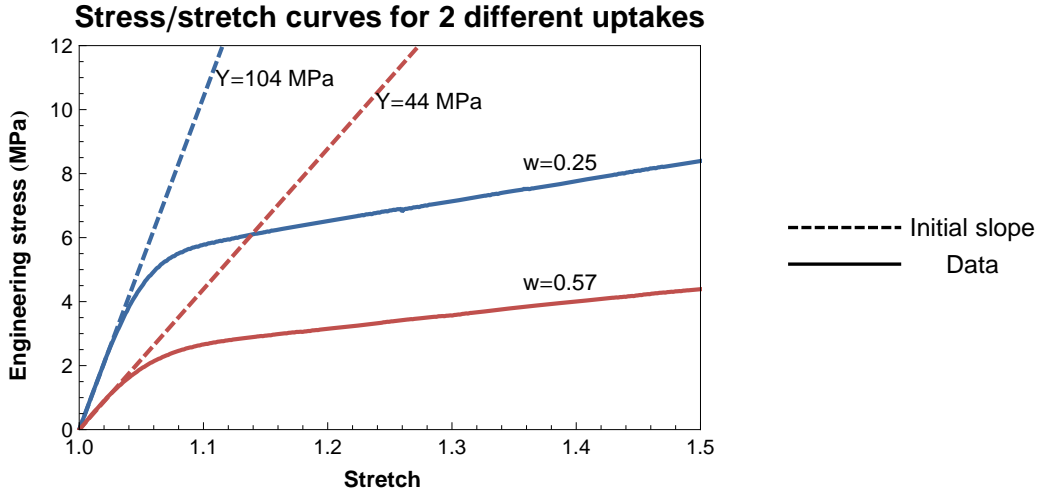
Figure 7.1: Stress/stretch curves obtained for samples with different solvent uptakes, which includes both water and ionic liquid content. The calculated Young's modulus for each sample is shown as a tangent line from the origin.

where t_i is the thickness of sample i and $t_0 = 178\mu m$ is the specification for dry thickness. The engineering stress in the x-direction along the length of the sample is calculated with

$$\sigma = \frac{F}{bt} \tag{7.3}$$

where F is the measured force and b is the width of the sample. The data was zeroed to the point of zero stress/strain using a dynamic graphical interface in Mathematica. The zero point was chosen for each sample by inspection, so a small human error is introduced into the data analysis. However, since the initial slope is the quantity of interest, this error was found to play a negligible role in the results, as was seen from sampling the points several times.

An example of stress/stretch data for samples with different uptakes is shown in Figure 7.1, along with the tangent lines showing the initial slope which represents the calculated Young's modulus. As expected, the sample with a higher uptake is softer. To calculate the modulus, a neo-Hookean model was fit to the initial linear region:

$$\sigma = \frac{1}{3}Y\left(\lambda - \lambda^{-2}\right) \tag{7.4}$$

where Y is the Young's modulus, λ is the stretch ratio, and σ is engineering stress. Eq. 7.4 is derived by applying boundary conditions for uniaxial tension and assuming incompressibility.
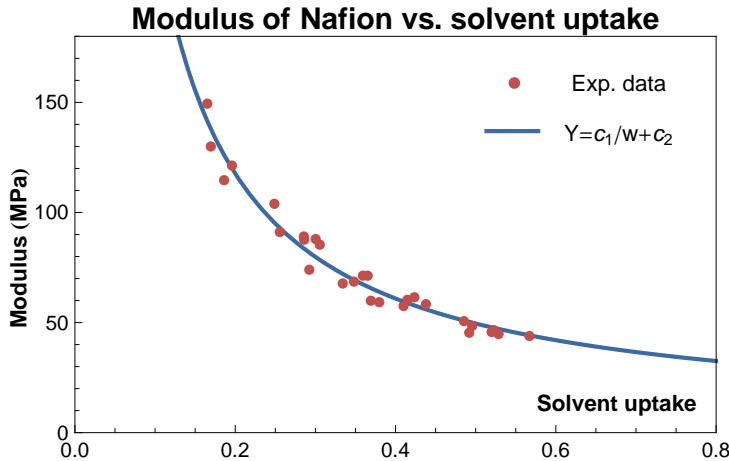
Figure 7.2: The calculated Young's modulus of Nafion with ionic liquid with respect to solvent uptake. A simple fit shows the dominant $1/w$ relationship.

Figure 7.2 is a graph of the calculated Young's modulus for the samples versus total solvent uptake, $w = w^{IL} + w^w$. The graph shows a neat $1/w$ trend; the fit of $Y = c_1/w + c_2$ gives $c_1 = 22.7$ and $c_2 = 4.18$ with a correlation coefficient of 0.995.

7.2 Model Application to Experimental Data

To apply the model outlined in Section 6.3 to the experimental data from Section 7.1, the parameters $\bar{\alpha}_1$ and $\bar{\alpha}_2$ are fit to the data using a least-squares routine. Other parameters are listed in Table 7.1. The fitting procedure gives $\bar{\alpha}_1 = 1.80$ and $\bar{\alpha}_2 = -0.063$, and the results are shown in Figure 7.3. The model shows an excellent fit to the data and captures the overall $1/w$ trend.

Parameter & Value	Definition
$\rho_B = 2.0$ g/cm^3	Dry density of Nafion
$\rho_{IL} = 1.39$ g/cm^3	Density of EMI-Tf
$\rho_w = 1.0$ g/cm^3	Density of water
$M_{IL} = 260.23$ g/mol	Molecular weight of EMI-Tf
$M_w = 18$ g/mol	Molecular weight of water
$EW = 1100$ g	Equivalent weight of Nafion 117
$\epsilon_1 = 15.1\epsilon_0$	Permittivity of EMI-Tf [57]
$\epsilon_2 = 7.5\epsilon_0$	Permittivity of water in the hydration shell of a Li$^+$ ion [56]
$\epsilon_0 = 8.85 \times 10^{-12}$ F/m	Permittivity of free space
$n_0 = 0.01$	Estimated initial porosity [12]

Table 7.1: Values for the parameters used in the stiffness model.
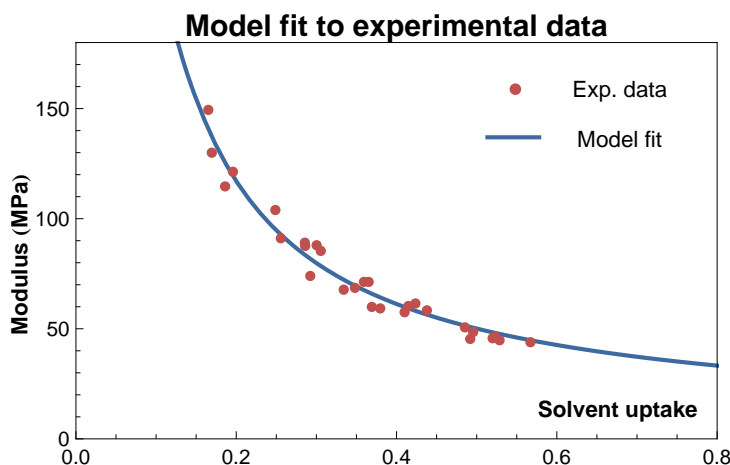
Figure 7.3: Experimental data with the micromechanical model applied and the parameters $\bar{\alpha}_1$ and $\bar{\alpha}_2$ fitted. The fit has a correlation coefficient of $R^2 = 0.996$.

Chapter 8

Results - Actuation Modeling

8.1   Model Application to an Ionic Liquid IPT

To apply the model outlined in the previous chapters to the actuation of an ionic liquid IPT with EMI-Tf ionic liquid as solvent, there are several parameters which are unknown and must be estimated. The hydrated thicknesses of the IPT and Nafion layer are given the values $2H = 200$ μm and $2h = 186$ μm, respectively. The average permittivity and thus the length scale for the charge transport problem is defined by modeling the system as a parallel plate capacitor,

$$\bar{\epsilon} = 2h\varsigma \tag{8.1}$$

where the capacitance per surface area is defined using an approximate measurement of $\varsigma = 0.05$ mF/cm^2 [1]. The radius of the cluster is assumed to vary as $a = 1.6 \, (w/\bar{w})^{1/3}$ nm, and the initial uniform solvent uptake is taken to be $\bar{w} = 0.5$. Since the diffusion coefficient of Li$^+$ in Nafion with ionic liquid is unknown, the charging time scale was estimated to be $\tau_C = 0.25$ s.

The modulus of Nafion with respect to solvent uptake was measured in Chapter 7; here, an empirical fit of the form

$$Y_B = \frac{c_1}{w} + c_2 \tag{8.2}$$

is used to represent the data. The calculated local solvent uptake in the CBL is several times higher than what is measured experimentally, and the micromechanical stiffness model outlined in Section 6.3 and applied to the data in Section 7.2 is not directly applicable at

Parameter	Value
$2H$	200 μm
$2h$	186 μm
ς	0.05 mF/cm^2
$\bar{w}$	0.5
c_1	22.7 MPa
c_2	4.18 MPa
τ_C	0.25 s
L	18 mm
Y_M	75 GPa
A_B	0.5
V_0	1 V
V_s	187.2 cm^3/mol

Table 8.1: Values for the parameters used in the actuation model.

these values. Thus, the empirical fit of Eq. 8.2 is used, which has the simple asymptotic behavior of $Y_B \to c_2$ as $w \to \infty$. The fit of Eq. 8.2 to the experimental results is shown in Figure 7.2 with the parameter values $c_1 = 22.7$ and $c_2 = 4.18$.

The modulus of the IPT is calculated from that of the bare polymer using the model in Ref. [12]. First, the average strain in the IPT is expressed as a sum of the average strain in the polymer and metal layers times the volume fraction of each layer. The average stress in the IPT is expressed the same way, and it is also assumed that the average stresses in the polymer and metal layers are related to the stress in the IPT by constants, referred to as concentration factors. The average stresses and strains in the polymer and metal layers and in the IPT are related using Hooke's law, and the resulting expression is simplified and rearranged to obtain

$$Y_{IPT} = \frac{Y_M Y_B(\bar{w})}{B A_B Y_M + (1 - B A_B) Y_B(\bar{w})} \qquad B = \frac{1 + w - f_M}{1 + w} \qquad (8.3)$$

where Y_M is the modulus of the metal, f_M is the volume fraction of metal plating in the dry sample, and A_B is a stress concentration factor for the average stress in the bare polymer. The values used for these coefficients are tabulated in Table 8.1 along with values for the other parameters which were used in the model.

The hydraulic permeability, K_s, and the effective dipole length, α, still remain to be estimated. Since the values of these parameters can have a large effect on the model predictions,

a parameter study was conducted in order to determine possible values that correlate with experimental trends. Since ion transport happens on a much faster time scale than solvent migration, varying K_s in the model will only affect the speed at which actuation occurs - the qualitative behavior will stay the same. This suggests a natural time scale for solvent migration,

$$\tau_s = \frac{\lambda h}{K_s P_R} \tag{8.4}$$

which is defined similarly to τ_C in Eq. 5.11. Note that τ_s depends implicitly on α, since $P_R = P_R(\alpha)$.

Now, using the linearized expressions from Section 5.1, Eq. 5.6 can be evaluated to determine solvent uptakes in the boundary layers and Eq. 5.7 can be numerically integrated to determine tip displacement. The results for boundary layer solvent uptakes and tip displacement when α is varied are shown in Figure 8.1. The applied voltage is $V_0 = 1V$ in these calculations. Since the solvent uptakes in the polymer are always above the critical uptake, α is taken be constant, not a function of solvent uptake as in Section 6.3.

Due to the large number of cations which move into the cathode boundary layer (CBL) when a voltage is applied, the charge density Q in this layer will be exponentially increasing. In the linearized formulation, the uniform charge density in the CBL is $Q = L_A/L_C$, which is > 1. This causes large electrostatic pressures to develop in the CBL (which vary with Q^2), and therefore a large amount of solvent will move into the CBL as the system moves towards equilibrium. The charge density in the anode boundary layer (ABL) is constant ($Q = -1$) due to the fixed anions on the polymer side-chains. Whether solvent uptake in the ABL will increase or decrease as the system moves toward equilibrium depends on P_R. When α is small, electrostatic interactions in the ABL will lead to $P_{ABL} > P_R$, so solvent will move into the ABL as the system moves towards equilibrium. When α increases, P_R increases but P_{ABL} stays the same, so eventually $P_{ABL} < P_R$ and solvent will move out of the ABL as shown in Figure 8.1(a). In the CBL, P_{CBL} will increase more quickly than P_R when α is increased due to the Q^2 dependence. However, Figure 8.1(b) shows that uptake in the CBL actually decreases for larger values of α. This is because the solvent uptake depends on the integral of the pressure difference with respect to time (Eq. 5.6), not the peak difference. When α increases, the pressure difference $P_{CBL} - P_R$ will initially increase, but numerical results show that it also will drop to zero more quickly, i.e. its integral will decrease. Therefore, the solvent uptake in the CBL will decrease when α is increased even though the initial pressure gradient is larger.
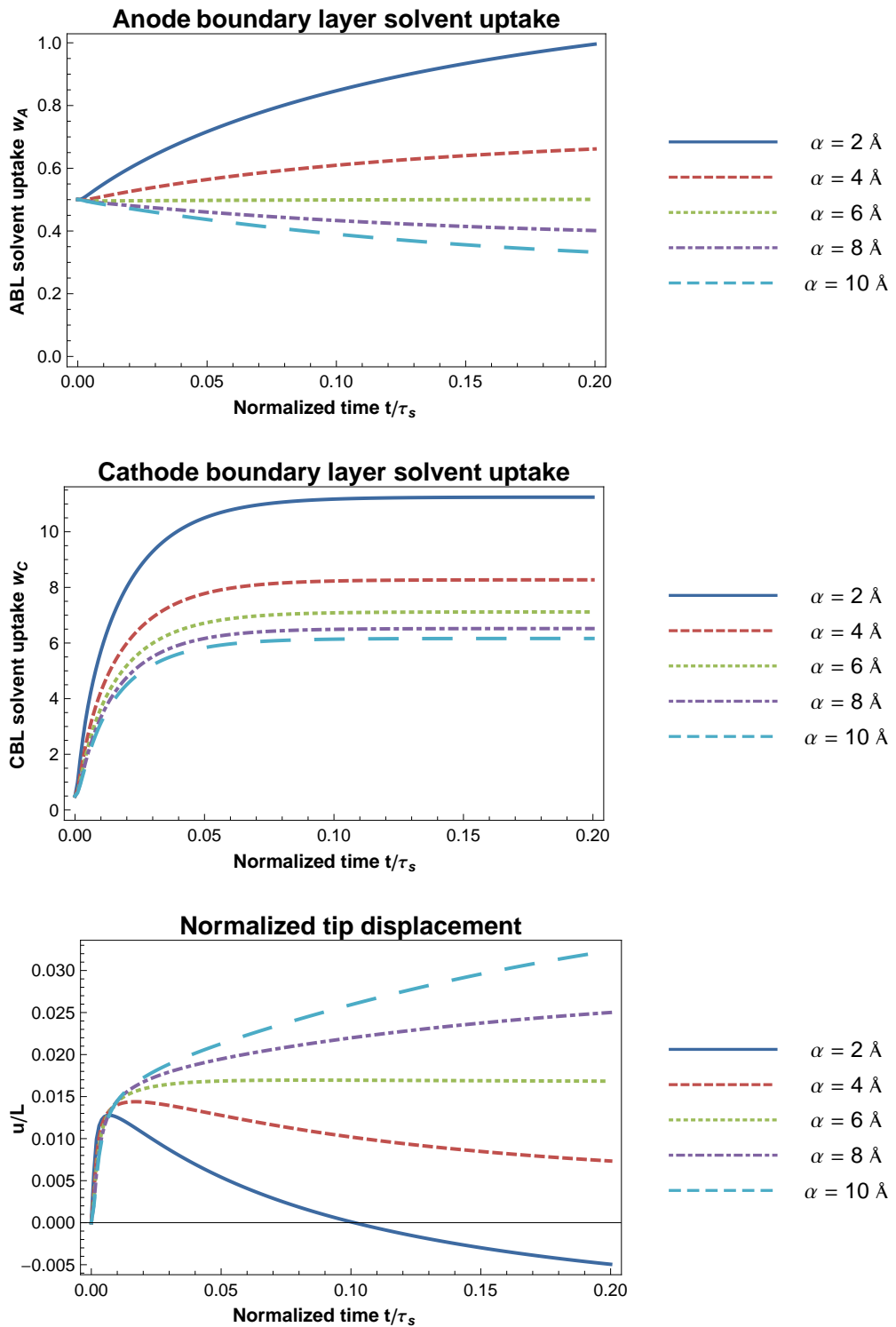
Figure 8.1: Results showing model calculations for anode and cathode boundary layer solvent uptakes and tip displacement when the effective dipole length α is varied.

Since backrelaxation has not been observed for ionic liquid IPTs, a value of $\alpha = 6$ Å may be chosen from Figure 8.1(c) to correlate with experimental results. For different values of α, it is seen that the magnitude of the initial response stays nearly constant but the extent of the backrelaxation changes. This is explained by looking at the solvent uptakes in the ABL and CBL. When α is large, the uptake in the ABL decreases from its initial value so the generated bending moments in both boundary layers will have the same sign and any relaxation will be in the same direction as the initial actuation movement. When α decreases, the solvent uptake in the ABL will now increase, creating a bending moment with an opposite sign of that generated by the CBL. The ABL is larger than the CBL, so solvent movement into the ABL takes longer. This is why the initial magnitude of the response is similar, but the model predictions at long times are different for the different cases. However, the linearization used in Eq. 5.6 amplifies this effect and makes solvent movement into the ABL appear quite slow. Due to the approximations used in generating these solutions, care should be taken when drawing conclusions from the results. A simple explanation could say that the extent of backrelaxation varies inversely with P_R, which is representative of the equilibrium electrostatic interactions, and determines the calculated uptake in the ABL in the model. Since Eq. 4.13 is an approximate expression, α can be taken to be a representation of these equilibrium electrostatic interactions rather than an actual physical length between an anion and a cation. In the model, an ionic liquid IPT can be given a higher value of α than a water-based IPT, where backrelaxation is observed. However, the actual results involve many coupled phenomena and this description is somewhat of an over-simplification of the system, especially since the governing equations were linearized before solving. Because of this, the model is expected to be most accurate at short times, where it is seen that results do not depend as strongly on α but more on charge transfer and the resulting cluster pressures. In this way, the linearized model can be used to identify parameters which maximize the initial actuation response. In regards to the response at longer times for water-based IPTs, a large amount of the observed backrelaxation may be due to oxidation/reduction reactions occurring at the electrodes [84] when $V_0 > 1.2$ V, an effect which is not considered here. The actuation of an IPT is quite complex and involves numerous phenomena which have been omitted here, including the results for charge transport of multiple mobile ionic species in ionic liquid IPTs which are presented in Chapter 9. From this analysis it is mainly seen that the actuation of IPT involves many complex nonlinear phenomena, with electrostatic interactions being dominant. It is also shown that a physically-based model which includes the dominant actuation mechanisms can be used to fit experimental trends and gain insight

Middle layer solvent uptake varying thickness
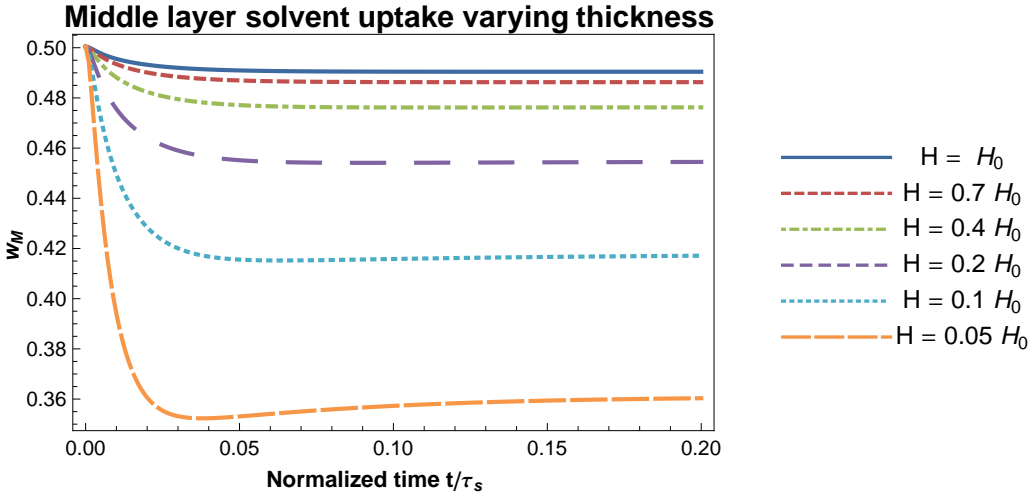
Figure 8.2: The calculated solvent uptake in the middle layer, w_M, when the membrane thickness is varied. $\alpha = 6$ Å and $H_0 = 100$ μm were used to correspond with results from Section 8.1, and h was assumed to vary with H.

into the complex processes at work during actuation.

8.2 Free Air Actuation Refinement

For an IPT made with Nafion 117, the dry thickness is 178 μm and the change supplied by the free air actuation refinement described in Section 5.2 is small due to the small relative sizes of the boundary layers versus the inactive middle layer. However, when a much thinner polymer membrane is used, enforcing conservation of mass of the solvent will cause a noticeable change in w_M, as shown in Figure 8.2, and the model predictions for the actuation response will change. Since the model results are dependent on several different parameters and α is fit to experimental data, it is more relevant to compare the change in w_M, not a change in the predicted tip displacement calculations, when the free air actuation refinement is applied. In Figure 8.2, the time scale τ_s for different membrane thicknesses is held constant since the linearization causes the calculated temporal response to be independent of h, as seen in Eq. 5.6. In a numerical implementation, it is expected that the time scale for solvent transport would vary linearly with membrane thickness. From Figure 8.2, it is seen that the refinement accounted for with Eq. 5.13 will only play a significant role in model predictions when the membrane becomes very thin. However, new ionic liquid IPT actuators are currently being made with much thinner membranes, such as those discussed in Ref. [85] which use Nafion
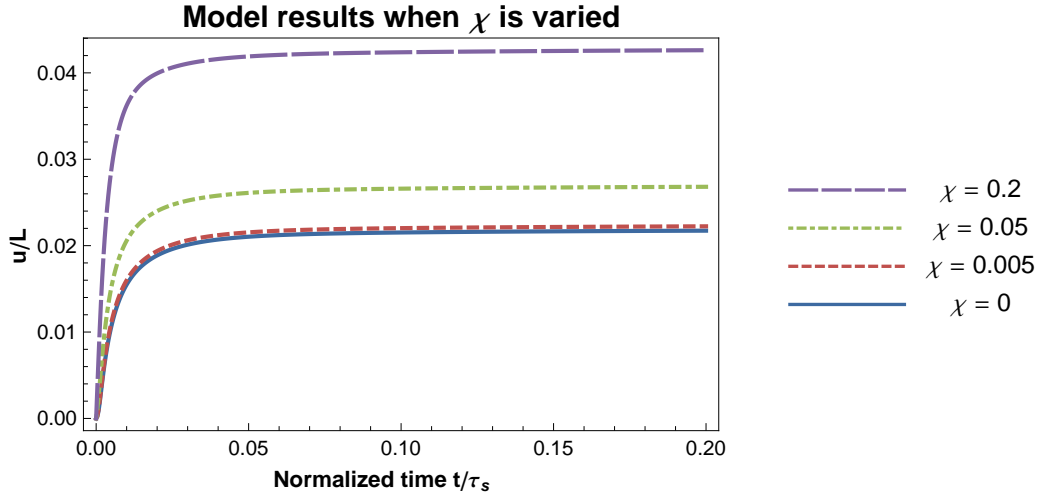
Figure 8.3: Comparison of model results for tip displacement for different values of χ

membranes only 25 μm thick. For these, the refinement outlined in this section will have a significant impact on the model predictions. For thicker membranes, the approximation $w_M \approx \bar{w}$ is typically sufficient.

8.3 Cation Dependent Volumetric Eigenstrains

Figure 8.3 shows a comparison of actuation predictions when the ion size parameter χ is varied. Since the diffusion coefficient of the ion and the equilibrium charge density were assumed to stay the same for the different size ions, Figure 8.3 is simply a parameter variation and does not accurately represent IPT actuators in the different ion forms. For large ions, the equilibrium charge density will change, as discussed in Section 3.3. The temporal response will also be different, because the larger ions will tend to move more slowly than the small ones. The effective dipole length was set as $\alpha = 6$ Å for these calculations.

From Figure 8.3 it is seen that large cations will play a considerable role in creating the volumetric expansion of the boundary layers which causes actuation. For an ionic liquid IPT where there are multiple mobile ionic species, this means that the volumes of the charged ionic liquid ions moving under the influence of the applied electric field along with those moving together as neutral cation-anion pairs need to be considered in a full description of actuation. This phenomenon is unique to ionic liquid IPTs, and recent experimental results have tested the effects of using ionic liquids with different sized ions [86]. Although not done

here, the modeling framework outlined in the previous chapters could be extended to model the experimental results in Ref. [86] through the inclusion of multiple mobile ionic species migration and the finite size of the ions of the ionic liquid. This sort of an extension to the model may be a topic of future research.

Chapter 9

Numerical Simulations of Charge Transfer

9.1 Water-Based IPTs: Single Mobile Ionic Species

To solve Eqs. 3.12-3.14 as outlined in Section 3.2, an efficient finite difference method was implemented [13, 87]. The evolution of cation concentration in the boundary layers when 1 V is applied is shown in Figure 9.1. To display the results, time is normalized according to the time scale $\tau_C = \lambda h/D$ and position is normalized with respect to the thickness of the membrane, $2h$. The last time step, $t = 3$, corresponds to an equilibrium configuration (t refers to non-dimensional time, i.e. $t = t_{dim}/\tau_C$). For comparison of results with Ref. [12], the Debye length is defined to be $\lambda = .779$ μm, and the thickness of the membrane is taken to be $2h = 212$ μm.

The time scale for the problem is often stated to be the Debye time, $\tau = \lambda^2/D$. However, Bazant et al. [88] state that the correct time scale for the problem is $\tau_C = \lambda h/D$ and show that this time scale arises from a matched asymptotic expansion of the Nernst-Planck/Poisson equations considering thin boundary layers. To analyze this result as applied to IPT actuation, numerical simulations were performed to determine the effect of actuator thickness on time to form boundary layers. The parameters used are the same as those used for Figure 9.1, and the numerical results are shown in Figure 9.2. The normalized charge transferred at a given time is calculated by integrating the charge density over one half of the polymer

Ion concentrations with 1 mobile ionic species
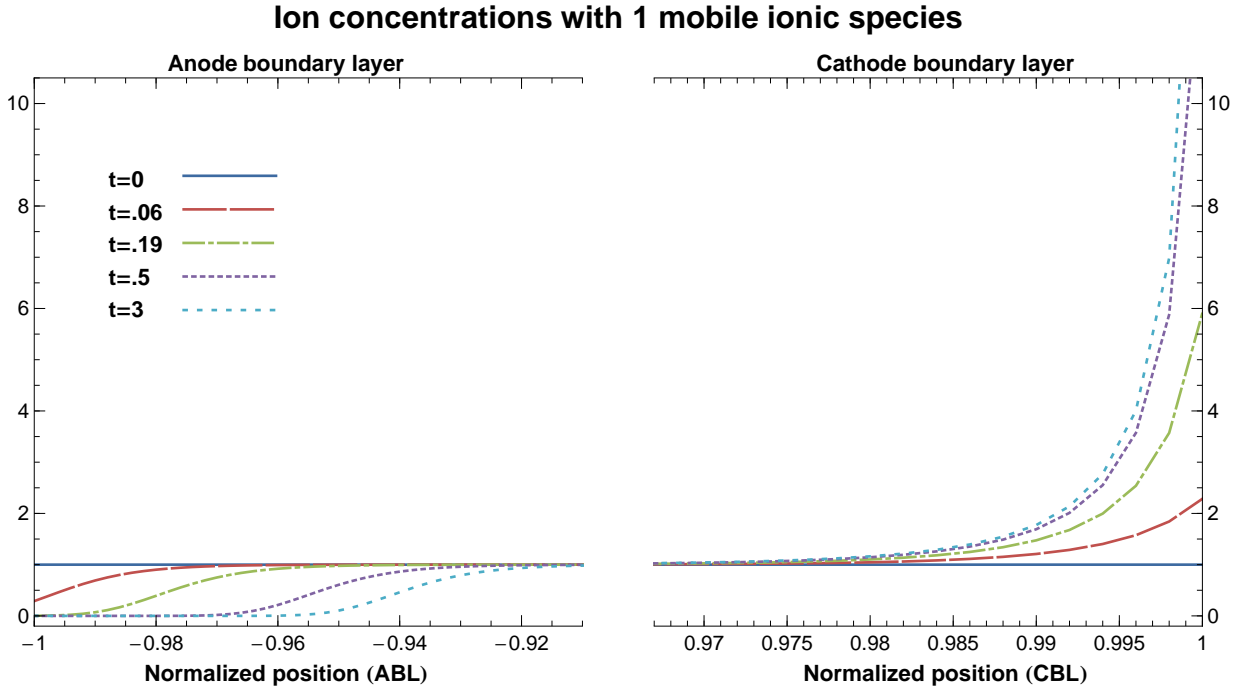
Figure 9.1: Transient numerical solution of the NPP equations showing cation concentration in response to an applied voltage of 1V

and dividing by $F\lambda c_0$. The time to form boundary layers is defined as the time needed to reach 90% of the total charge transferred. For actuators with different thicknesses, the total amount of charge transferred at equilibrium is independent of actuator thickness when the same voltage is applied. This behavior is expected because the sizes of the boundary layers are defined by the Debye length using NPP theory and do not depend on the thickness of the actuator. The sizes of the boundary layers vary with solvent uptake, electrode structure, applied voltage, and ion exchange capacity of the ionomer. Only at high applied potentials where steric effects from the mobile ions become important will the boundary layer size vary with applied potential. Also, it is seen that the time to reach a certain amount of charge transferred, and thus the time needed for actuation to occur, varies linearly with thickness. The results in Figure 9.2(b) agree with the results of Bazant et al. [88] that the time scale for the problem is $\tau_C = \lambda h/D$, not $\tau = \lambda^2/D$.

Physically, this result is intuitive since ion flux is driven by the electric field, not the absolute value of the electric potential. The electric field is the change in electric potential with respect to a change in position, which here only refers to the x direction. When a voltage is first applied to the system (at $t = 0$), the potential in the membrane is initially a linear function

Charge transferred vs. time

Normalized charge transferred

Thinner actuator

Normalized time

Time to form boundary layers vs. thickness

Time to form boundary layers

● Numerical simulations

— Linear regression

Membrane thickness (μm)
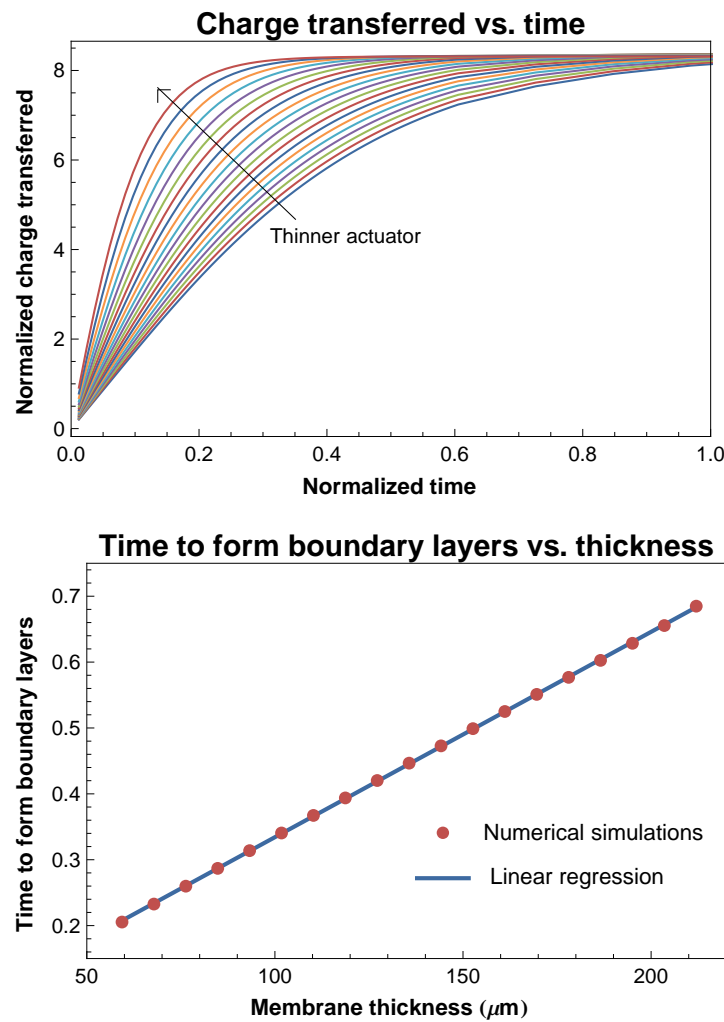
Figure 9.2: The effect of actuator thickness on boundary layer charge dynamics. (a) Charge transferred vs. time for actuators with different thicknesses. (b) Time to form boundary layers versus actuator thickness

of x. This means that the electric field is initially constant and equal to $V_0/2h$. So, at $t = 0$, the electric field varies inversely with thickness. From the Nernst-Planck equation (Eq. 3.12), the electric field is the driving force for migrative ion flux, so it follows that the time to form boundary layers varies linearly with membrane thickness. A more mathematically rigorous description of this time scale is given by Bazant [88].

9.2 Ionic Liquid IPTs: Multiple Mobile Ionic Species

9.2.1 Parameter Description

The system in consideration is an ionic liquid IPT with EMI-Tf ionic liquid as solvent and Li^+ as the neutralizing counter-cation. The ionomer membrane is Nafion 117, which has an equivalent weight of 1100g and is given a swollen thickness of 200 μm. The three mobile ionic species are Li^+, Tf^-, and EMI^+, and the anionic sulfonate groups of the Nafion membrane are considered fixed. The Debye length is effectively defined using a capacitance measurement of 0.05 mF/cm^2 for an ionic liquid IPT [1], which yields $\lambda = 0.152$ μm.

The concentration of the ionic liquid ions in the polymer is known simply from the uptake. However, unlike in a neat ionic liquid, all of the ions of the ionic liquid will not be available to separate and selectively move towards the electrodes. Due to interactions with the Nafion ionomer, some of the ionic liquid ion pairs will continue to exist as dipoles and quadrupoles even when a voltage is applied [47]. The amount of "free" ionic liquid ions is not known. Also, although the diffusion coefficients of EMI^+ and Tf^- in Nafion have recently been measured [55], the relative diffusion coefficient of Li^+ is not known. These parameters were varied in the numerical solutions in order to see the dynamic response of the system for the different cases. For simplicity, the diffusion coefficients of the ionic liquid ions were given equal values, denoted as

$$D_{IL} = \frac{D_{EMI^+}}{D_{Li^+}} = \frac{D_{Tf^-}}{D_{Li^+}} \tag{9.1}$$

The amount of "free" ionic liquid ions relative to Li^+ ions is defined as

$$F_{IL} = \frac{c_{EMI^+}^0}{c_{Li^+}^0} = \frac{c_{Tf^-}^0}{c_{Li^+}^0} \tag{9.2}$$

In the following, the parameters sets of $(D_{IL}, F_{IL}) = (1, 0.5)$, $(0.1, 0.5)$, and $(0.1, 0.1)$ are

shown.

9.2.2 Illustrative Example at Low Applied Voltage

The finite element model outlined in Section 3.4 was implemented in Mathematica using the parameter sets outlined in the previous section. To analyze the response, a test case with an applied voltage of $V_0 = 0.25$ V is considered. This is low compared to typical IPT operating voltages, but since it is known that the assumptions in the underlying theory do not hold when steric interactions between the ions become important, the results for higher applied potentials with classic NPP theory should not be used. Nonetheless, a test case with a relatively low voltage can give insight into the mechanisms of ion transport, and this approach is taken here.

Figures 9.3, 9.4, and 9.5 show the evolution of the boundary layers when the step voltage V_0 is applied at $t = 0$. In these test cases, two time scales emerge - a charging time scale dependent on the Debye length, $\tau_C = \lambda h / D$, and another diffusive time scale dependent only on the size of the system, $\tau_D = h^2/D$. These time scales come from an asymptotic expansion of the NPP equations considering thin boundary layers, as shown in Ref. [88]. This effect can be explained phenomenologically by considering the driving forces of flux as shown by the Nernst-Planck equation. In Eq. 3.20, the first term on the RHS is flux from diffusion, and the second term is flux due to migration. The diffusive flux varies with the concentration gradient, and the migrative flux depends on the electric field. When the potential is first applied, the electric field is constant through the thickness, i.e. there is a linear variation in potential. As shown in Figure 9.6, the potential distribution quickly shifts as the ions move towards the electrodes, leaving a near zero electric field in all but the regions nearest the electrode (the boundary layers). In the bulk region outside the boundary layers, the flux will now be primarily diffusive, and for $\phi_{,x} \to 0$, combining Eqs. 3.20 and 3.21 gives Fick's 2nd law of diffusion. Now, ion movement in this layer will occur on the diffusive time scale τ_D. Due to the large amount of ions moving into/out of the boundary layers, there will be an initial excess or depletion just outside the boundary layers. Since the electric field has already been screened by the ions in the boundary layers, now only diffusive flux will occur in this area directly outside the boundary layers. For three mobile species with different diffusion coefficients the asymmetry of the problem is not conducive to a simple interpretation of the behavior, but the general presence of two time scales and a non-monotonic concentration

profile for each ion is similar to the simpler case of a binary electrolyte.

For the test cases shown in Figures 9.3, 9.4, and 9.5, each shows the same basic ion movement in the formation of the boundary layers, but the dynamic response is seen to be different for each case. In Figures 9.3 and 9.4 where $F_{IL} = 0.5$ (F_{IL} is the fraction of "free" ionic liquid ions relative to Li$^+$ ions) the equilibrium response as $t \to \infty$ is identical. For all the cases the time needed to reach equilibrium is much longer than when only a single mobile ionic species is considered due to presence of the second time scale τ_D discussed above. This is true even when the diffusion coefficients of all the ions are equal in Figure 9.3. In Figures 9.4 and 9.5 where $D_{IL} = 0.1$, even longer times are needed to reach equilibrium since the diffusion coefficients of the ionic liquid ions are set to $1/10$ that of the counter-cations. When $D_{IL} = 0.1$ the nonmonotic concentration profile is most visible, especially for the mobile anion Tf$^-$. However, as F_{IL} decreases, the overall charge transfer response depends more on the counter-cation and less on the ionic liquid ions, as shown in Figure 9.5. In this case, the most notable change in the response as compared to a water-based IPT is due to the presence of a mobile anion, which causes a region of increasingly negative charge density to form near the anode.

Figure 9.7 shows the evolution of charge density for the different cases. The charge density does not exhibit multiple time scales as the concentration profiles do, since the second time scale deals with bulk diffusion. Diffusive movement does not affect the charge density, since if $\phi_{,x} \ll 1$ is constant, then $\phi_{,xx} = 0$ and the charge density must be zero from Eq. 3.22.

The charge transferred and current with respect to time are shown in Figure 9.8 for the different test cases. The charge transferred is the integral of the charge of each ion times its concentration integrated over half of the system, i.e.

$$q = \int_0^{h^*} \sum_j z_j c_j(x) dx \tag{9.3}$$

and the current is the change in charge transferred with respect to time:

$$i = \frac{dq}{dt} \tag{9.4}$$

The charge transferred at a certain time step is calculated in a finite element framework by
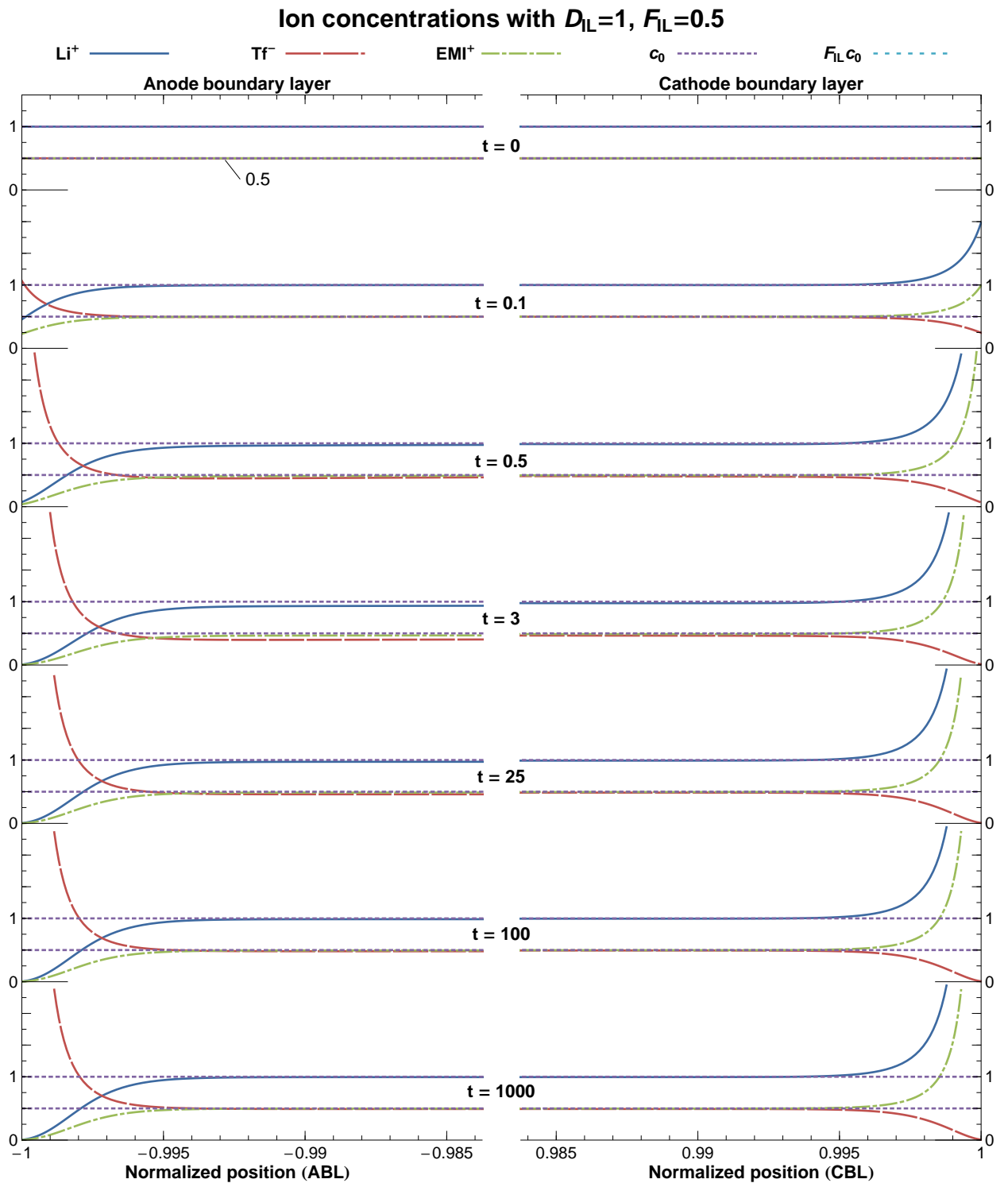
Figure 9.3: Concentration in the boundary layers with respect to time for $D_{IL} = 1$, $F_{IL} = 0.5$, and $V_0 = 0.25$ V. Later times are shown as data sets below the previous set, and the initial concentrations are shown as dotted lines for each ion.
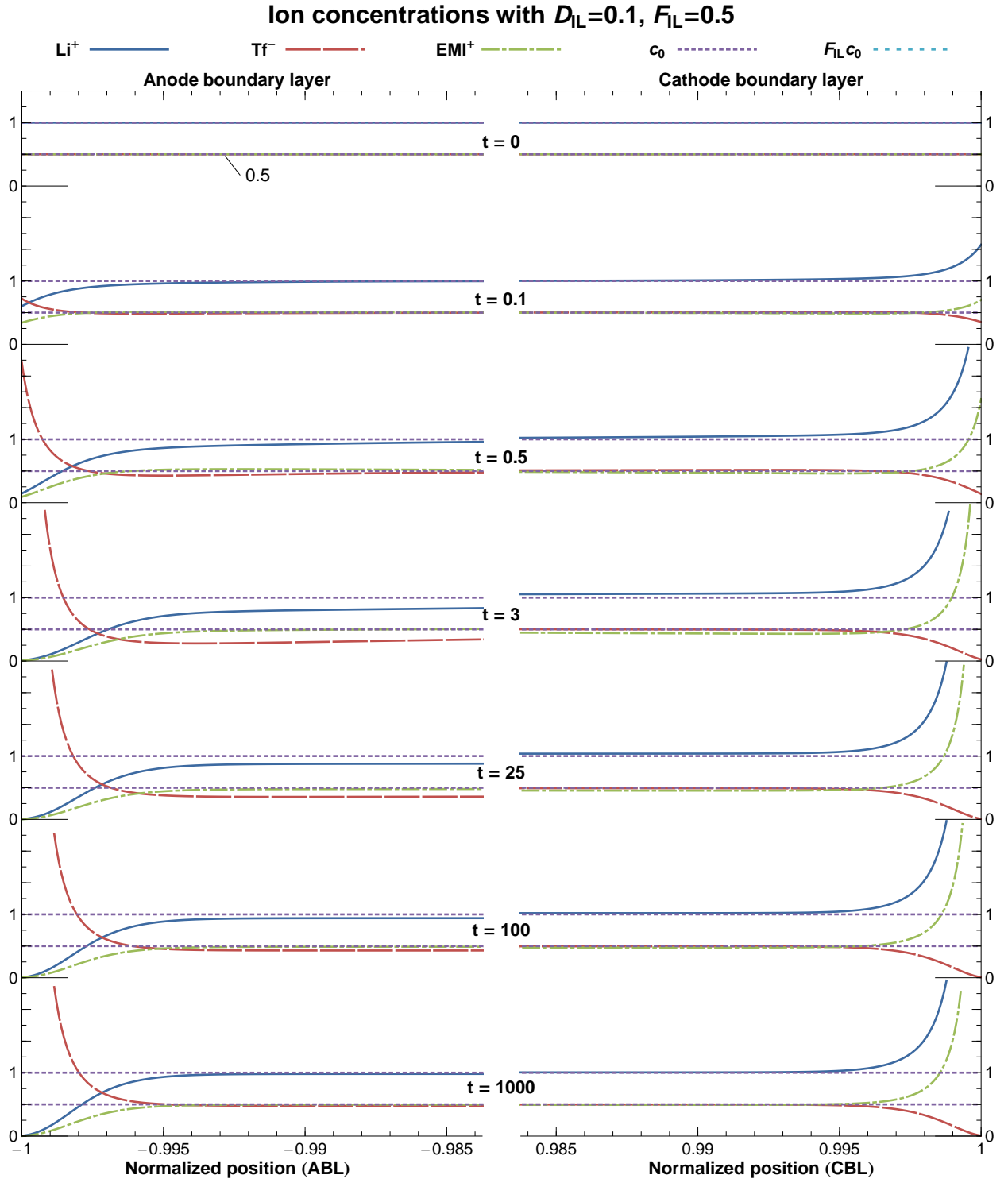
Figure 9.4: Concentration in the boundary layers with respect to time for $D_{IL} = 0.1$, $F_{IL} = 0.5$, and $V_0 = 0.25$ V. Later times are shown as data sets below the previous set, and the initial concentrations are shown as dotted lines for each ion.
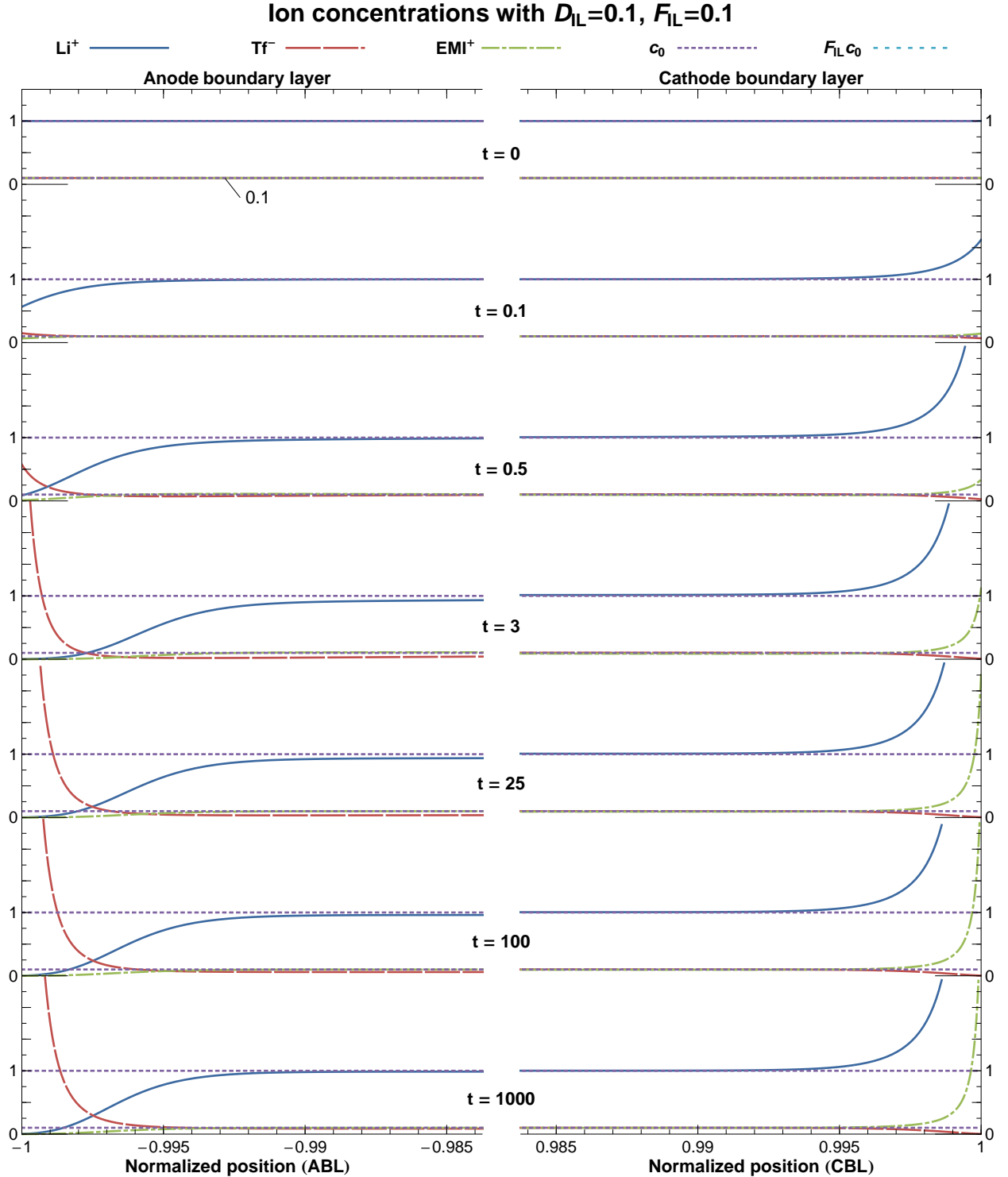
Figure 9.5: Concentration in the boundary layers with respect to time for $D_{IL} = 0.1$, $F_{IL} = 0.1$, and $V_0 = 0.25$ V. Later times are shown as data sets below the previous set, and the initial concentrations are shown as dotted lines for each ion.
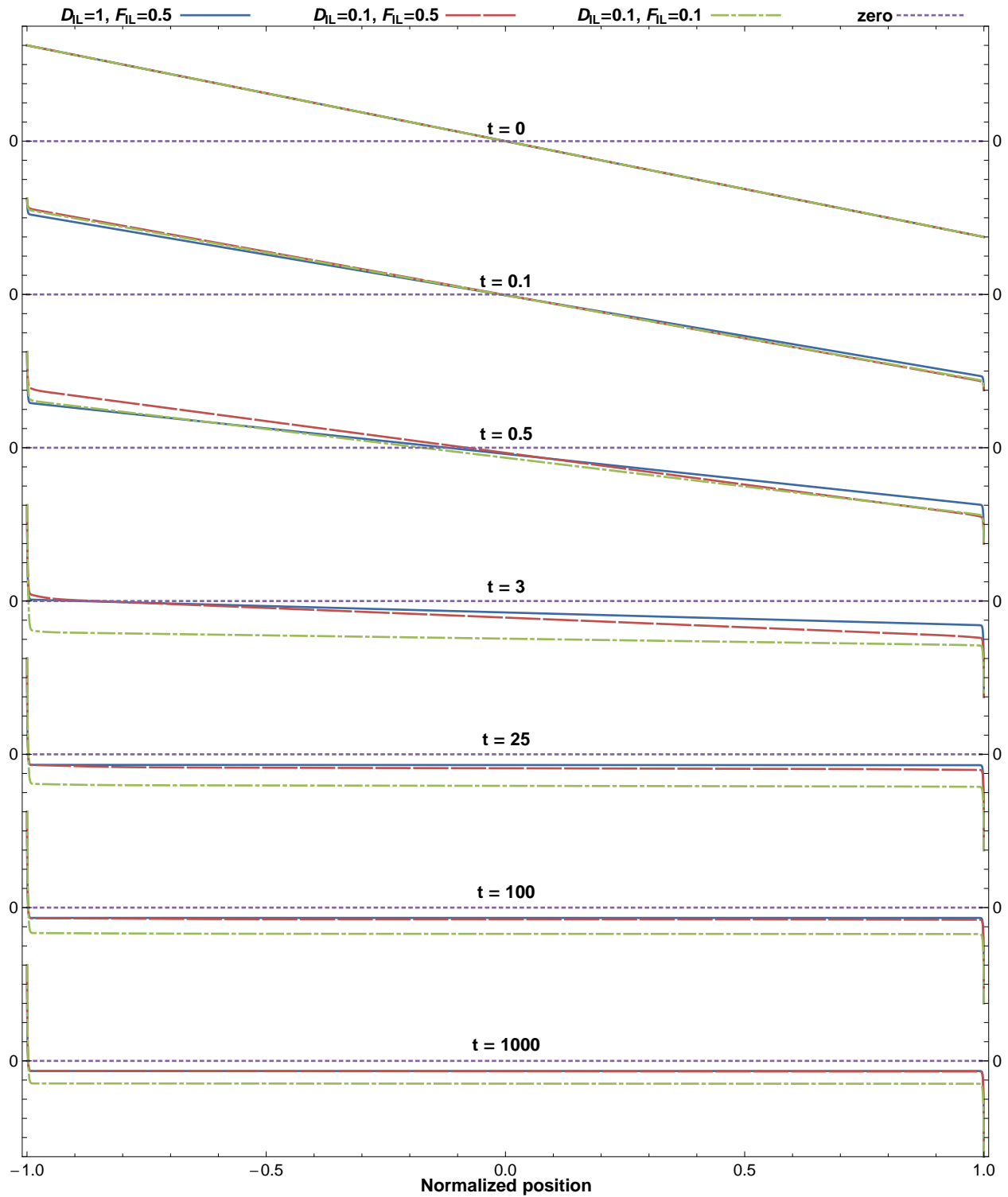
Figure 9.6: Evolution of the potential distribution in the membrane for the different cases.
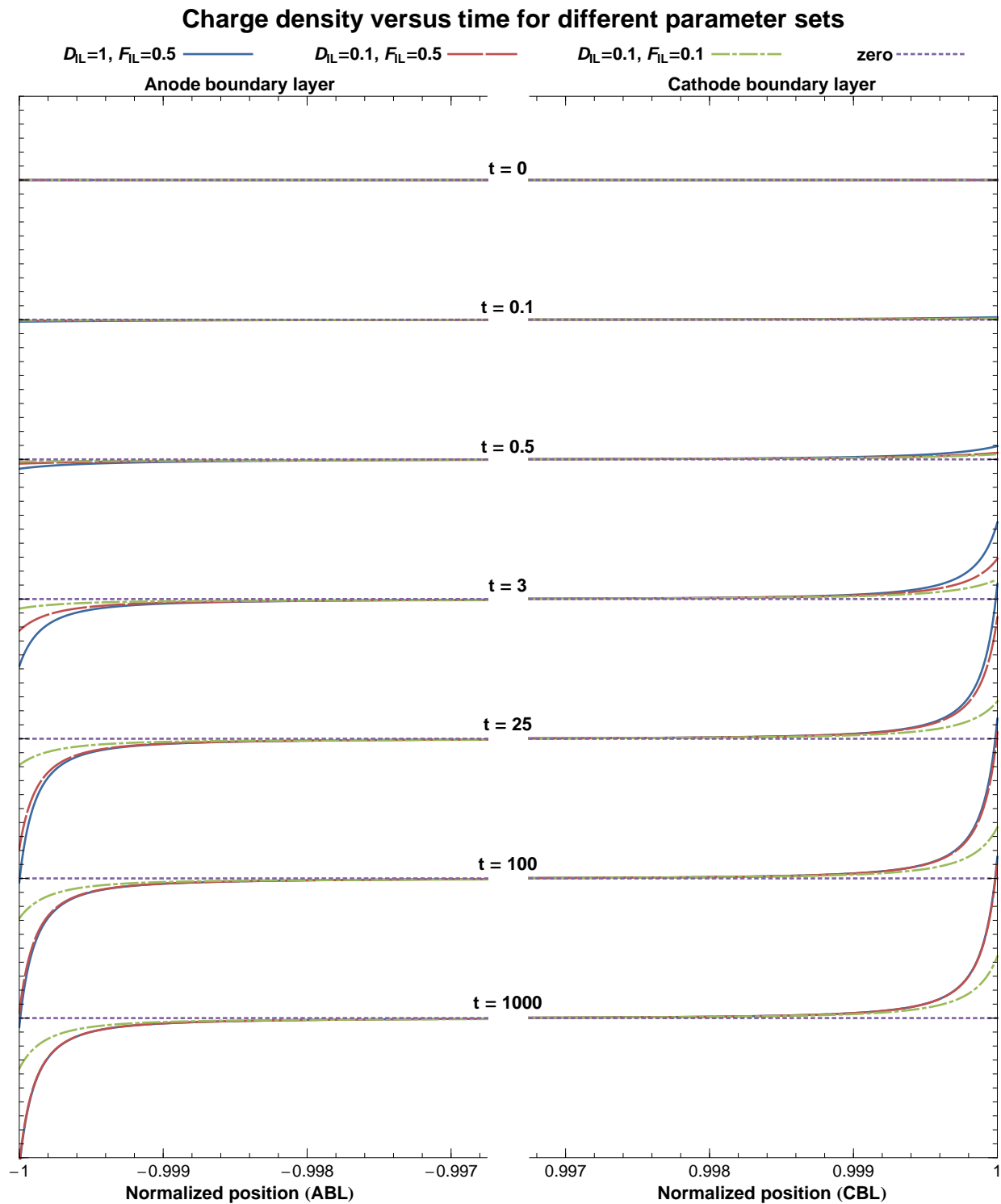
Figure 9.7: Evolution of the charge density distribution in the membrane for the different cases.
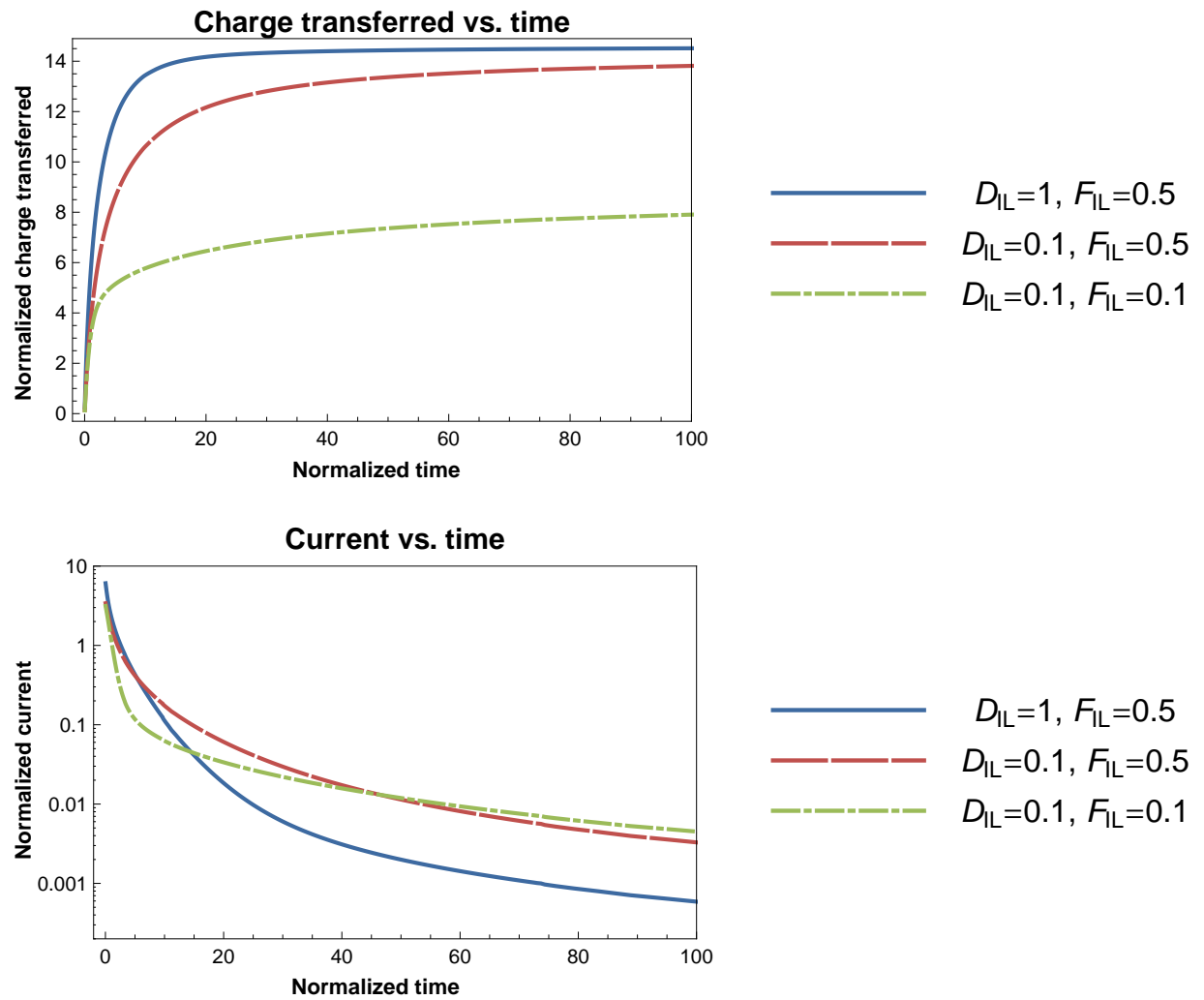
Figure 9.8: Charge transferred and current vs. time for the different test cases. (a) Normalized charge transferred is calculated as $q/(F\lambda c_0)$ (b) Normalized current is $ih/(FD_+c_0)$, where D_+ is the diffusion coefficient of Li^+.

defining an integral operator,

$$H_A = \int_0^h N_A dx \tag{9.5}$$

so that Eq. 9.3 is evaluated using

$$q_n = \sum_j H_A z_j c_A^j(t_n) \tag{9.6}$$

where q_n refers to the charge transferred at time step n. To calculate the current, first define the matrices

$$M_{AB}^t = \int_0^t L_A L_B dt \tag{9.7}$$

$$K_{AB}^t = \int_0^t L_A \frac{dL_B}{dt} dt \tag{9.8}$$

where L_A are the Lagrange interpolation functions and the interpolation is done over time, not space. Now, the current for each time step is calculated with

$$i = \left(M^t\right)^{-1} K^t q \tag{9.9}$$

These calculations only depend on the charge density since they are a sum over the different ionic species, and therefore there is only one dominant time scale in the response. When $D_{IL} = 1$, charge is transferred quickly, so the current also decays quickly. For the cases where $D_{IL} = 0.1$, the charging time is slowed by the slower moving ionic liquid ions, and therefore the current takes longer to decay to zero. However, for the case with $D_{IL} = 0.1$ and $F_{IL} = 0.1$, Figure 9.8(b) shows that the current initially decays faster than when $D_{IL} = 1$ and $F_{IL} = 0.5$. This seems contradictory at first, since the ionic liquid ions are now prescribed to move more slowly, but the response can be explained as follows. When there is only a single mobile ionic species, the NPP equations predict a maximum in capacitance near zero applied voltage [6], compared to a binary electrolyte solution which displays a minimum in capacitance at this point. This suggests that the presence of a mobile anion will tend to increase the capacitance of the system, and increase the overall amount of charge transferred as shown in Figure 9.8(a). Specifically, more cations will now move into the cathode boundary layer in addition to anions now moving into the anode boundary layer, even if only mobile anions (not anions and cations) are added to the system, and thus the capacitance will

vary nonlinearly with the amount of mobile anions. Note that only adding mobile anions would mean removing fixed anionic groups due to conservation of charge. For the case with $D_{IL} = 0.1$ and $F_{IL} = 0.1$, there is only a small number of mobile anions and therefore there is a decrease in capacitance. This means that less charge will be transferred by the mobile counter-cation Li^+, and therefore this charge transfer will finish more quickly. After the quick movement of Li^+ ions, there are still slow-moving ionic liquid ions in the system which now cause the current to decay very slowly. At long times, the numerically calculated current values are several orders of magnitude below the initial response and can be practically taken to be zero. The current response at long times is also not a quantity of interest to be obtained from the numerical solution in this case, since the long term behavior as $t \rightarrow \infty$ is always known: current decays to zero. The initial current response, on the other hand, is a very important quantity to calculate accurately since it is the quantity most easily measured by experiment.

Chapter 10

Discussion

10.1 Modulus of Nafion With Respect to Ionic Liquid Uptake

In Chapter 7 experimental stress-stretch data was taken in order to measure the modulus of Nafion swollen with ionic liquid with respect to solvent uptake, and a micromechanical model for the modulus of the swollen ionomer developed by Nemat-Nasser [12] was modified using the results of Chapter 4 and applied to the data. The results demonstrate that the dominant relationship is between modulus and volume fraction of solvent, and the results are only weakly dependent on the nature of the solvent. This sort of a conclusion cannot be made in a broad sense, however. Recall that the ionic liquid was incorporated into the samples at room temperature. This leads to essentially no change in the microstructure of the ionomer when ionic liquid is added, and thus it is reasonable to expect similar behavior as seen with other solvents. To fabricate an IPT, maximum absorption of the ionic liquid is achieved by placing the membrane in an ionic liquid bath and heating to $\sim$ 105 °C. Higher heating temperatures have also been used [40]. Nafion is known to have multiple glass transition temperatures (T_g's), including transitions corresponding to the ionic domains (denoted as the α transition in the literature) and the polymer matrix (β transition). The former occurs at a higher temperature, and has been found to vary significantly for Nafion in different ionic forms [18, 70]. For Nafion in Na$^+$ form, the β transition is at $\sim$ 150 °C and the α transition is at $\sim$ 240 °C. For Nafion in Li$^+$ form, similar transition temperatures can be

expected [70]. Above T_g, the polymer chains can move locally and re-orient themselves. So, if a Nafion membrane is heated to near or above either the α or β transition temperatures, the polymer chains will be able to re-orient themselves into a configuration that minimizes free energy. In the presence of an ionic liquid, this re-orientation may give rise to a slightly different microstructure, which in turn will affect the mechanical and transport properties. In this study, this effect was not considered since the ionic liquid was incorporated at room temperature. Future work may include investigations of microstructural changes and their resulting effect on membrane properties when an ionic liquid is incorporated near T_g.

The modulus of Nafion with respect to solvent content has been previously investigated by Nemat-Nasser [12, 13], where water, glycerol, and polyethylene glycol were used as solvents. In order to make a direct comparison of results, the preparation steps need to be the same; otherwise, uncontrolled effects will dominate. Ideally, the Nafion samples should also come from the same batch. When these steps are not followed, only a qualitative comparison should be made. The $1/w$ trend that was found here agrees with Refs. [12, 13]; however, the magnitude of the modulus is low for the present results. To experimentally investigate the difference in modulus between Nafion with ionic liquid versus Nafion with water, all tests would need to follow identical protocols. However, from the trend demonstrated in the results and the discussion points mentioned above, it is expected that the dominant trend is with solvent uptake and any dependence of the modulus on the characteristics of the solvent will be small for solvents typically considered for use with IPTs. If the preparation is changed so that the solvent is incorporated at temperatures near T_g, then different results could be expected.

10.2   Charge Transfer

The solutions of the Nernst-Planck/Poisson equations with 3 mobile species show distinct differences compared to that of a single mobile ionic species in a water-based IPT. When there is a mobile anion, the anode boundary layer will have an increasingly negative charge density, compared to a water-based IPT where the ABL has a constant charge density due to the fixed anionic groups on the ionomer backbone. When there are multiple mobile ionic species, the concentration of each ion exhibits a non-monotonic charging profile across the thickness of the membrane, and the dynamic response shows the presence of two distinct time scales. The introduction of an ionic liquid will also tend to increase the capacitance

of the device at low applied potentials, since the increased amount of mobile ions results in a greater amount of charge transferred. However, to make conclusions for the general case, the modified theory in Eq. 3.19 needs to be used. The applicability of classic NPP theory in describing ion transport in ionic liquids is limited due to the large sizes of the ionic liquid ions. The test case shown here with an applied voltage of 0.25 V may even be out of range of what NPP theory can accurately describe with respect to ionic liquids in IPTs. Further analysis is needed in order to make a firm conclusion in this respect. The correction for the finite size of the ions shown in Eq. 3.19 will have several notable effects on the predictions for ion transport. Using Eq. 3.7, the boundary layer size is characterized by the Debye length and is constant for different applied voltages. When imposing a maximum concentration, the boundary layer size will now become a function of the applied voltage, increasing for larger applied potentials. Imposing a finite maximum concentration for the ionic liquid ions also will change the capacitance/voltage relationship of the transducer. Since IPTs with a single mobile ionic species are predicted to show a decrease in capacitance with applied voltage [6], and neat ionic liquids typically show a similar trend [48, 89], it can be reasonably expected that an ionic liquid IPT will show a steeper drop-off for its capacitance/voltage curve versus a water-based IPT. This relationship can be computed numerically using Eq. 3.19 for ionic liquid ion flux, and measured experimentally using ac voltammetry or a related technique. A comparison here could validate or refute the theory of ion transport in ionic liquid IPTs discussed here, and will be the subject of future research.

10.3 Effects of Multiple Mobile Ionic Species on Actuation

In the actuation model applied to an ionic liquid IPT in Chapter 8, it was still assumed that there is only one mobile ionic species in the device; the results from Chapter 9 were not incorporated. To account for the movement of the ions of the ionic liquid under the applied field, the volumetric eigenstrain in the boundary layers would need to include the finite size of the ionic liquid ions, as discussed in Sections 5.3 and 8.3. Assuming concentration profiles for each ion as shown in Section 9.2, this will have several notable effects on the actuation predictions. The first is that the anode boundary layer will have an increasingly negative charge density, which in turn has two main effects: the electrostatic pressure in the ABL will increase, causing more solvent to move into the ABL, and the large ionic liquid ions

will also cause expansion of the ABL. The CBL will still undergo the largest expansion since more ions move into this layer. The bending moment generated from ABL expansion will have a sign opposite of that generated by CBL expansion. However, because the ionic liquid also has a mobile cation, more cations are now moving into the CBL, and the volumes of the large ionic liquids cations also cause further expansion of the CBL. Therefore, it isn't clear whether or not the multiple mobile ionic species of the ionic liquid IPT will increase or decrease the actuation response, since the results are a balance of several different effects.

If the sizes of the ionic liquid ions are noticeably different, then the effect may be larger. There are quite a few different interactions which need to be considered for the case of different-sized ions, including the fraction of "free" ionic liquid ions, the equilibrium charge distribution considering the finite size of the ions, and the resulting cluster pressures and solvent transport. If the size of the anion of the ionic liquid is varied, as done in Ref. [86], and the fraction of "free" ionic liquid ions is taken to be the same for the different ionic liquids in the IPT, then the difference in response can be explained within the current model framework in terms of a balance between anion size effects and boundary layer pressures. As the size of the anion increases, the ABL will grow larger, since the maximum concentration of the anion will decrease. As the size of the ion decreases, the size of the ABL decreases, but now the electrostatic pressure (which varies with Q^2) will increase. Results for different sized anions will be a balance between these two effects. In Ref. [86], it was found experimentally that the IPTs with smaller ionic liquid anions had a better overall actuation response. If the fraction of free ions is the same, this suggests that ABL expansion due to large sizes of the ions is dominant over ABL expansion due to solvent influx from electrostatic pressures, and thus the larger ions tend to have a more negative effect on actuation. However, having a different fraction of "free" ionic liquid ions would alter this because the overall capacitance of the device would change, as was demonstrated in Section 9.2. Larger ions already decrease the capacitance, but a smaller amount of "free" ions further decreases the capacitance.

From this it is seen that simple conclusions cannot be made as to the effects of multiple mobile ionic species migration on IPT actuation performance. Further work needs to be done in model validation and other key parameters and relationships need to be measured experimentally, including the fraction of "free" ionic liquid ions and the capacitance/voltage relationship for IPTs with different ionic liquids. A full numerical solution instead of a linearization of the model outlined in the previous chapters would also give more information as to how the ionic liquid affects actuation performance.

10.4 Modeling Assumptions

Because of the complex nature of IPTs many simplifying assumptions are needed to model actuation; the possible effects of some of these assumptions are discussed here. One omission from the current model is the explicit effects of electrode structure. The Debye length was defined using an approximate bulk capacitance measurement in order to place model predictions for the total amount of charge transferred when a voltage is applied in line with experimental results. This does not give any information about the micro-mechanisms in the boundary layers, however. Because the electrodes are interpenetrating, using a definition of electrode performance based on the total surface area of the electrode, as done in Ref. [42], also does not capture all of the micro-mechanisms of actuation. The interpenetrating electrodes will cause highly variable local charge distributions, mechanical properties, and morphology, all of which will vary in three dimensions in the boundary layers. The exact nature of these changes is unknown, but in Section 8.1 it was shown that a homogenization approach can yield results which generally describe the macroscopic actuation response. Such an approach is better suited to identifying the dominant mechanisms related to actuation, but not in providing a complete description of any single phenomenon. It is well known that the performance of an IPT depends strongly on the nature of the electrodes, and many other studies have focused specifically on the electrodes on an IPT. The methods used in this work agree with previous studies in demonstrating the importance of the nature of the electrodes in the performance of an IPT. To optimize IPT performance, electrodes should be formed which maximize the amount of charge transferred, since the boundary layer pressures which drive solvent movement vary with Q^2.

The homogenization procedure within the micromechanics framework is another central assumption, where a dilute distribution of spherical clusters of uniform size was presumed. Because the polymer backbone material is assumed to be linearly elastic and interactions between clusters are considered negligible, the spherical microstructure only plays a role when calculating effective electrostatic cluster pressures. Recent research has demonstrated that the ionic aggregates in Nafion may be cylindrical, not spherical [29, 30, 31]. Changing to an assumption of a cylindrical microstructure would change the expressions which represent electrostatic interactions, but the dominant behavior would still show a Q^2 dependence. If a nonlinear elastic model of polymer chain deformation was used, along with a higher-order mixing approach to account for neighboring clusters, the assumption of microstructure would enter the model calculations and make a larger impact on model predictions. In short,

the current model is only weakly dependent on polymer morphology because of the simplifying assumptions that were made, and a higher-order approach would need to be taken to specifically relate morphological properties to actuation and charge transport behavior. This becomes important when comparing the behavior of different ionomers (i.e. other than Nafion), and will be a topic of future research.

In Eq. 4.8, the anion surface charge density of a cluster was calculated by assuming the number of ionic groups per cluster stays constant as the cluster expands or contracts. As an ionomer takes up more solvent, the clusters will combine and form larger clusters with an increased number of ionic groups per cluster [24, 27, 32, 90]. Assuming that the radius of the cluster varies with the cube root of solvent uptake, Eq. 4.8 gives $q \propto w^{-2/3}$. Defining ν such that $q \propto w^{\nu}$, the combination of clusters leads to $\nu > -2/3$. The combination of two spherical clusters with radius a to make one larger spherical cluster with radius A, for example, leads to an increase of surface charge density by a factor of $2^{1/3}$, since $A^3/a^3 = 2$. Since electrostatic pressures vary with q^2, the combination of clusters to make larger clusters will relatively increase electrostatic pressures, and the inclusion of this effect in the model would tend to increase predictions for boundary layer uptakes and actuation response. Including this effect would ultimately change model predictions for electromechanical coupling, since it would alter the relationship between electrostatic pressure and solvent uptake, which is the dominant relationship in relating charge transferred to actuation response.

Finally, because a linearized expression is used to calculate tip displacement (Eq. 5.7), any solution using this expression will lose some information. For example, the model predictions for backrelaxation using Eq. 5.7 depend largely on the relative sizes of the boundary layers. The effect of this difference is exaggerated using Eq. 5.6 because of the $1/L_{BL}^2$ dependence. In a complete numerical solution, the relation of relative boundary layer sizes in determining the extent of any backrelaxation would be different from the linearized solution. When looking at a complicated balance of different interactions such as this, the linearized solution can be used to identify important relationships, but a more complete analysis needs to be done before drawing firm conclusions.

Chapter 11

Conclusions and Suggestions for Future Work

In this work a physical model of IPT actuation was developed using NPP theory for charge transport. Actuation was expressed as a function of boundary layer expansion from solvent transport, which was calculated according to osmotic and electrostatic cluster pressures. Free air actuation and the finite size of the counter-cations were considered, showing that the movement of the large ions of the ionic liquid under the applied field will have a significant effect on the actuation response. Numerical simulations considering 3 mobile ionic species were performed, showing differences in charge transfer characteristics that are unique to ionic-liquid IPTs versus their water-based counterparts. A modified theory to model ion flux considering the large sizes of the ionic liquid ions was discussed along with the implications this has towards actuation. This chapter gives an overview of the various results and conclusions in the text, along with directions of future research.

In Chapter 9, numerical results were presented for the transient ion concentrations and charge density in an IPT. Considering a single mobile ionic species, the numerical simulations demonstrated the formation of the boundary layers (Figure 9.1) and the effect of actuator thickness on boundary layer charge dynamics (Figure 9.2). The time to form boundary layers was found numerically to vary linearly with actuator thickness, which is in agreement with Ref. [88] where the charging time scale is established as $\tau_C = \lambda h / D$. Numerical simulations were performed using classic NPP theory considering 3 mobile ionic species and varying the initial ion concentration and diffusion coefficients. The results show the emergence of two

time scales which correspond to migration and diffusion: a charging time scale τ_C and a diffusive time scale $\tau_D = h^2/D$. With 3 mobile ionic species, the anode boundary layer now has an increasingly negative charge density, whereas with 1 mobile ionic species the charge density is constant, corresponding to the fixed anions. With the additional mobile ions in the system, the capacitance increases since more charge is now being transferred.

To extend these results to the general case, the finite size of the ionic liquid ions needs to be accounted for in the governing equations for charge transport. NPP theory is clearly limited to low applied potentials in regards to ion transport in ionic liquids, since the large ionic liquid ions will cause a maximum concentration to be quickly reached. A modified theory which accounts for the finite size of the ions was outlined in Section 3.3, and although numerical simulations were not performed which included this modification, some of the effects were discussed in Section 10.2. Classic NPP theory may not even be applicable to ion transport in an ionic liquid IPT at the relatively low applied potential of 0.25 V, demonstrated by the large predictions for ionic liquid ion concentration at the electrodes shown in Section 9.2. To determine the range of applicability of NPP theory in describing electrochemical migration in an ionic liquid, experiments need to be performed so that results can be compared with theoretical considerations.

In Chapter 7 it was found that Nafion swollen with ionic liquid shows the same general trend as Nafion swollen with water for modulus vs. uptake. As discussed in Section 10.1, this can be reasonably expected due to the sample preparation procedure. To investigate the effects of the ionic liquid on the mechanical properties of Nafion when the ionic liquid is incorporated at higher temperatures (near T_g), further systematic testing would need to be done.

In Chapter 8 the actuation model was applied to describe actuation in an ionic liquid IPT, showing that the general trend is captured well and in agreement with experimental results. The model demonstrates that electrostatic interactions are dominant in actuation, and specifically that electrostatic boundary layer pressures will vary with charge density squared. The actuation of an IPT is quite complex and consists of a variety of nonlinear phenomena which much be modeled in a complete description of actuation. To form a reasonable model, approximations and simplifying assumptions are needed, and the effects of a few key assumptions were discussed in Section 10.4. These include assumptions of polymer microstructure, the continuum representation of ion and solvent transport and polymer deformation, and loss of solution accuracy due to linearization. Also, the effect of multiple

mobile ionic species was neglected in the model results of Chapter 8. As discussed in Section 10.3, the effect of multiple mobile ionic species on actuation performance depends on several different factors and a simple conclusion cannot be made.

Several areas of future work can be identified from the results discussed in this work. In the actuation model, the treatment of the polymer backbone as a continuum with linearly elastic constitutive relations makes the model results only weakly dependent on polymer morphology. Additionally, microstructural assumptions affect electromechanical coupling predictions since the electrostatic pressures are dependent on the geometry of a cluster, which also can vary with uptake when clusters expand and combine. Future work will be directed towards modeling of the polymer microstructure, and of structural evolution with respect to solvent uptake, so that the effects of different ionomer membranes and treatment procedures can be modeled.

Further analysis also needs to be done in order to understand and accurately model the charge transfer characteristics when an ionic liquid is used as solvent. Future work will be directed towards a full numerical and analytical analysis using the modified theory of Section 3.3, along with a comparison of experimental and theoretical/numerical results for the capacitance/voltage relationship of ionic liquid and water-based IPTs. Experimentally, ac voltammetry or a related technique can be used to measure the capacitance/voltage relationship of the IPT. With an accurate model of charge transfer, the full effects of multiple mobile ionic species migration can be included in the actuation model. An improved actuation model of ionic liquid IPTs would also include volumetric strain due to the migration of the ionic liquid ions, and a more complete analytical/numerical analysis, so that some approximations and linearizations are avoided and firm conclusions in regards to actuation performance can be made.

Ionic polymer transducers are an interesting class of smart materials with promising applications as soft sensors and actuators due their low actuation voltages. However, the limited understanding of actuation mechanisms and their dependence on various performance parameters currently limits the direct use of these devices. Higher performance, in areas such as force output, is needed before IPT actuators find a wide variety of practical use. In this work, a physics-based model of IPT actuation was developed based on a previous model by Nemat-Nasser [12] in order to establish the dominant mechanisms of actuation along with specific topics which merit further investigation. With a better a understanding of the underlying mechanisms of actuation, the performance of future devices can be improved, and

IPTs may one day find use in a wide variety of applications.

11.1 Specific Contributions

- Modeling framework for describing multiple mobile ionic species ionic migration in ionic liquid IPTs. Numerical simulations show distinct differences in boundary layer formation, which depends on the relative diffusion coefficients and fraction of "free" ionic liquid ions. Future work will include the use of a modified theory of ion transport which can describe higher applied voltages, and the comparison of these theories with experimental results.

- Numerical simulations considering a single mobile ionic species verified the linear dependence of boundary layer formation time on actuator thickness.

- Experimental measurements and modeling of Nafion swollen with ionic liquid. Results show that the ionic liquid does not specifically change the relationship of modulus vs uptake in comparison to other solvents, when the ionic liquid is incorporated at room temperature. However, swelling with ionic liquid while heating near T_g may yield different results.

- Analysis of local cluster interactions during actuation reveals the dependence of osmotic and electrostatic cluster pressures on the charge distribution in the membrane. To a first order approximation, osmotic pressure varies linearly with charge density and electrostatic pressure varies with charge density squared. These derivations, based on model considerations within a micromechanics framework, are in agreement with previous empirical models, providing an explanation as to why these models succeed in fitting experimental data. The modeling framework established here can also be extended to model electromechanical coupling in IPTs considering different microstructural parameters, which will be a topic of future work.

- The actuation model applied to an ionic liquid IPT was shown to capture the essential actuation behavior. Parts of the model were identified which can be improved upon in order to make solid conclusions in regards to actuation performance. These include a more accurate analytical analysis or complete numerical analysis of the model governing equations and the use of a higher-order nonlinear model of polymer backbone

deformation to explicitly include the effects of polymer microstructure in the actuation predictions. For an ionic liquid IPT, the finite size of the mobile ions moving under the applied field also contributes to the swelling of the boundary layers, as demonstrated in Section 8.3, and should be included in a complete analysis of ionic liquid IPT actuation. These considerations will also be topics of future work.

- The general discussions and overall analysis presented in this thesis contribute to the understanding of the physical mechanisms of IPT actuation, and provide a modeling framework where important relationships can specifically be investigated.

Appendix A

Matrix Definitions for FEM Solution of NPP Equations

The matrices $\mathbf{M}$, $\mathbf{r}$, $\mathbf{f}$, and $\frac{\partial \mathbf{r}}{\partial \mathbf{q}}$ from Eqs. 3.30 and 3.31 are defined using the weak form of the governing equations shown in Eq. 3.27. The formulation used here follows Lim [51], but here there are 3 mobile ionic species. To define the mass matrix $\mathbf{M}$, first let

$$m_{AB}^e = \int_{x_e}^{x_{e+1}} N_A N_B dx \tag{A.1}$$

where x_e and x_{e+1} are the nodal coordinates of element e. Using this, define the matrices

$$\mathbf{a} = \begin{bmatrix} m_{11}^e & m_{22}^e \\ m_{21}^e & m_{22}^e \end{bmatrix} \qquad \mathbf{b} = \begin{bmatrix} m_{13}^e & m_{14}^e \\ m_{23}^e & m_{24}^e \end{bmatrix} \qquad \mathbf{c} = \begin{bmatrix} m_{33}^e & m_{34}^e \\ m_{43}^e & m_{44}^e \end{bmatrix} \tag{A.2}$$

These are then used to make the additional definitions

$$\mathbf{A} = \begin{bmatrix} 0 & 0 & 0 & 0 \\ 0 & \mathbf{a} & 0 & 0 \\ 0 & 0 & \mathbf{a} & 0 \\ 0 & 0 & 0 & \mathbf{a} \end{bmatrix} \qquad \mathbf{B} = \begin{bmatrix} 0 & 0 & 0 & 0 \\ 0 & \mathbf{b} & 0 & 0 \\ 0 & 0 & \mathbf{b} & 0 \\ 0 & 0 & 0 & \mathbf{b} \end{bmatrix} \qquad \mathbf{C} = \begin{bmatrix} 0 & 0 & 0 & 0 \\ 0 & \mathbf{c} & 0 & 0 \\ 0 & 0 & \mathbf{c} & 0 \\ 0 & 0 & 0 & \mathbf{c} \end{bmatrix} \tag{A.3}$$

where each 0 represents a 2×2 sub-matrix. Now, the mass matrix for element e is expressed as

$$\mathbf{M}^e = \begin{bmatrix} \mathbf{A} & \mathbf{B} \\ \mathbf{B}^T & \mathbf{C} \end{bmatrix} \tag{A.4}$$

and these are assembled in typical fashion to form the global matrix $\mathbf{M}$.

The forcing matrix $\mathbf{f}$ corresponds to the terms

$$\left[N_A \frac{dN_B}{dx} \phi_B \right]_{-h^*}^{h^*} \tag{A.5}$$

and

$$[N_A J_i]_{-h^*}^{h^*} \tag{A.6}$$

in Eq. 3.27, where $i = 1, 2, 3$. The zero flux boundary condition in Eq. 3.25 means that all the terms in Eq. A.6 will be zero. Eq. A.5 will place two nonzero terms in $\mathbf{f}$ at the corresponding global positions of ϕ_1 and ϕ_{2ne+1} in $\mathbf{q}$, where ϕ_j refers to the jth global degree of freedom of potential, ne is the number of elements, and the total number of nodal degrees of freedom for potential (and for each concentration variable) is $2(ne + 1)$. In the numerical procedure, rows and columns of the global matrices which correspond to the known variables are removed, so the forcing matrix can simply be defined as

$$\mathbf{f} = \{0\} \tag{A.7}$$

The known nodal variables ϕ_1 and ϕ_{ne+1} are given the values $+V_0^*/2$ and $-V_0^*/2$, respectively. Using the zero flux boundary condition, the nodal variables corresponding to the concentration gradient at the boundary are set as $c_2^i = -c_1^i z_i \phi_2$ and $c_{2(ne+1)}^i = -c_{2ne+1}^i z_i \phi_{2(ne+1)}$ with $i = 1, 2, 3$ for the different ions, where again the subscripts refer to global degrees of freedom. Note that since the Hermite shape functions are used, the second degree of freedom at each node represents the negative gradient of the primary nodal variable, e.g. $c_2^i = -\frac{\partial c_i(-h^*)}{\partial x}$.

The matrix $\mathbf{r}$ consists of the remaining terms in Eq. 3.27, which can be defined over a single

element as

$$\Xi_A^e = \int_{x_e}^{x_{e+1}} \left(-\frac{dN_A}{dx}\frac{dN_B}{dx}\phi_B + N_A \left[N_B \sum_{j=1}^{3} z_j c_B^j - 1 \right] \right) dx$$

$$\Lambda_A^{(e,i)} = \int_{x_e}^{x_{e+1}} D_i \frac{dN_A}{dx} \left(\frac{dN_B}{dx}c_B^i + z_i N_B c_B^i \frac{dN_K}{dx}\phi_K \right) dx \tag{A.8}$$

Using this, define the element matrix

$$\mathbf{r}^e = \left\{ \Xi_1^e, \Xi_2^e, \Lambda_1^{(e,1)}, \Lambda_2^{(e,1)}, \Lambda_1^{(e,2)}, \Lambda_2^{(e,2)}, \Lambda_1^{(e,3)}, \Lambda_2^{(e,3)}, \Xi_3^e, \Xi_4^e, \Lambda_3^{(e,1)}, \Lambda_4^{(e,1)}, \Lambda_3^{(e,2)}, \Lambda_4^{(e,2)}, \Lambda_3^{(e,3)}, \Lambda_4^{(e,3)} \right\}$$
$$\tag{A.9}$$

and use this to assemble the global matrix $\mathbf{r}$.

To use Newton-Raphson iteration to solve the system of equations, the tangent matrix

$$\mathbf{T} = \frac{\partial \mathbf{r}}{\partial \mathbf{q}} \tag{A.10}$$

needs to be calculated. In Ref. [51], $\mathbf{T}$ is determined through careful bookkeeping of the algebraic manipulations. Although more computationally expensive, a much simpler and more easily generalized calculation of $\mathbf{T}$ is straightforward using symbolic manipulation and functional programming constructs in Mathematica. Assuming that $\mathbf{q}$ contains a complete list of the undefined nodal variables $\mathbf{q}$ and the components of $\mathbf{r}$ are stored in $\mathbf{r}$, the tangent matrix is calculated with

```
Map[Function[{var},D[#,var]],q]&/@r;
```

This argument creates a vector of derivative operators which is then mapped to operate on each element of $\mathbf{r}$. In this fashion the tangent matrix can be calculated for an arbitrary set of nonlinear differential equations with an arbitrary set of nodal variables.

Appendix B

Derivation of Electrostatic Cluster Pressure

In this appendix the equations for electrostatic cluster pressure considering both surface and volume charge distribution of cations (Eqs. 4.21 and 4.22) are derived in detail. A surface charge density of cations will be considered first, since this is the simpler of the two cases. This system is described by first considering two spheres as shown in Figure B.1. The inner sphere has a total charge which corresponds to the cations contained in the cluster. In the model framework, this charge is calculated by first defining the absolute value of the total anion charge on the surface of a cluster as

$$Q_0 = 4\pi a^2 q \tag{B.1}$$

where a is the cluster radius and q is the cluster surface charge density, which is calculated using Eq. 4.8. The total charge of the cluster is $Q_0 Q$, where Q is the normalized ion charge density defined in Eq. 4.9. Therefore, the total charge of the cations on the surface of the inner sphere is simply $Q_0(Q + 1)$. The configuration energy, or work done to assemble the charge distribution, is calculated as

$$W = \frac{\epsilon}{2} \int_0^\infty \int_0^\pi \int_0^{2\pi} E^2 r^2 \sin\theta \, dr \, d\theta \, d\phi \tag{B.2}$$
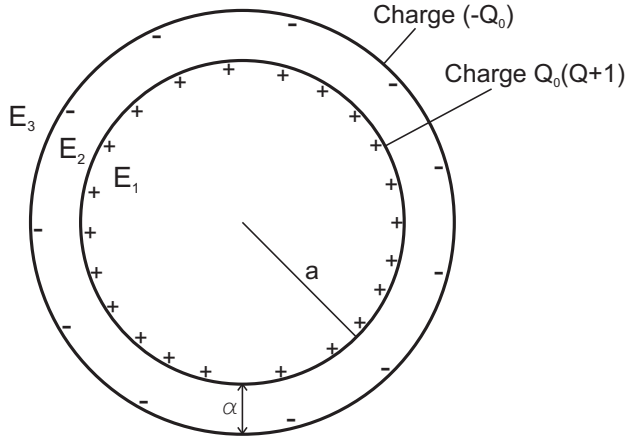
Figure B.1: The representation for the electrostatic calculations of a cathode boundary layer cluster with positive net charge, showing two surface charge distributions.

For the surface charge distribution, there is no electric field inside the inner sphere, so the electric fields in the different regions are expressed as

$$
\begin{aligned}
0 < r < a \qquad & E_1 = 0 \\
a < r < a + \alpha \qquad & E_2 = \frac{Q_0(Q+1)}{4\pi\epsilon r^2} \\
a + \alpha < r < \infty \qquad & E_3 = \frac{Q_0 Q}{4\pi\epsilon r^2}
\end{aligned}
\tag{B.3}
$$

Using these in Eq. B.2 yields

$$
W_e = \frac{Q_0^2}{8\pi\epsilon}\left(\frac{Q^2}{a+\alpha} + (Q+1)^2 \left[\frac{1}{a} + \frac{1}{a+\alpha} \right] \right)
\tag{B.4}
$$

The radial force acting on the surface of the cluster is the change in configuration energy with respect to a change in cluster radius, i.e.

$$
\begin{aligned}
F_e &= -\frac{dW}{da} \\
&= \frac{Q_0^2}{8\pi\epsilon}\left(\frac{Q^2}{(a+\alpha)^2} + (Q+1)^2 \left[\frac{1}{a^2} + \frac{1}{(a+\alpha)^2} \right] \right)
\end{aligned}
\tag{B.5}
$$

Because of symmetry, the energy in Eq. B.4 only depends on the cluster radius, and the force is uniformly distributed on the surface of the cluster. The effective pressure which will tend to expand or contract the cluster is the force acting normal to the surface divided by
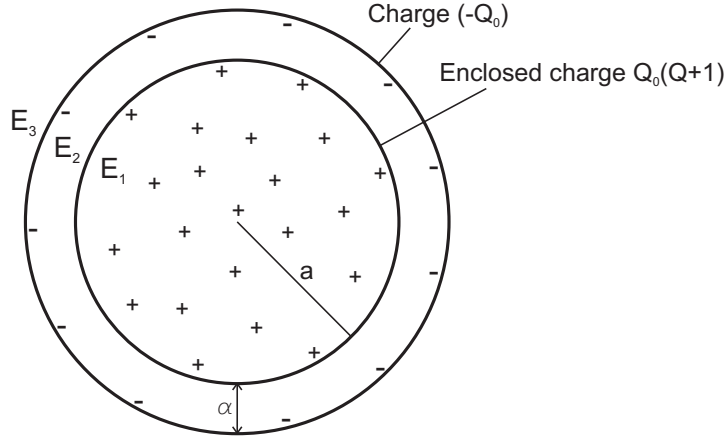
Figure B.2: A cathode boundary layer cluster with positive net charge, where a uniform volume charge density of cations and a uniform surface charge density of anions is assumed.

the surface area. For a sphere, the surface normal vector is always in the radial direction. The pressure is now calculated and simplified using the definition of Q_0:

$$
\begin{aligned}
P_e &= \frac{F}{4\pi a^2} \\
&= \frac{q^2}{2\epsilon}\left(Q^2 \frac{a^2}{(a+\alpha)^2} + (Q+1)^2\left[1 - \frac{a^2}{(a+\alpha)^2}\right]\right)
\end{aligned}
\tag{B.6}
$$

Note that making the substitution for Q_0 after taking the derivative with respect to cluster radius to find force is equivalent to saying the total charge, or the number of ionic groups per cluster, stays constant as the cluster expands or contracts. If the substitution was made before taking the derivative in Eq. B.5, then the surface charge density would be assumed constant. If the change in total cluster charge (i.e. the number of ionic groups per cluster) with respect to a change in radius was known, then this could be included to find the force acting on the surface of the cluster. These assumptions have a direct impact on the model predictions for electromechanical coupling and the overall actuation response.

Now, consider a constant volume charge density of cations inside the cluster as shown in Figure B.2. The electric field in the different regions is now given by

$$0 < r < a \qquad E_1 = \frac{Q_0(Q+1)r}{4\pi\epsilon a^3}$$
$$a < r < a + \alpha \qquad E_2 = \frac{Q_0(Q+1)}{4\pi\epsilon r^2}$$
$$a + \alpha < r < \infty \qquad E_3 = \frac{Q_0 Q}{4\pi\epsilon r^2} \tag{B.7}$$

Since the fields in regions 2 and 3 are the same as above, the energy can be calculated as

$$W_{vol} = W_e + \frac{4\pi\epsilon}{2} \int_0^a E_1^2 r^2 dr$$
$$= W_e + \frac{Q_0^2}{8\pi\epsilon} \frac{(Q+1)^2}{5a} \tag{B.8}$$

The total force acting on the cluster is

$$F_{vol} = F_e + \frac{Q_0^2}{8\pi\epsilon} \frac{(Q+1)^2}{5a^2} \tag{B.9}$$

Taking the pressure as force divided by surface area and simplifying using the definition of Q_0 leads to

$$P_{vol} = \frac{q^2}{2\epsilon} \left(Q^2 \frac{a^2}{(a+\alpha)^2} + (Q+1)^2 \left[\frac{6}{5} - \frac{a^2}{(a+\alpha)^2} \right] \right) \tag{B.10}$$

This is the electrostatic pressure acting to expand or contract the cluster when a volume charge density of cations is assumed. Looking at Eqs. B.6 and B.10, the squared charge density and the condition of $\alpha > 0$ cause the calculated pressures to always be positive, i.e. they predict that the cluster will always tend to expand in order to reach a state of minimum potential energy. This result comes from the assumption of cation and anion pairs aligning radially, which is a configuration that does not minimize electrostatic free energy. At low solvent uptakes where clusters are smaller and only consist of a few ion pairs (and little to no solvent), this is not a good assumption; at these uptakes it is known that electrostatic interactions between ion pairs are favorable (which would create an effective negative pressure), and this is the driving force behind ionic aggregation and the initial formation of clusters in the ionomer. Therefore, Eqs. B.6 and B.10 are not applicable to ionomers in a dry state or at very low solvent uptakes. These equations are intended to describe electrostatic interactions for typical conditions of IPT actuation, which consist of sufficient solvent uptakes and nonzero net cluster charge in the boundary layers.

Appendix C

Tip Displacement Using the Euler-Bernoulli Beam Theory

The eigenstrain generated by cluster expansion is defined as

$$e_v = \ln\left(1 + w\right) = \ln\left(\frac{V_{polymer} + V_{solvent}}{V_{polymer}}\right) \tag{C.1}$$

Assuming an isotropic material, the axial strain is calculated to be

$$e_z = \ln\left((1 + w)^{\frac{1}{3}}\right) = \frac{1}{3}e_v \tag{C.2}$$

where the coordinate system is shown in Figure C.1. For an IPT in a cantilever configuration, the maximum axial strain will occur at $x = H$, i.e. $e_z(H) = e_{max}$ where $2H$ is the thickness of the IPT as shown in Figure C.1. Euler-Bernoulli beam theory is used to relate this strain
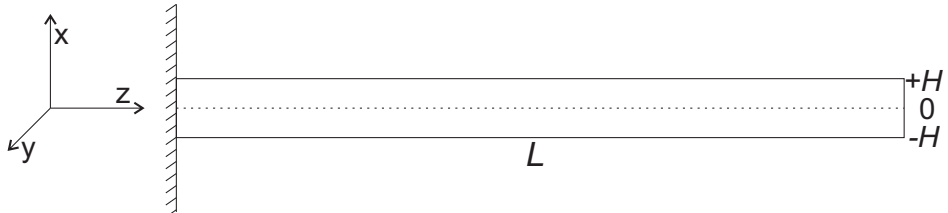

Figure C.1: A diagram of an IPT in a cantilever configuration, showing the coordinate axes.

to the tip displacement, u, using

$$e_{max} = \frac{2Hu}{L^2} \tag{C.3}$$

where L is the length of the IPT. The transducer is assumed to bend with constant curvature along its length, so e_{max} is not a function of position in the z-direction. The bending moment acting on a cross section of the IPT is calculated with

$$M = \int_{-H}^{H} Y(x) e_z(x) x dx \tag{C.4}$$

where $Y(x)$ is the local Young's modulus. Using Eq. C.3, the integral in Eq. C.4 is approximated to obtain [12]

$$M = \frac{e_{max}}{H} \int_{-H}^{H} Y(x)x^2 dx \approx \frac{2}{3} e_{max} H^2 \left(3Y_{IPT}(\bar{w}) - 2Y_B(\bar{w})\right) \tag{C.5}$$

where $Y_{IPT}(\bar{w})$ and $Y_B(\bar{w})$ are the Young's modulus of the IPT and the bare polymer, respectively, both evaluated at the average solvent in the transducer, $\bar{w}$.

The bending moment created by the volumetric expansion of the boundary layers is calculated using Eqs. C.1, C.2, and C.4:

$$M_{BL} = \frac{1}{3} \int_{-h}^{h} Y_B(x,t)x \ln\left(1 + w(x,t)\right) dx \tag{C.6}$$

where the limits of integration are from $-h$ to h because eigenstrains develop only in the polymer (not the metal layers) in this simplified representation. The modulus of the polymer will vary in the boundary layers due to changes in solvent uptake and also due to the cations acting as pseudo cross-linkers with the polymer chains [12]. However, the latter effect is ignored and the modulus is represented with the empirical fit shown in Section 8.1.

Combining Eqs. C.3, C.5, and C.6, the normalized tip displacement is expressed as

$$\frac{u}{L} = \frac{L}{4H^3 \left(3Y_{IPT} - 2Y_B\right)} \int_{-h}^{h} x Y_B(x,t) \ln\left(1 + w(x,t)\right) dx \tag{C.7}$$

Since the volumetric strain rate $\dot{e}_v$ is readily expressed as a function of the pressure gradient

using Eqs. 4.1 and 5.3, it is convenient to express the tip displacement rate

$$\frac{\dot{u}}{L} = \frac{L}{4H^3 \left(3Y_{IPT} - 2Y_B\right)} \int_{-h}^{h} x Y_B(x,t) \frac{\dot{w}(x,t)}{1 + w(x,t)} dx \qquad \text{(C.8)}$$

where the term containing $\dot{Y}_B(x,t)$ is ignored since the rate of change of the local modulus is expected to be small.

Appendix D

Animations of Numerical Simulations (Electronic Version)

## D.1   1 Mobile Ionic Species Concentration Profile
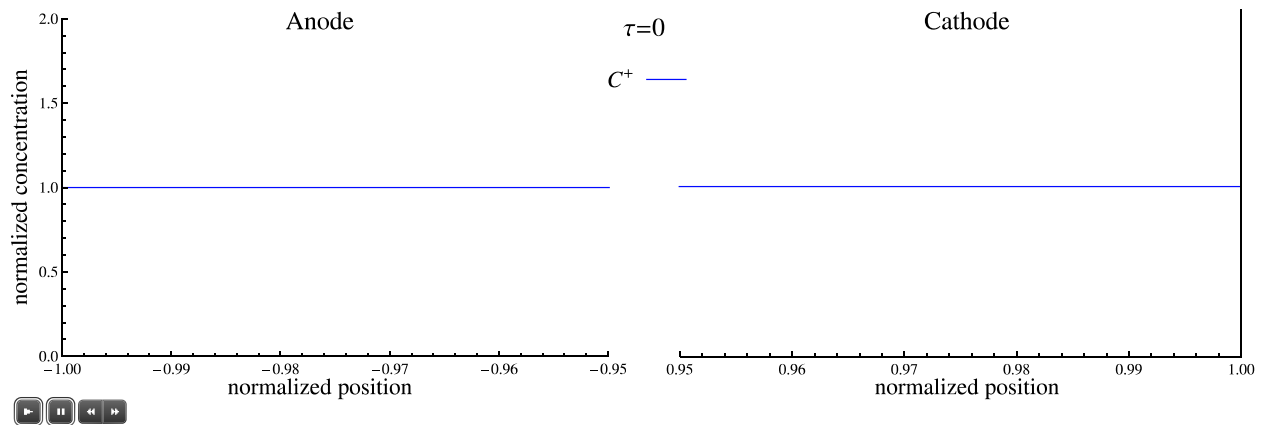
Figure D.1: Animation of concentration profiles with respect to time for a single mobile cation species, C$^+$, with an applied voltage of $V_0 = 1$ V. Only the boundary layers nearest the electrodes are shown. Note the asymmetry in the charge distribution and the larger size of the anode boundary layer versus the cathode boundary layer.

D.2   3 Mobile Ionic Species Concentration Profiles with $D_{IL} = 1$ and $F_{IL} = 0.5$
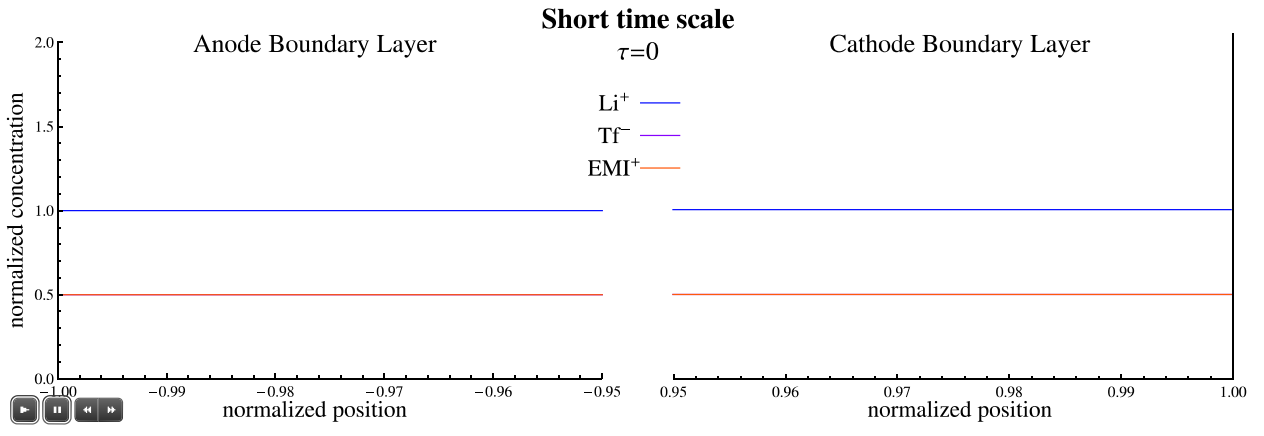

(a) Short time scale with $D_{IL} = 1$, $F_{IL} = 0.5$.
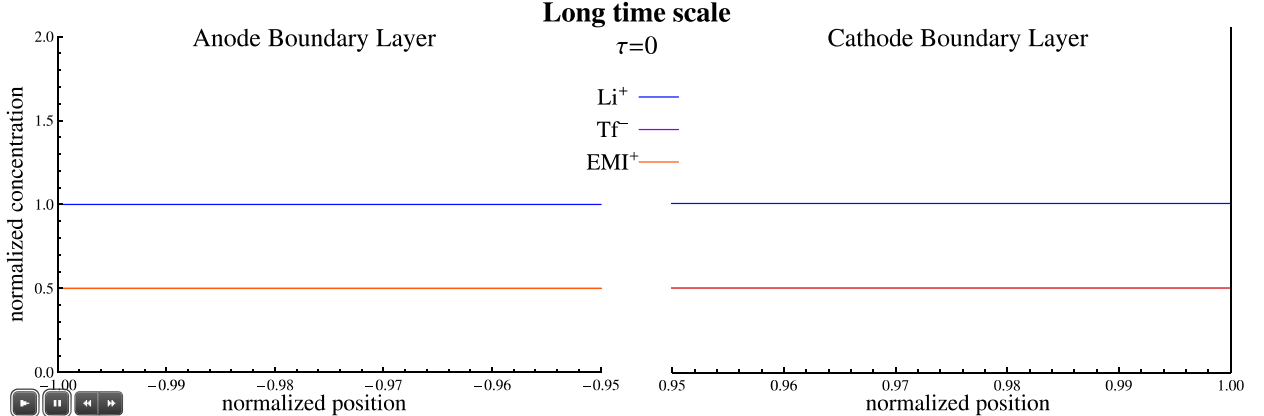
(b) Long time scale with $D_{IL} = 1$, $F_{IL} = 0.5$.

Figure D.2: Animation of concentration profiles with respect to time for 3 mobile ionic species with $D_{IL} = 1$ and $F_{IL} = 0.5$, i.e. equal diffusion coefficients of all the ions and half as many "free" ionic liquid ions as mobile cations. At short time scales (a) there is migrative flux of ions towards the electrodes to form the boundary layers. At longer times (b), there is only diffusive flux outside of the boundary layers as the system moves towards equilibrium.

D.3 3 Mobile Ionic Species Concentration Profiles with $D_{IL} = 0.1$ and $F_{IL} = 0.5$
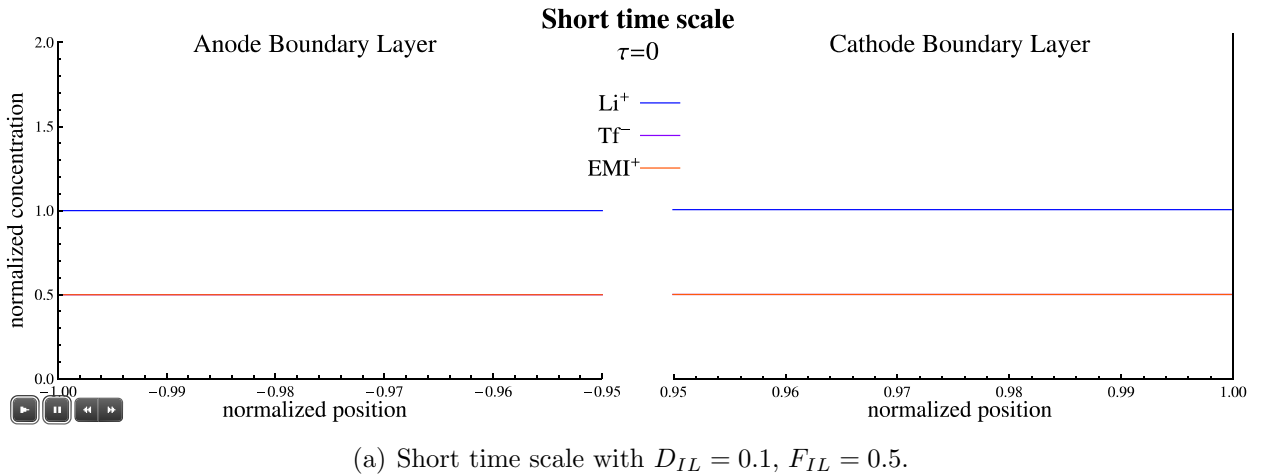
(a) Short time scale with $D_{IL} = 0.1$, $F_{IL} = 0.5$.
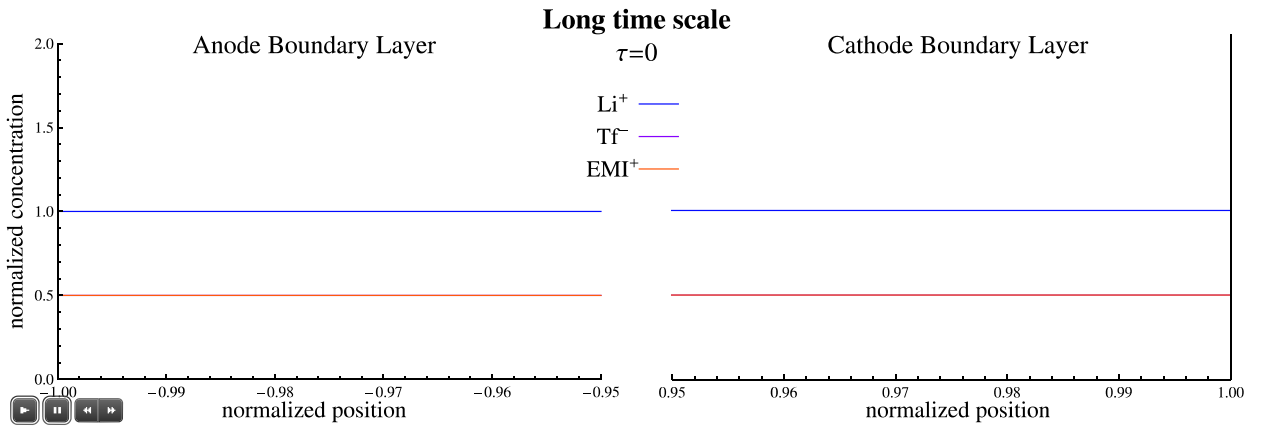
(b) Long time scale with $D_{IL} = 0.1$, $F_{IL} = 0.5$.

Figure D.3: Animation of concentration profiles with respect to time for 3 mobile ionic species with $D_{IL} = 0.1$ and $F_{IL} = 0.5$, i.e. the ionic liquids ions have diffusion coefficients 1/10 of the counter-cations and there are half as many "free" ionic liquid ions as mobile cations. At short time scales (a) the non-monotonic charging profile is quite distinct, especially in the ABL, since there is an order of magnitude difference in the diffusion coefficients of the ions. At longer times (b) it is seen that the concentrations of the ions just outside of either boundary layer either initially increase and then decrease or initially decrease and then increase.

D.4 3 Mobile Ionic Species Concentration Profiles with $D_{IL} = 0.1$ and $F_{IL} = 0.1$
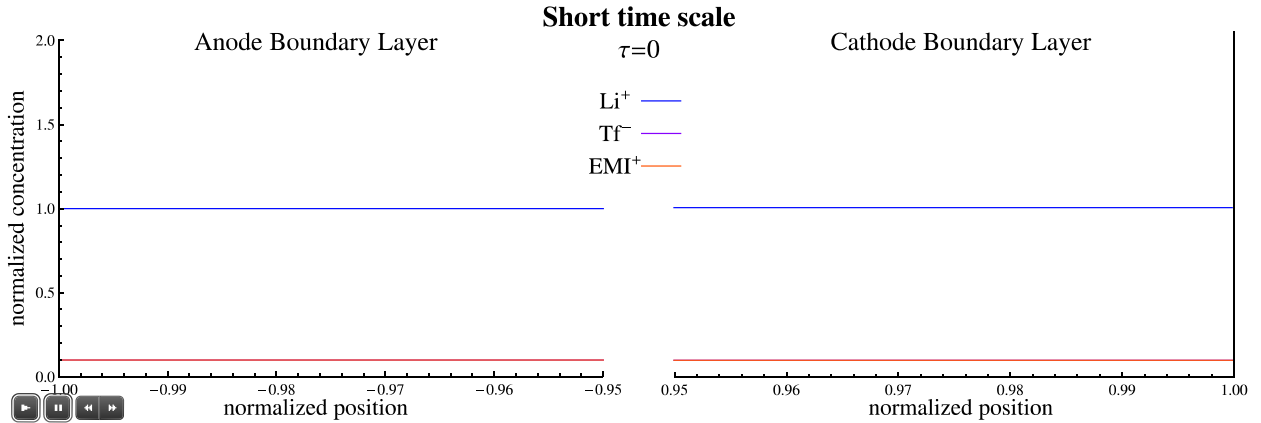

(a) Short time scale with $D_{IL} = 0.1$, $F_{IL} = 0.1$.
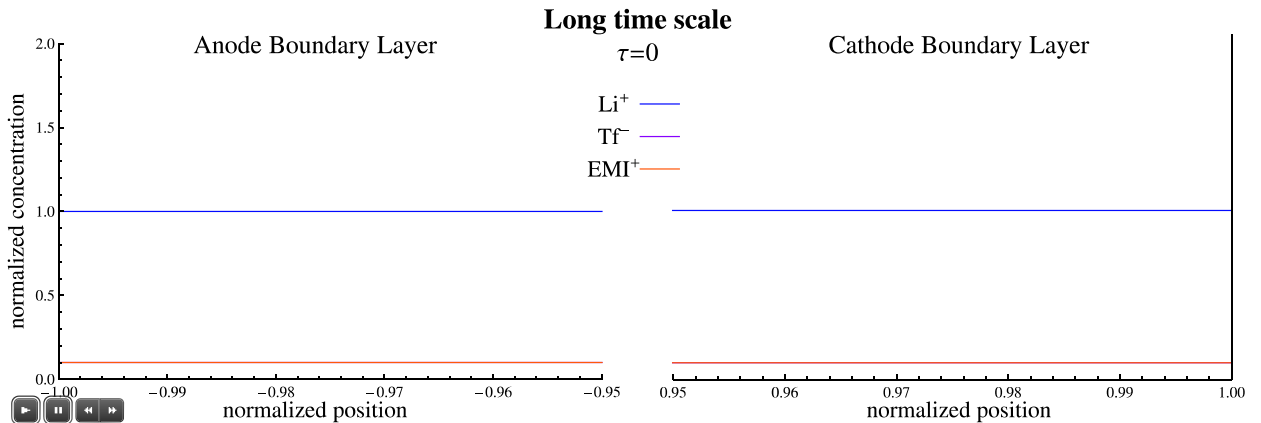
(b) Long time scale with $D_{IL} = 0.1$, $F_{IL} = 0.1$.

Figure D.4: Animation of concentration profiles with respect to time for 3 mobile ionic species with $D_{IL} = 0.1$ and $F_{IL} = 0.1$, i.e. the ionic liquids ions have diffusion coefficients 1/10 of the counter-cations and there are also 1/10 as many "free" ionic liquid ions as mobile cations. When there are fewer "free" ion liquid ions, the counter-cation is the main charge carrier; Figures (a) and (b) resemble Figure D.1 more closely than either Figure D.2 or Figure D.3. At long time scales (b) the non-monotonic charging profile and relaxation towards equilibrium is still evident, but it is not nearly as pronounced as the case of a larger amount of "free" ionic liquid liquids ions shown in Figure D.3.

## D.5 Monte Carlo Simulation of Local Ion Distribution
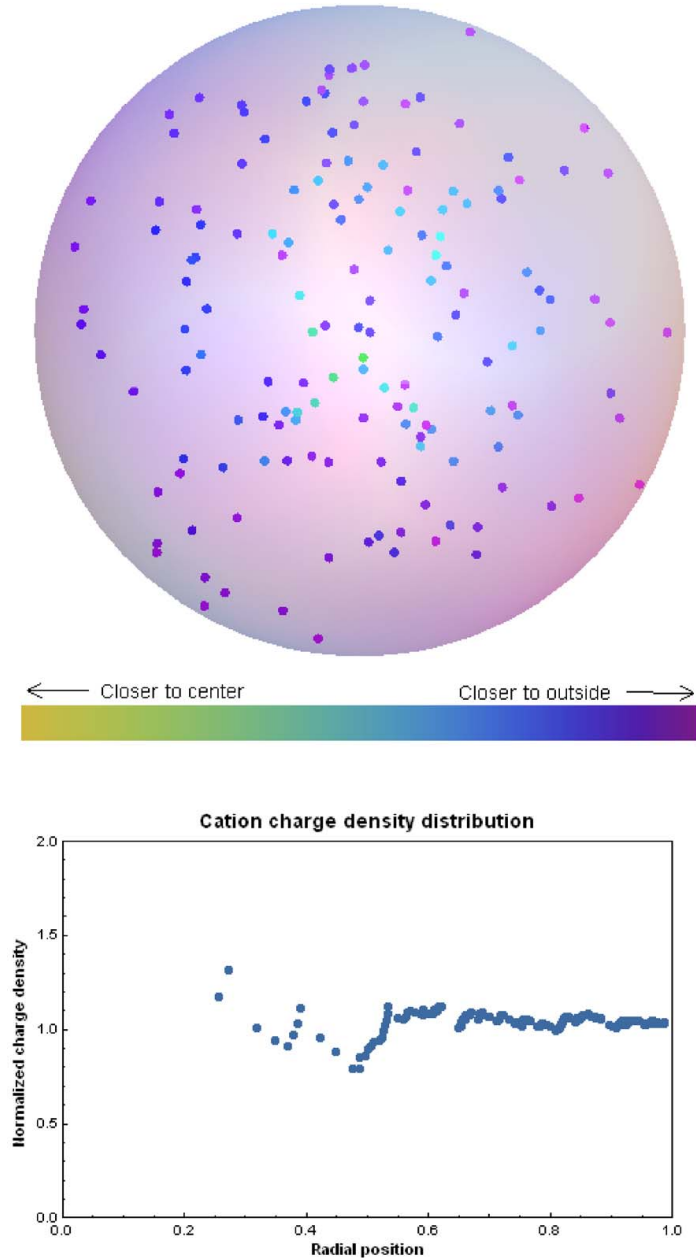
Figure D.5: A run of the Monte Carlo simulation of local ion distribution, showing the evolution of the positions of the cations as the system moves towards a state which minimizes free energy. Click to play. The cations are seen to move towards the outside of the sphere as the system moves towards equilibrium.

Bibliography

[1] M. D. Bennett and D. J. Leo, "Ionic liquids as stable solvents for ionic polymer transducers," *Sensors and Actuators A: Physical*, vol. 115, pp. 79–90, Sept. 2004.

[2] P. Bonhote, A. Dias, N. Papageorgiou, K. Kalyanasundaram, and M. Gratzel, "Hydrophobic, highly conductive ambient-temperature molten salts," *Inorganic Chemistry*, vol. 35, pp. 1168–1178, Feb. 1996.

[3] J. Bockris and A. Reddy, *Modern Electrochemistry 1*. New York: Plenum Press, 1998.

[4] K. M. Newbury and D. J. Leo, "Linear electromechanical model of ionic polymer transducers - Part I: Model development," *Journal of Intelligent Material Systems and Structures*, vol. 14, pp. 333–342, June 2003.

[5] J. W. Paquette, K. J. Kim, J. Nam, and Y. S. Tak, "An equivalent circuit model for ionic polymer-metal composites and their performance improvement by a clay-based polymer nano-composite technique," *Journal of Intelligent Material Systems and Structures*, vol. 14, pp. 633–642, Oct. 2003.

[6] M. Porfiri, "Charge dynamics in ionic polymer metal composites," *Journal of Applied Physics*, vol. 104, Nov. 2008.

[7] B. J. Akle and D. J. Leo, "Characterization and modeling of extensional and bending actuation in ionomeric polymer transducers," *Smart Materials and Structures*, vol. 16, no. 4, pp. 1348–1360, 2007.

[8] C. S. Kothera, D. J. Leo, and S. L. Lacy, "Characterization and modeling of the nonlinear response of ionic polymer actuators," *Journal of Vibration and Control*, vol. 14, pp. 1151–1173, Aug. 2008.

[9] K. Asaka and K. Oguro, "Bending of polyelectrolyte membrane platinum composites by electric stimuli: Part II. Response kinetics," *Journal of Electroanalytical Chemistry*, vol. 480, no. 1-2, pp. 186–198, 2000.

[10] T. Wallmersperger, D. J. Leo, and C. S. Kothera, "Transport modeling in ionomeric polymer transducers and its relationship to electromechanical coupling," *Journal of Applied Physics*, vol. 101, no. 2, pp. 024912–9, 2007.

[11] M. Porfiri, "An electromechanical model for sensing and actuation of ionic polymer metal composites," *Smart Materials and Structures*, vol. 18, no. 1, p. 015016, 2009.

[12] S. Nemat-Nasser, "Micromechanics of actuation of ionic polymer-metal composites," *Journal of Applied Physics*, vol. 92, no. 5, pp. 2899–2915, 2002.

[13] S. Nemat-Nasser and S. Zamani, "Modeling of electrochemomechanical response of ionic polymer-metal composites with various solvents," *Journal of Applied Physics*, vol. 100, no. 6, pp. 064310–18, 2006.

[14] M. D. Bennett, D. J. Leo, G. L. Wilkes, F. L. Beyer, and T. W. Pechar, "A model of charge transport and electromechanical transduction in ionic liquid-swollen Nafion membranes," *Polymer*, vol. 47, pp. 6782–6796, Sept. 2006.

[15] M. D. Bennett, *Electromechanical Transduction in Ionic Liquid-Swollen Nafion Membranes*. PhD thesis, Virginia Tech, Nov. 2005.

[16] A. Eisenberg and J. Kim, *Introduction to Ionomers*. Wiley-Interscience, 1 ed., Apr. 1998.

[17] C. Heitner-Wirguin, "Recent advances in perfluorinated ionomer membranes: structure, properties and applications," *Journal of Membrane Science*, vol. 120, pp. 1–33, 1996.

[18] K. Mauritz and R. Moore, "State of understanding of Nafion," *Chemical Reviews*, vol. 104, pp. 4535–4586, Oct. 2004.

[19] J. Wang, C. Xu, M. Taya, and Y. Kuga, "A Flemion-based actuator with ionic liquid as solvent," *Smart Materials and Structures*, vol. 16, no. 2, pp. S214–S219, 2007.

[20] S. Nemat-Nasser and Y. Wu, "Comparative experimental study of ionic polymer–metal composites with different backbone ionomers and in various cation forms," *Journal of Applied Physics*, vol. 93, pp. 5255–5267, May 2003.

[21] A. J. Duncan, D. J. Leo, and T. E. Long, "Beyond Nafion: Charged macromolecules tailored for performance as ionic polymer transducers," *Macromolecules*, vol. 41, pp. 7765–7775, Nov. 2008.

[22] A. Eisenberg, "Clustering of ions in organic polymers. a theoretical approach," *Macromolecules*, vol. 3, no. 2, pp. 147–154, 1970.

[23] W. J. MacKnight, W. P. Taggart, and R. S. Stein, "A model for the structure of ionomers," *Journal of Polymer Science: Polymer Symposia*, vol. 45, pp. 113–128, 1974.

[24] D. J. Yarusso and S. L. Cooper, "Analysis of SAXS data from ionomer systems," *Polymer*, vol. 26, 1985.

[25] D. J. Yarusso and S. L. Cooper, "Microstructure of ionomers: Interpretation of Small-Angle x-ray scattering data," *Macromolecules*, vol. 16, pp. 1871–1880, 1983.

[26] A. Eisenberg, B. Hird, and R. B. Moore, "A new multiplet-cluster model for the morphology of random ionomers," *Macromolecules*, vol. 23, no. 18, 1990.

[27] T. D. Gierke and W. Y. Hsu, "The cluster-network model of ion clustering in perfluorosulfonated membranes," *ACS Symposium Series*, 1982.

[28] W. Hsu, J. Barkley, and P. Meakin, "Ion percolation and insulator-to-conductor transition in nafion perfluorosulfonic acid membranes," *Macromolecules*, vol. 13, pp. 198–200, 1980.

[29] K. Schmidt-Rohr and Q. Chen, "Parallel cylindrical water nanochannels in nafion fuel-cell membranes," *Nat Mater*, vol. 7, no. 1, pp. 75–83, 2008.

[30] L. Rubatat, G. Gebel, and O. Diat, "Fibrillar structure of Nafion: Matching fourier and real space studies of corresponding films and solutions," *Macromolecules*, vol. 37, pp. 7772–7783, 2004.

[31] L. Rubatat, A. Rollet, G. Gebel, and O. Diat, "Evidence of elongated polymeric aggregates in Nafion," *Macromolecules*, vol. 35, pp. 4050–4055, May 2002.

[32] D. A. Mologin, P. G. Khalatur, and A. R. Khokhlov, "Structural organization of water-containing Nafion: A cellular-automaton-based simulation," *Macromolecular Theory and Simulations*, vol. 11, pp. 587–607, 2002.

[33] P. Choi, N. Jalani, and R. Datta, "Thermodynamics and proton transport in Nafion - II. Proton diffusion mechanisms and conductivity," *Journal of the Electrochemical Society*, vol. 152, no. 3, pp. E123–E130, 2005.

[34] M. Eikerling, A. A. Kornyshev, and U. Stimming, "Electrophysical properties of polymer electrolyte membranes: A random network model," *Journal of Physical Chemistry B*, vol. 101, no. 50, pp. 10807–10820, 1997.

[35] M. Shahinpoor, Y. Bar-Cohen, J. O. Simpson, and J. Smith, "Ionic polymermetal composites (IPMCs) as biomimetic sensors, actuators and artificial musclesa review," *Smart Mater. Struct*, vol. 7, no. 6, 1998.

[36] K. J. Kim and M. Shahinpoor, "Ionic polymer-metal composites: II. Manufacturing techniques," *Smart Materials and Structures*, vol. 12, no. 1, pp. 65–79, 2003.

[37] M. Shahinpoor and K. J. Kim, "Ionic polymer-metal composites: I. Fundamentals," *Smart Materials and Structures*, vol. 10, pp. 819–833, 2001.

[38] M. Shahinpoor and K. J. Kim, "The effect of surface-electrode resistance on the performance of ionic polymer-metal composite (IPMC) artificial muscles," *Smart Materials and Structures*, vol. 9, no. 4, pp. 543–551, 2000.

[39] B. J. Akle, D. J. Leo, M. A. Hickner, and J. E. McGrath, "Correlation of capacitance and actuation in ionomeric polymer transducers," *Journal of Materials Science*, vol. 40, pp. 3715–3724, July 2005.

[40] B. Akle, M. Bennett, D. Leo, K. Wiles, and J. McGrath, "Direct assembly process: a novel fabrication technique for large strain ionic polymer transducers," *Journal of Materials Science*, vol. 42, no. 16, pp. 7031–7041, 2007.

[41] D. J. Leo, K. Farinholt, T. Wallmersperger, and Y. Bar-Cohen, "Computational models of ionic transport and electromechanical transduction in ionomeric polymer transducers (Invited paper)," vol. 5759, (San Diego, CA, USA), pp. 170–181, SPIE, May 2005.

[42] M. Porfiri, "Influence of electrode surface roughness and steric effects on the nonlinear electromechanical behavior of ionic polymer metal composites," *Physical Review E (Statistical, Nonlinear, and Soft Matter Physics)*, vol. 79, pp. 041503–13, Apr. 2009.

[43] M. Shahinpoor and K. J. Kim, "Ionic polymer-metal composites: III. Modeling and simulation as biomimetic sensors, actuators, transducers, and artificial muscles," *Smart Materials and Structures*, vol. 13, pp. 1362–1388, 2004.

[44] R. A. Robinson and R. H. Stokes, *Electrolyte Solutions.* London: Butterworths Publications Limited, 2 ed., 1959.

[45] J. Li, K. G. Wilmsmeyer, and L. A. Madsen, "Anisotropic diffusion and morphology in perfluorosulfonate ionomers investigated by NMR," *Macromolecules*, vol. 42, no. 1, pp. 255–262, 2009.

[46] D. J. Griffiths, *Introduction to Electrodynamics.* Prentice-Hall, 3 ed., 1999.

[47] R. Colby, "To be published."

[48] A. A. Kornyshev, "Double-Layer in ionic liquids: Paradigm change?," *Journal of Physical Chemistry B*, vol. 111, no. 20, p. 5545, 2007.

[49] K. B. Oldham, "A Gouy-Chapman-Stern model of the double layer at a (metal)/(ionic liquid) interface," *Journal of Electroanalytical Chemistry*, vol. 613, pp. 131–138, Feb. 2008.

[50] M. S. Kilic, M. Z. Bazant, and A. Ajdari, "Steric effects in the dynamics of electrolytes at large applied voltages. II. Modified Poisson-Nernst-Planck equations," *Physical Review E (Statistical, Nonlinear, and Soft Matter Physics)*, vol. 75, pp. 021503–11, Feb. 2007.

[51] J. Lim, J. Whitcomb, J. Boyd, and J. Varghese, "Transient finite element analysis of electric double layer using Nernst-Planck-Poisson equations with a modified Stern layer," *Journal of Colloid and Interface Science*, vol. 305, no. 1, pp. 159–174, 2007.

[52] J. G. Wijmans and R. W. Baker, "The solution-diffusion model: a review," *Journal of Membrane Science*, vol. 107, pp. 1–21, Nov. 1995.

[53] C. E. Evans, R. D. Noble, S. Nazeri-Thompson, B. Nazeri, and C. A. Koval, "Role of conditioning on water uptake and hydraulic permeability of Nafion membranes," *Journal of Membrane Science*, vol. 279, pp. 521–528, Aug. 2006.

[54] T. Okada, G. Xie, O. Gorseth, S. Kjelstrup, N. Nakamura, and T. Arimura, "Ion and water transport characteristics of Nafion membranes as electrolytes," *Electrochimica Acta*, vol. 43, pp. 3741–3747, Aug. 1998.

[55] J. Li, K. G. Wilmsmeyer, J. Hou, and L. A. Madsen, "The role of water in transport of ionic liquids in polymeric artificial muscle actuators," *Soft Matter*, 2009.

[56] I. Danielewicz-Ferchmin, "Phase diagram of hydration shells in ionic solutions," *The Journal of Physical Chemistry*, vol. 99, pp. 5658–5665, Apr. 1995.

[57] H. Weingartner, "The static dielectric constant of ionic liquids," *Zeitschrift fur Physikalische Chemie*, vol. 220, no. 10, pp. 1395–1405, 2007.

[58] C. J. F. Bottcher, O. C. van Belle, P. Bordewijk, A. Rip, and O. C. van, *Theory of Electric Polarization*. Elsevier Scientific Pub. Co, 1973.

[59] A. H. Sihvola and J. A. Kong, "Effective permittivity of dielectric mixtures," *IEEE Transactions of Geoscience and Remote Sensing*, vol. 26, no. 4, 1988.

[60] S. Nemat-Nasser and J. Y. Li, "Electromechanical response of ionic polymer-metal composites," *Journal of Applied Physics*, vol. 87, no. 7, 2000.

[61] V. Datye, P. Taylor, and A. J. Hopfinger, "Simple model for clustering and ionic transport in ionomer membranes," *Macromolecules*, vol. 17, no. 9, pp. 1704–1708, 1984.

[62] E. Saff and A. Kuijlaars, "Distributing many points on a sphere.," *Mathematical Intelligencer*, vol. 19, no. 1, p. 5, 1997.

[63] S. R. Lowry and K. A. Mauritz, "An investigation of ionic hydration effects in perfluorosulfonate ionomers by fourier transform infrared spectroscopy," *Journal of the American Chemical Society*, vol. 102, pp. 4665–4667, July 1980.

[64] M. Laporta, M. Pegoraro, and L. Zanderighi, "Perfluorosulfonated membrane (Nafion): FT-IR study of the state of water with increasing humidity," *Physical Chemistry Chemical Physics*, vol. 1, no. 19, pp. 4619–4628, 1999.

[65] M. Rubinstein and R. H. Colby, *Polymer physics*. Oxford University Press, July 2003.

[66] P. C. Hiemenz, *Polymer chemistry*. CRC Press, 1984.

[67] L. R. G. Treloar, *The physics of rubber elasticity*. Oxford University Press, Nov. 2005.

[68] T. Kyu and A. Eisenberg, "Mechanical relaxations in perfluorosulfonate ionomer membranes," in *Perfluorinated Ionomer Membranes*, ACS Symposium Series, pp. 79–110, Washington, D. C.: American Chemical Society, Feb. 1982.

[69] R. B. Moore, K. M. Cable, and T. L. Croley, "Barriers to flow in semicrystalline ionomers: A procedure for preparing melt-processed perfluorosulfonate ionomer films and membranes," *Journal of Membrane Science*, vol. 75, pp. 7–14, Dec. 1992.

[70] K. A. Page, K. M. Cable, and R. B. Moore, "Molecular origins of the thermal transitions and dynamic mechanical relaxations in perfluorosulfonate ionomers," *Macromolecules*, vol. 38, pp. 6472–6484, July 2005.

[71] W. G. F. Grot, G. E. Munn, and P. N. Walmsley, "Perfluorinated ion exchange membranes," in *141th National Meeting, The Electrochemical Society, Houston, Texas*, vol. 7, 1972.

[72] W. Hsu and T. Gierke, "Elastic theory for ionic clustering in perfluorinated ionomers," *Macromolecules*, vol. 15, pp. 101–105, 1982.

[73] Y. Kawano, Y. Wang, R. A. Palmer, and S. R. Aubuchon, "Stress-strain curves of Nafion membranes in acid and salt forms," *Polimeros*, vol. 12, pp. 96–101, 2002.

[74] S. Kundu, L. C. Simon, M. Fowler, and S. Grot, "Mechanical properties of Nafion electrolyte membranes under hydrated conditions," *Polymer*, vol. 46, pp. 11707–11715, Nov. 2005.

[75] J. Y. Li and S. Nemat-Nasser, "Micromechanical analysis of ionic clustering in Nafion perfluorinated membrane," *Mechanics of Materials*, vol. 32, pp. 303–314, 2000.

[76] F. Gao and L. Weiland, "A multiscale model applied to ionic polymer stiffness prediction," *Journal of Materials Research*, vol. 23, pp. 833–841, Mar. 2008.

[77] R. Solasi, Y. Zou, X. Huang, K. Reifsnider, and D. Condit, "On mechanical behavior and in-plane modeling of constrained PEM fuel cell membranes subjected to hydration and temperature cycles," *Journal of Power Sources*, vol. 167, pp. 366–377, May 2007.

[78] F. Bauer, S. Denneler, and M. Willert-Porada, "Influence of temperature and humidity on the mechanical properties of Nafion-117 polymer electrolyte membrane," *Journal of Polymer Science Part B: Polymer Physics*, vol. 43, no. 7, pp. 786–795, 2005.

[79] Y. Tang, A. M. Karlsson, M. H. Santare, M. Gilbert, S. Cleghorn, and W. B. Johnson, "An experimental investigation of humidity and temperature effects on the mechanical

properties of perfluorosulfonic acid membrane," *Materials Science and Engineering: A*, vol. 425, pp. 297–304, June 2006.

[80] L. M. Onishi, J. M. Prausnitz, and J. Newman, "Water-Nafion equilibria: Absence of Schroeder's paradox," *The Journal of Physical Chemistry B*, vol. 111, no. 34, pp. 10166–10173, 2007.

[81] N. J. Bunce, S. J. Sondheimer, and C. A. Fyfe, "Proton NMR method for the quantitative determination of the water content of the polymeric fluorosulfonic acid Nafion-H," *Macromolecules*, vol. 19, pp. 333–339, Feb. 1986.

[82] T. A. Zawodzinski, M. Neeman, L. O. Sillerud, and S. Gottesfeld, "Determination of water diffusion coefficients in perfluorosulfonate ionomeric membranes," *Journal of Physical Chemistry*, vol. 95, pp. 6040–6044, July 1991.

[83] P. Hapiot and C. Lagrost, "Electrochemical reactivity in room-temperature ionic liquids," *Chemical Reviews*, vol. 108, pp. 2238–2264, July 2008.

[84] E. T. Enikov and G. S. Seo, "Analysis of water and proton fluxes in ion-exchange polymer-metal composite (IPMC) actuators subjected to large external potentials," *Sensors and Actuators A: Physical*, vol. 122, pp. 264–272, Aug. 2005.

[85] S. Liu, M. Lin, Y. Liu, Q. Zhang, R. Montazami, V. Jain, and J. R. Heflin, "Investigating a few key issues of ionomeric polymer conductive network composite electromechanical transducers," in *Proceedings of SPIE*, (San Diego, CA, USA), pp. 72870T–10, 2009.

[86] J. Lee and Y. Yoo, "Anion effects in imidazolium ionic liquids on the performance of IPMCs," *Sensors and Actuators B: Chemical*, vol. 137, pp. 539–546, Apr. 2009.

[87] T. R. Brumleve and R. P. Buck, "Numerical solution of the Nernst-Planck and Poisson equation system with applications to membrane electrochemistry and solid state physics," *Journal of Electroanalytical Chemistry*, vol. 90, pp. 1–31, June 1978.

[88] M. Z. Bazant, K. Thornton, and A. Ajdari, "Diffuse-charge dynamics in electrochemical systems," *Physical Review E*, vol. 70, no. 2, p. 021506, 2004.

[89] C. Nanjundiah, S. F. McDevitt, and V. R. Koch, "Differential capacitance measurements in solvent-free ionic liquids at Hg and C interfaces," *Journal of The Electrochemical Society*, vol. 144, p. 3392, 2005.

[90] K. A. Mauritz and C. E. Rogers, "A water sorption isotherm model for ionomer membranes with cluster morphologies," *Macromolecules*, vol. 18, no. 3, pp. 483–491, 1985.